SANDIA REPORT

SAND2012-7930
Unlimited Release
Printed April 2013

C6 Plate Puncture Testing Report

Doug VanGoethem, Theresa Cordova, and Phillip Reu

Prepared by
Sandia National Laboratories
Albuquerque, New Mexico 87185 and Livermore, California 94550

Sandia National Laboratories is a multi-program laboratory managed and operated by Sandia Corporation, a wholly owned subsidiary of Lockheed Martin Corporation, for the U.S. Department of Energy's National Nuclear Security Administration under contract DE-AC04-94AL85000.

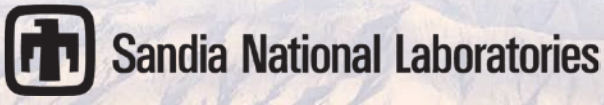

Issued by Sandia National Laboratories, operated for the United **S**tates Department of Energy by Sandia Corporation.

Available to DOE and DOE contractors from
U.S. Department of Energy
Office of Scientific and Technical Information
P.O. Box 62
Oak Ridge, TN 37831

Telephone: (865) 576-8401
Facsimile: (865) 576-5728
E-Mail: reports@adonis.osti.gov
Online ordering: http://www.osti.gov/bridge

Available to the public from
U.S. Department of Commerce
National Technical Information Service
5285 Port Royal Rd.
Springfield, VA 22161

Telephone: (800) 553-6847
Facsimile: (703) 605-6900
E-Mail: orders@ntis.fedworld.gov
Online order: http://www.ntis.gov/help/ordermethods.asp?loc=7-4-0#online

SAND2012-7930
Unlimited Release
Printed April 2013

C6 Plate Puncture Plate Testing Report

Doug VanGoethem
Component Science and Mechanics, 1526

Theresa Cordova
Experimental Mechanics/NDE & Model Validation, 1522

Phillip Reu
Sensing and Imaging Technologies, 1535

Sandia National Laboratories
P.O. Box 5800
Albuquerque, New Mexico 87185-0372

Abstract

There are numerous scenarios where critical systems could be subject to penetration by projectiles or fixed objects (e.g., collision, natural disaster, act of terrorism, etc.). It is desired to use computational models to examine these scenarios and make risk-informed decisions; however, modeling of material failure is an active area of research, and new models must be validated with experimental data. The purpose of this report is to document the experimental work performed from FY07 through FY08 on the Campaign Six Plate Puncture project. The goal of this project was to acquire experimental data on the puncture and penetration of metal plates for use in model validation. Of particular interest is the PLH failure model also known as the multilinear line segment model. A significant amount of data that will be useful for the verification and validation of computational models of ductile failure were collected during this project were collected and documented herein; however, much more work remains to be performed, collecting additional experimental data that will further the task of model verification.

ACKNOWLEDGMENTS

The authors are grateful to the experimental team which included D.J. Kenney, John Laing, David Szklarz, and Larry Yellowhorse for their invaluable insight and expertise.

CONTENTS

FIGURES

TABLES

NOMENCLATURE

~	approximately
x	by
°	degrees
∅	diameter
"	inch
µm/m	micrometers per meter
µs	microseconds
µstrain	microstrain
±	plus or minus
3-D	three-dimensional
.asc	ASCII (American Standard Code for Information Interchange) image file
ARP	abrasion-resistant plate
ASTM	American Society for Testing and Materials
Con	conical
Cyl	cylindrical
DIC	digital image correlation
DIN	German Institute for Standardization
DT	drop table
E	modulus of elasticity
EDP	Experimental Development Plan
EDP Mech	assigned test number in the EDP software
e1	DIC data label
e2	DIC data label
FFT	fast Fourier transform
fps	feet per second
FSO	full-scale output
FY	fiscal year
g	acceleration
G	acceleration
Hz	hertz (cycles per second)
ID	identification
in	inches
in/in	inches per inch
IRIG	Inter Range Instrumentation Group
kHz	kilohertz

kip	kilopounds (1,000 pounds-force)
kN	kilonewtons
ksi	kilopounds (kip) per square inch
ksi/min	kilopounds (kip) per square inch per minute
lb_f	pounds-force
LVDT	linear variable differential transformer
MHz	megahertz
mils/sec	thousandths of an inch per second
mm	millimeters
ms	milliseconds
NA	not applicable
No.	number
PC	personal computer
PCI	peripheral component interconnection
PLH	Power Law Hardening
pps	pictures per second
psi	pounds per square inch
SG	strain gage
TTL	transistor-transistor logic
VIDAS	VXI data acquisition system
VXI	VMEbus Extensions for Instrumentation
W	deformation

1 INTRODUCTION

The purpose of this report is to document the experimental work performed from FY07 through FY08 on the Campaign Six Plate Puncture project. This project was originally two subprojects labeled PLH Failure Criteria (Task 01.3.3.1) and Panel Testing (Task 01.3.3.2).

There are numerous scenarios where critical systems could be subject to penetration by projectiles or fixed objects (e.g., collision, natural disaster, act of terrorism, etc.). It is desired to use computational models to examine these scenarios and make risk-informed decisions; however, modeling of material failure is an active area of research, and new models must be validated with experimental data. The goal of this Campaign Six project was to acquire experimental data on the puncture and penetration of metal plates for use in model validation. Of particular interest is the PLH failure model also known as the multilinear line segment model developed by Jerry Wellman (Organization 1525).

1.1 Previous Work

Previous work (i.e., prior to FY07) utilized three-hole crack growth coupons for constitutive model parameter fitting. FY07 experimental work switched to metallic plates fractured by quasi-statically pushing a cylindrical punch through these plates. Tensile testing for this project in FY07 is not covered in this report. The plate punch geometry work was begun in FY07 under a different investigator. The documentation of FY07 testing presented in this section uses data and pictures left by the initial investigator who transferred positions prior to post-processing and test documentation. Quasi-static tests were performed on 16-gauge mild steel plates. Time, load, and actuator displacement were recorded for all tests. Table 1 lists the various punch plate tests performed, the punch size used for each test, and additional sensors recorded. All plates tested were mild steel punched with a cylindrical punch. Most testing was performed in the Structural Frame. Tests 12–14 and 21–23 were tested in a uniaxial load frame. Tests 13, 14, and 21–23 did not incorporate additional displacement sensors apart from the actuator's internal linear variable differential transformer (LVDT) for displacement measurements. All tests in the Structural Frame used an external LVDT placed on the plate's flange or Keyence sensors with less noise to record the displacement of the punch relative to the plate's flange.

Table 1. FY07 Test Matrix

Test Number	MTS File Name/ HBM File Name	Plate ∅ (inch)	Punch ∅ (inch)	# of Strain Gages	Additional Sensors	Comments
1	6D-1.0P-S01/NA	6	1	0	1 external LVDT, 1 Keyence	—
2	6D-1.0P-S02/NA	6	1	0	1 external LVDT, 1 Keyence	—
3	6D-1.0P-S03/NA	6	1	0	1 external LVDT, 1 Keyence	—
4	6D-1.0P-S04/NA	6	1	0	1 external LVDT, 1 Keyence	—

continued . . .

Table 1. FY07 Test Matrix, continued

Test No.	MTS File Name/ HBM File Name	Plate ∅ (inch)	Punch ∅ (inch)	No. of Strain Gages	Additional Sensors	Comments
5	6D-1.0P-S05/ 6in_run5.asc	6	1	0	7 external LVDTs, 1 Keyence	—
6	6D-1.0P-S06/ 6in_run6.asc	6	1	24	1 external LVDT, 1 Keyence	—
7	6D-0.5P-S07/ 6in_run7.asc	6	0.5	0	1 external LVDT, 1 Keyence	—
8	6D-0.5P-S08/ 6in_run8.asc	6	0.5	0	1 external LVDT, 1 Keyence	—
9	6D-0.5P-S09/ 6in_run9.asc	6	0.5	3	1 external LVDT, 1 Keyence	—
10	6D-0.5P-S10/ 6in_run10.asc	6	0.5	0	1 external LVDT, 1 Keyence	—
11	6D-0.5P-S11/NA	6	0.5	0	1 external LVDT, 1 Keyence	—
12	6D-1.0P-MTS12	6	1		1 external LVDT, 1 auxiliary load cell	Tested on 110 kip frame
13	12D-1.0P-MTS01-R1/ NA	12	1	0	No additional sensors	Tested on 220 kip frame
14	12D-1.0P-MTS01-R2/ NA	12	1	0	No additional sensors	Tested on 220 kip frame
15	12D-1.0P-S02/NA	12	1	0	1 external LVDT, 1 auxiliary load cell	—
16	12D-1.0P-S03-R1/NA	12	1	0	1 external LVDT, 1 auxiliary load cell	—
17	12D-1.0P-S03-R2/NA	12	1	0	1 external LVDT, 1 auxiliary load cell	—
18	12D-1.0P-S04/NA	12	1	0	1 external LVDT, 1 auxiliary load cell	—
19	12D-1.0P-S05/NA	12	1	0	1 external LVDT, 1 auxiliary load cell	—
20	12D-1.0P-S06/NA	12	1	0	1 external LVDT, 1 auxiliary load cell	—
21	12D-1.0P-MTS03/NA	12	1	0	No additional sensors	Tested on 220 kip frame

Table 1. FY07 Test Matrix, continued

Test No.	MTS File Name/ HBM File Name	Plate ∅ (inch)	Punch ∅ (inch)	No. of Strain Gages	Additional Sensors	Comments
22	12D-1.0P-MTS04/NA	12	1	0	No additional sensors	Tested on 220 kip frame
23	12D-0.5P-MTS02/NA	12	0.5	0	No additional sensors	Tested on 220 kip frame
24	12D-0.5P-S01/NA	12	0.5	0	1 external LVDT, 1 auxiliary load cell	—
25	12D-0.5P-S07/NA	12	0.5	0	1 external LVDT, 1 auxiliary load cell	—
26	12D-0.5P-S08/NA	12	0.5	0	1 external LVDT, 1 auxiliary load cell	—
27	12D-0.5P-S09/NA	12	0.5	0	1 external LVDT, 1 auxiliary load cell	—
28	12D-0.5P-S10/NA	12	0.5	0	1 external LVDT, 1 auxiliary load cell	—
29	12D-0.5P-S11-R1/NA	12	0.5	0	1 external LVDT, 1 auxiliary load cell	—
30	12D-0.5P-S11-R1/NA	12	0.5	0	1 external LVDT, 1 auxiliary load cell	—

If the test had an associated HBM file, rosette strain gages may have been applied to the plate or additional displacement sensors such as a Keyence sensor or LVDTs were used. Unfortunately the 12-inch diameter plates were not instrumented with strain gages; therefore, time, load, and displacement are the only information available for the larger diameter plates. Most of the plates were tested in the Structural Frame unless otherwise noted in the *Comments* column of Table 1. Test 9 included three rosette strain gages located on the punch side of the plate. The 6-inch diameter plate listed as Test 6 was the most heavily gaged plate with a total of 24 rosette strain gages and is shown in Figure 1. The strain gages were bonded to the punch side of the plate every 45° at locations one, two, and three inches away from the center. Stacked strain gages were used closest to the center where the strain was anticipated to be the highest and where less bondable space was available. Adjacent rosette strain gages were used at all other locations.

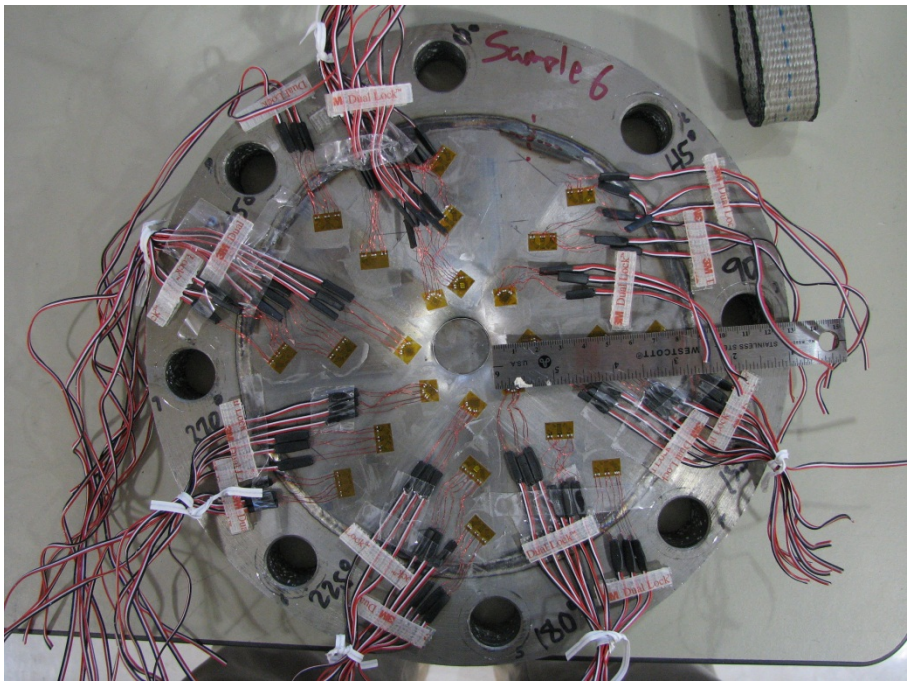

Figure 1. 6-inch diameter plate punched by a 1-inch cylindrical punch

Test 6 contained a total of 72 measured channels in addition to 72 calculated channels for principal strains and principal strain angles. A low-pass Bessel filter was used for the strain gage data. A 1-inch cylindrical punch pierced the heavily gaged plate causing perforation of the plate and reaching a maximum load of 4,443 pounds-force (lb_f). Those plates tested with the smaller 0.5-inch punch, perforated with maximum loads around 2,490 ± 10 lb_f. Thus the measured strain was higher for the plates that were pierced with the bigger 1-inch punch compared to the plates punctured with the 0.5-inch punches. Figure 2 displays an example of the longer flat 1-inch cylindrical punch used for the FY07 test series.

Figure 2. FY07 flat end, 1-inch cylindrical punch

The picture of the punch shown in Figure 2 was taken post-test and shows typical damage incurred by the 1-inch cylindrical punches. The damage at the tip extends approximately one inch in length because the punches used in this test series were allowed to fully pierce the plate. This complete penetration typically dislodged the plate material in contact with the circular end of the punch causing permanent deformation to the plate near the area of contact. The 0.5-inch cylindrical punches were similar in design to the punch shown in Figure 2 but were more susceptible to punch damage during testing as a result of their thin, elongated, cylindrical shape. Common damage to the 0.5-inch cylindrical punches included permanent bending of the smaller diameter punches or complete failure of the punch as shown in Figure 3.

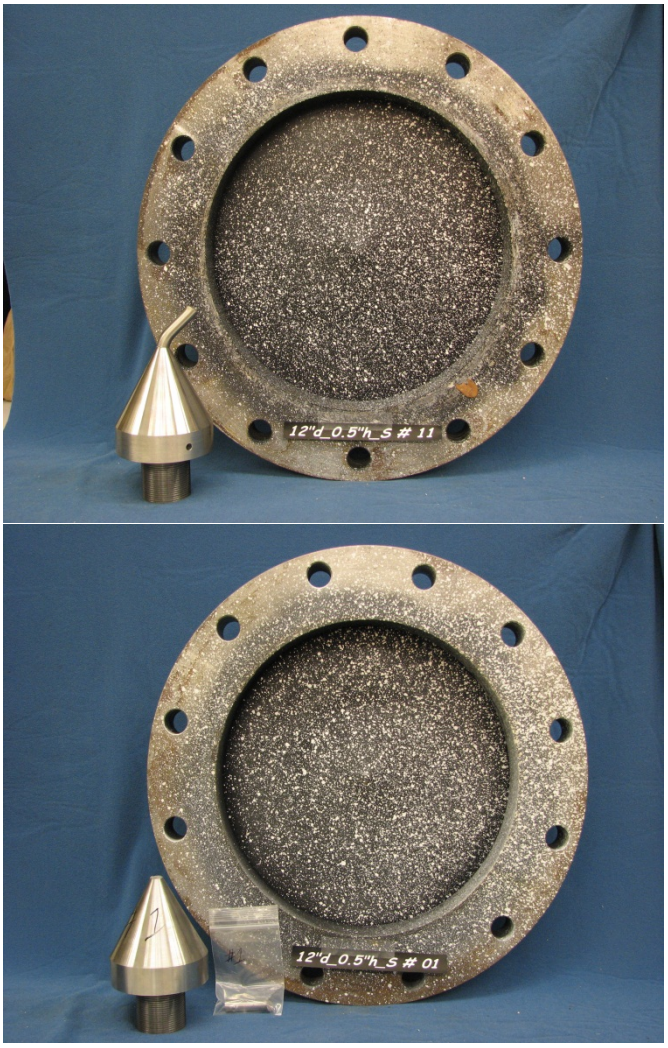

Figure 3. Damaged punch (post-test)

Problems such as bending of the longer length punches witnessed during and post-testing in FY07 resulted in further improvements to the punch design for FY08 tests. Although full engagement of the cylindrical punch to perforate the plate was allowed, the FY07 test series did not engage the tapers of the punches, and further exploration of taper engagement was explored in FY08.

The highly instrumented plate, Test 6, demonstrated consistent response patterns as measured by the strain gages symmetrically laid out on the plate. The peak load was approximately 4,441 lb_f . All strain measurements were highest near the center and decreased as the distance from the center increased. Radial strains demonstrated stretching in the material while most circumferential strain readings indicated an initial compression of the material followed by an increase in material length. The strain gages located near the weld boundary maintained an increasing negative strain reading, possibly demonstrating an influence from boundary constraints. Similar strain gage readings confirmed the central location of the punch relative to the plate. The calculated principal-1 strains for those strain gages located one inch away from the center are plotted in Figure 4 and Figure 5.

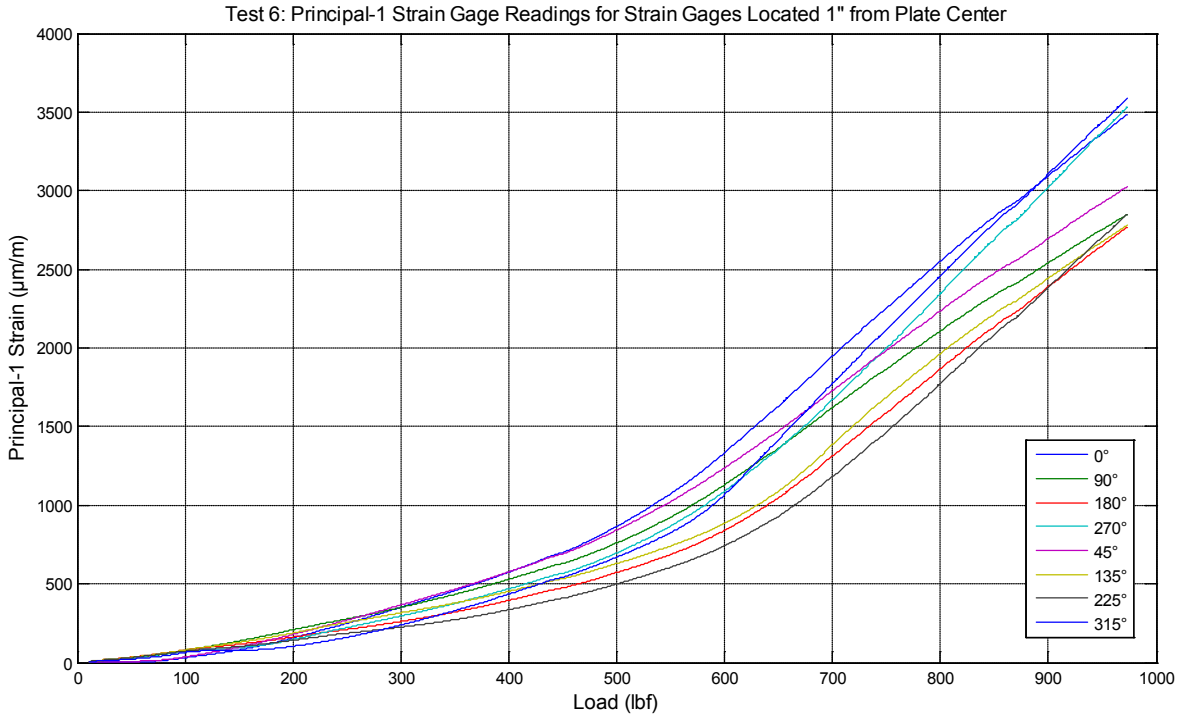

Figure 4. Test 6 principal strain 1

Strain is presented in Figure 4 in units of microstrain (µm/m), and load is represented as lb_f. The calculated strain gage channels for principal strain 1 increased with increasing load and all demonstrated a similar response. The calculated strains located at 0°, 270°, and 315°, exhibited slightly larger strains than any other location on the plate. The signal for the rosette strain gage located one inch from the center at the 0° axis was lost at approximately 1,700 lb_f. Post-test pictures reveal that this gage became delaminated from the plate. A similar loss in signal was observed for the strain gage located one inch from the center along the 315° line.

A look at the calculated principal 2 strains in Figure 5 showed a similar trend in data as did the principal-1 strains.

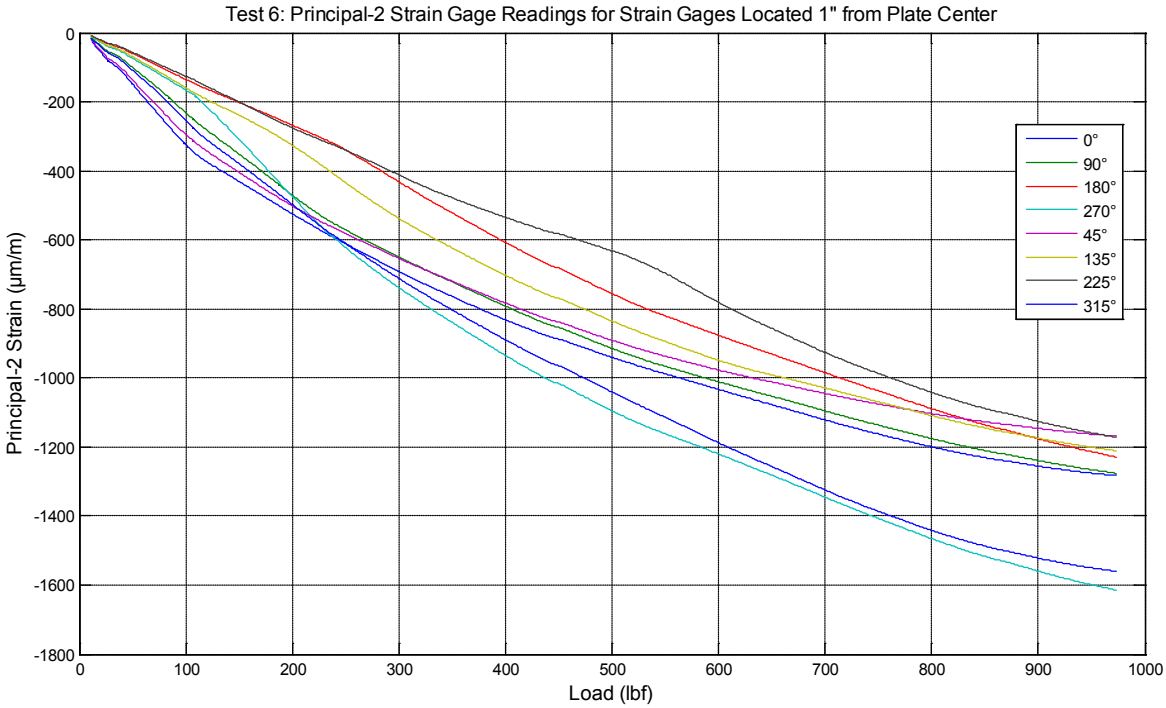

Figure 5. Test 6 principal strain 2

Once again the strains at 0°, 270°, and 315° displayed slightly higher calculated readings than did the other strain gages. Unlike the first principal strains, the second principal strains became increasingly negative as the load was increased.

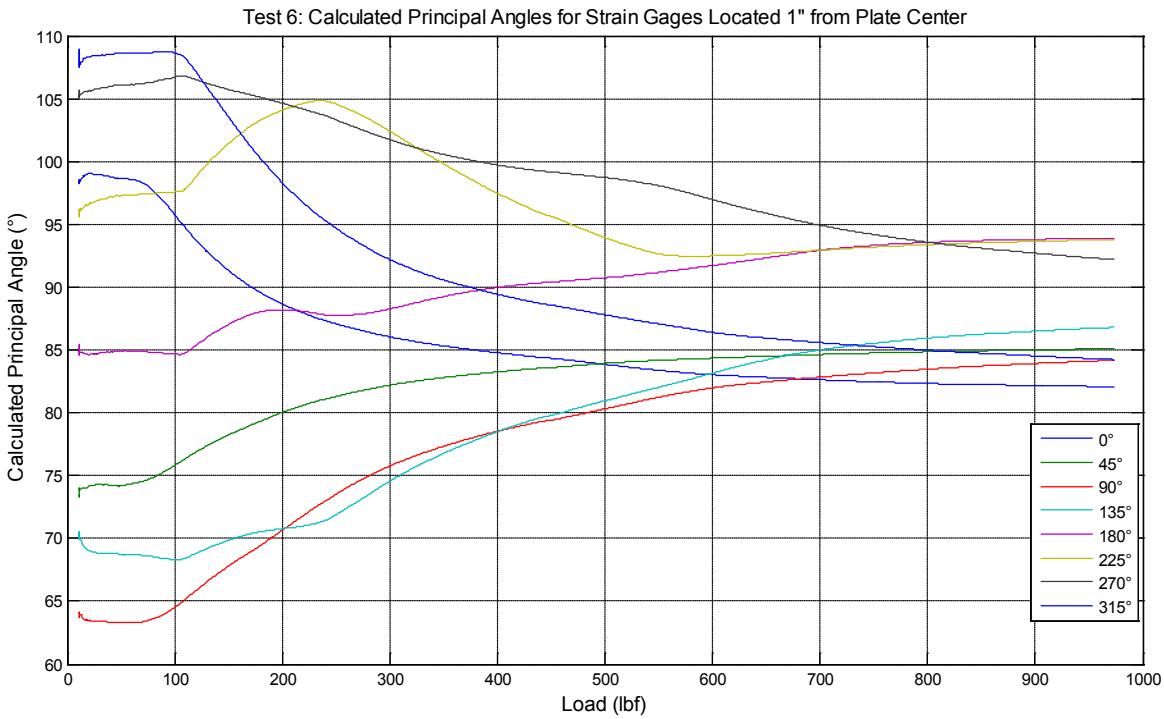

Figure 6. Test 6 principal angle

It should be noted from Figure 1 that the orientation of each strain gage changed as the radial angle changed. In addition, the strain gages orientation pattern is not followed for strain gages located along the 0° and 45° radial angles: these gages were rotated 90° counterclockwise from the laid out pattern. Hence interpretation of the measurements shown in Figure 6 after compensating for the variation in strain gage orientations revealed that all principal axes pointed to the center of the plate. The principal angles on the ordinate axis are represented in units of degrees while load on the abscissa is shown in lb_f.

Although Test 9 was gaged for comparison with digital image correlation (DIC) results, only results comparing calculated principal strains from Test 6 and DIC findings are presented here because other results were similar. In general, excellent agreement was seen between all gages. For simplicity, only the gages at 0°, 90°, 180°, and 270° are plotted for comparison. One uncertainty for the comparison was that *approximate* locations were chosen for extracting the DIC data that corresponded as closely as possible with the strain gage locations. Exact locations were not obtained because the strain gages were located on the opposite side of the plate from the DIC extraction data points.

Figure 7 shows data from three sets of rosettes at the 1-inch radius from the center of the plate. The DIC data are indicated by the *e1* label, while the gage data are labeled as *Gage*.

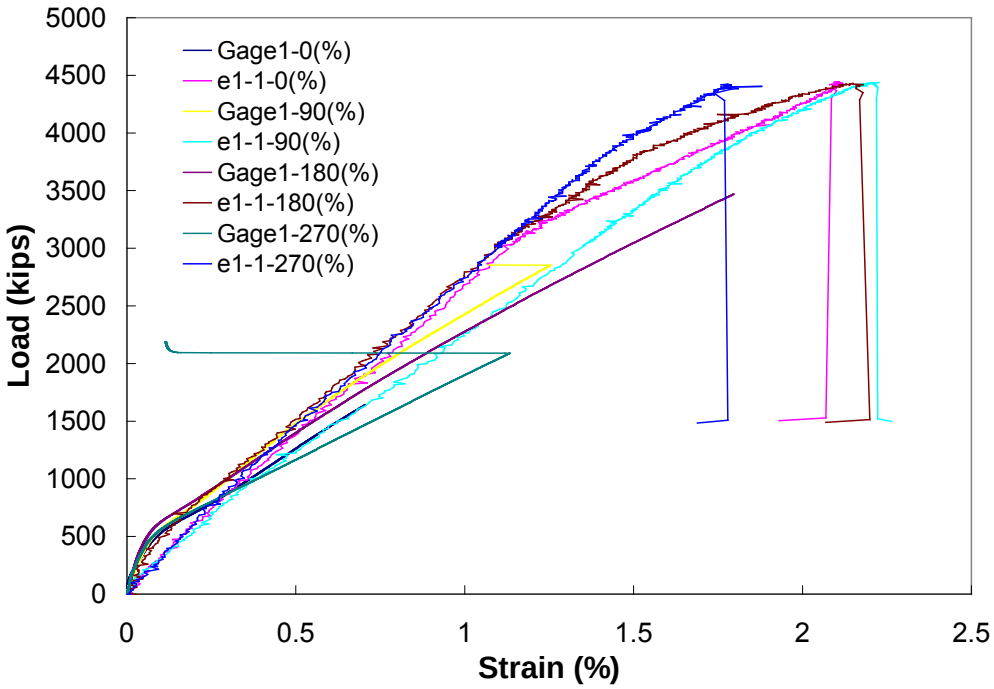

Figure 7. Principal strain data from gages and corresponding DIC results extracted from the data

The DIC data are noisier than the gage data. This is an inherent limitation in DIC in that the strain data are obtained by differentiating the displacement data. This amplifies any noise in the data. Also note that the gages failed between 1% and 2% strain, well before failure of the part. DIC is typically able to achieve a much higher maximum strain measurement (hence the use of Lagrangian strain) than even a perfectly applied strain gage. However, without smoothing or averaging, the strain noise is higher. Data for the 2-inch radius are shown in Figure 8, and data for the 3-inch radius are shown in Figure 9.

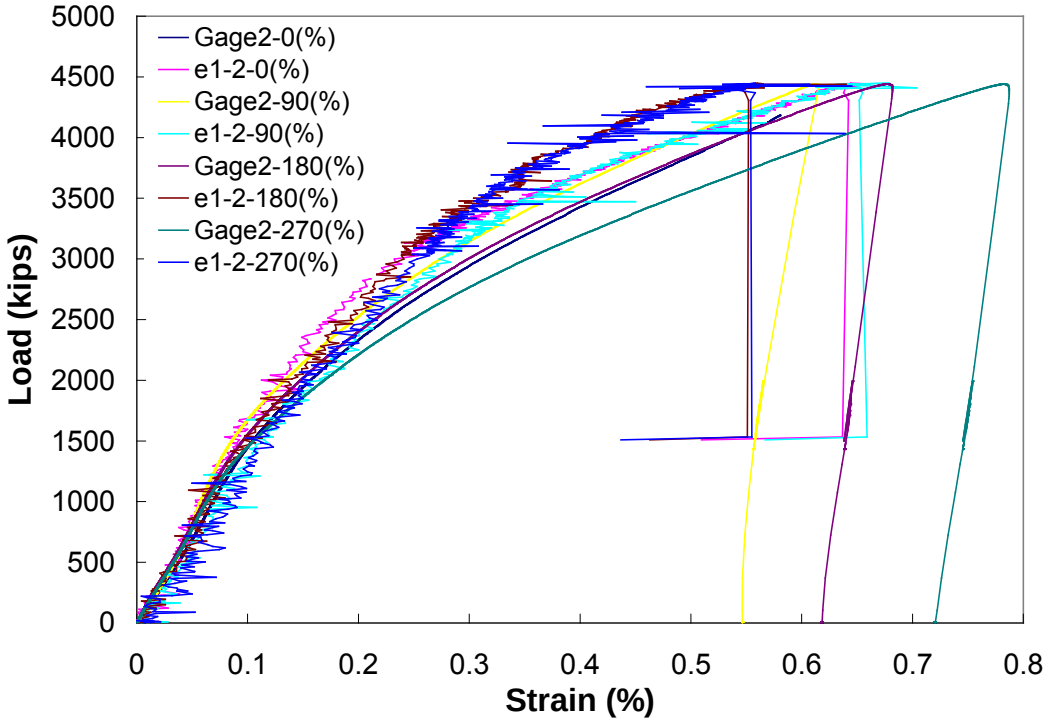

Figure 8. Principal strain data at 2-inch radius

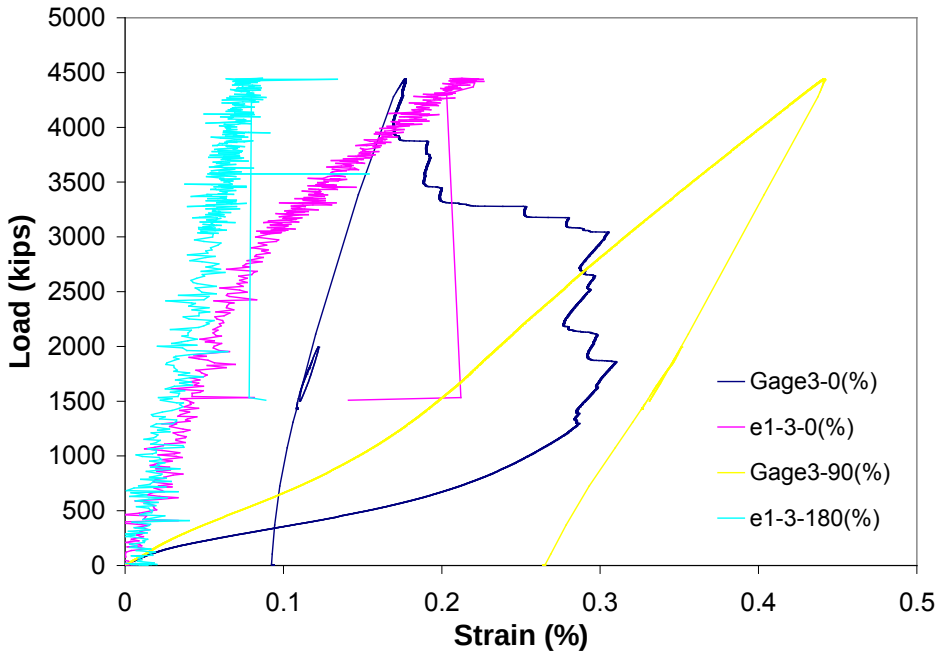

Figure 9. Principal strain data at 3-inch radius (Sample 6)

Comparison of the data at the 3-inch radius suffers mainly because of the low strain levels in that area of the sample: typically DIC can yield results down to 100 microstrain but struggles to achieve better than that. Also, this portion of the sample was not easily imaged with the load frame holding the sample. This did not allow for a data point to be picked as close to the gage location as desired.

1.2 FY08–FY09 Approach

1.2.1 Plate Geometry

Test specimens were constructed by welding a disk of material to a commercial AWWA C207 Class E pipe flange. The nominal 6-inch size is shown in Figure 10. In FY07 some samples were made using a 12-inch nominal pipe flange; however, it was not possible to accommodate this size in the dynamic test setup. Therefore, all samples tested in FY08 and FY09 were fabricated for the size shown below. This geometry was selected because pipe flanges are an off-the-shelf item. Welding the plate provides a constrained boundary condition. The constrained boundary condition and axisymmetric geometry make it easier to model the tests with a finite element method.

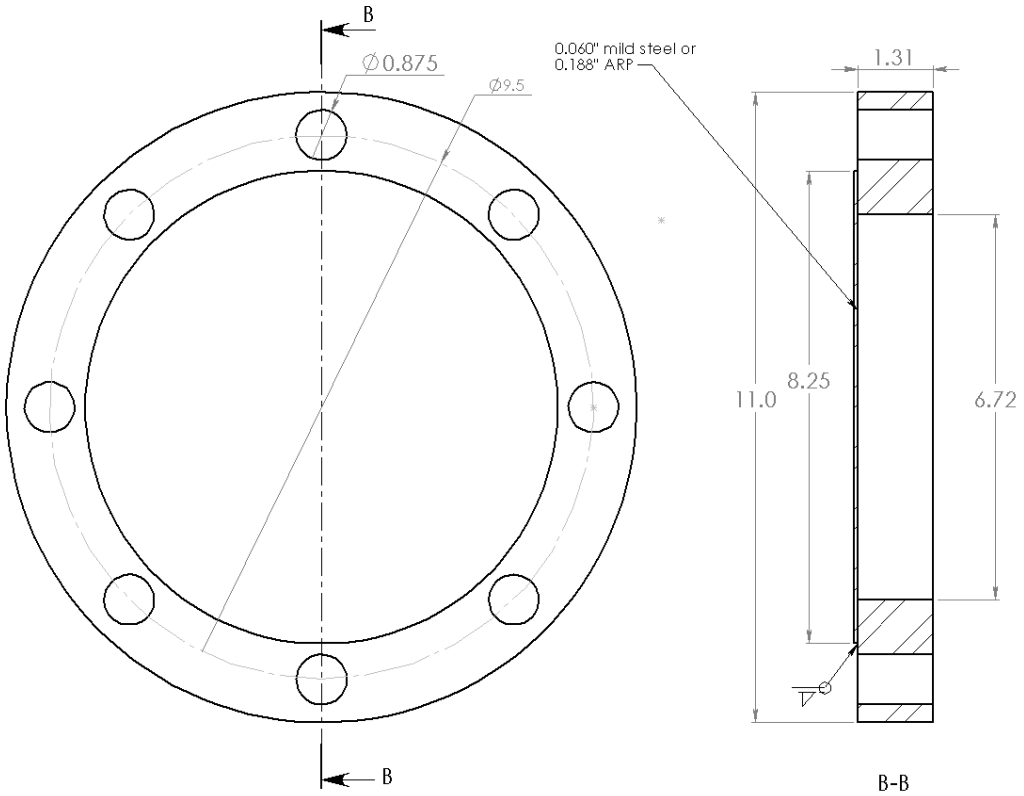

Figure 10. 6-inch (nominal) plate geometry

1.2.2 Punch Geometry

Two punch designs were utilized and are shown in Figure 11 and Figure 12. The cylindrical or flat-end punch is similar to the geometry used in FY07 although, the cylindrical section was shortened to be 0.5 inches long instead of 2 inches. This punch geometry typically loads the plate until a disk of material is punched out of the plate as it fails. The conical punch geometry was added to investigate a different stress field caused by spherical contact. The punches were manufactured of 4340 steel and heat treated to 188 ksi (i.e., 41.5 Rockwell C hardness).

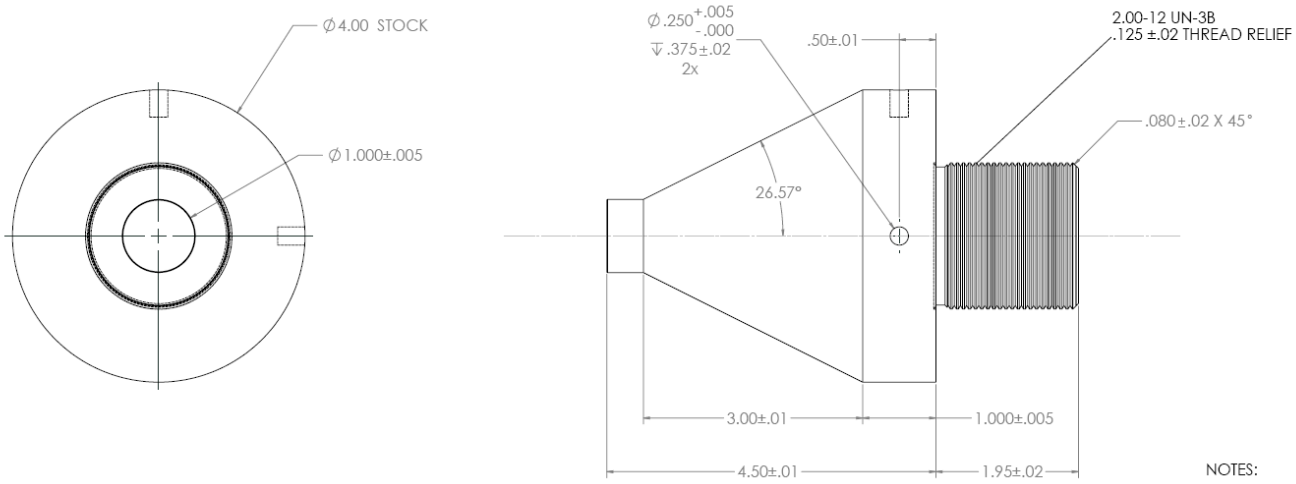

Figure 11. Cylindrical (i.e., flat-end) punch

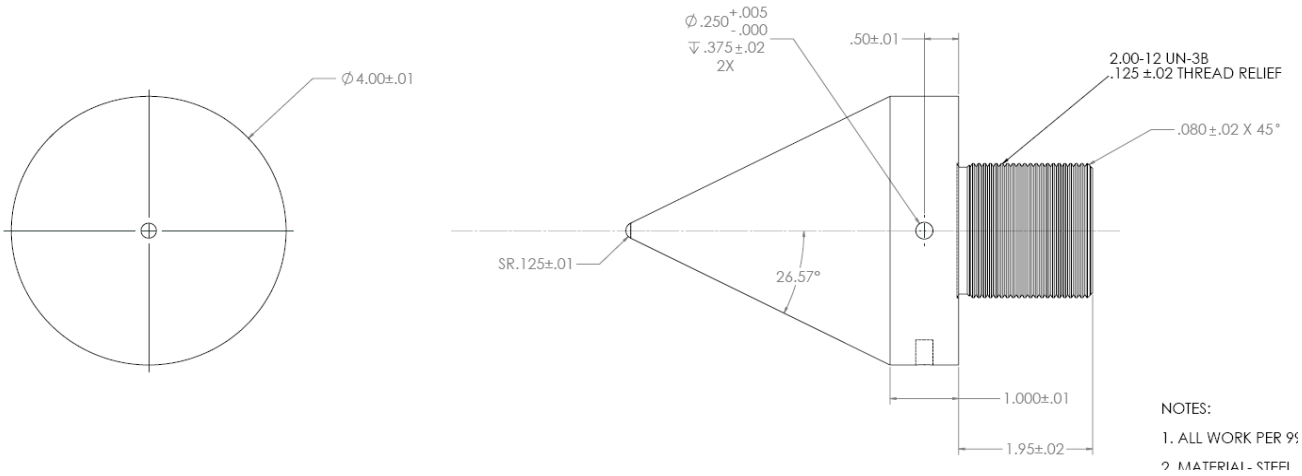

Figure 12. Conical punch

During preliminary dynamic testing using bolted steel and aluminum plates, the punch traveled approximately 0.5 inches past the cylindrical portion and engaged the tapered region. This resulted in radial crack formation, leaving *petals* of material in the aluminum plates, but not in the more ductile steel. Because this petaling behavior was of interest to the model developers, the test plan was modified to exercise this mechanism further. Previous testing had stopped the punch travel on the cylindrical portion without engaging the taper. In this round of testing, the punch was forced through approximately 3.5 inches to engage the taper and exercise the petaling failure mode of the plates.

1.2.3 Materials and Material Properties

Two materials were investigated in this round of testing. Samples were manufactured with 16-gauge thickness (0.060-inch) mild steel (ASTM A366) and 0.188-inch thick abrasion-resistant steel plate (i.e., *abrasion-resistant plate*, ARP). Abrasion-resistant plate is a hard (477–534 Brinell Hardness Number), high-strength steel with 12–15% elongation at failure. These two materials were selected because they would exhibit drastically different failure behaviors, one being a low-strength, thin material and the other being a high-strength, thick material.

Dog bone-shaped tensile samples (also referred to as *coupons*) were cut from the same material lots in order to experimentally attain material properties associated with each material. Samples were cut in the longitudinal and transverse directions for each material. Elongation of the samples was measured with a calibrated extensometer. The abrasion-resistant steel samples were tested to failure. The mild steel specimens were tested to near failure, leaving a small portion of the center material intact.

Figure 13 and Figure 14 show the tested samples of mild steel and abrasion-resistant steel, respectively.

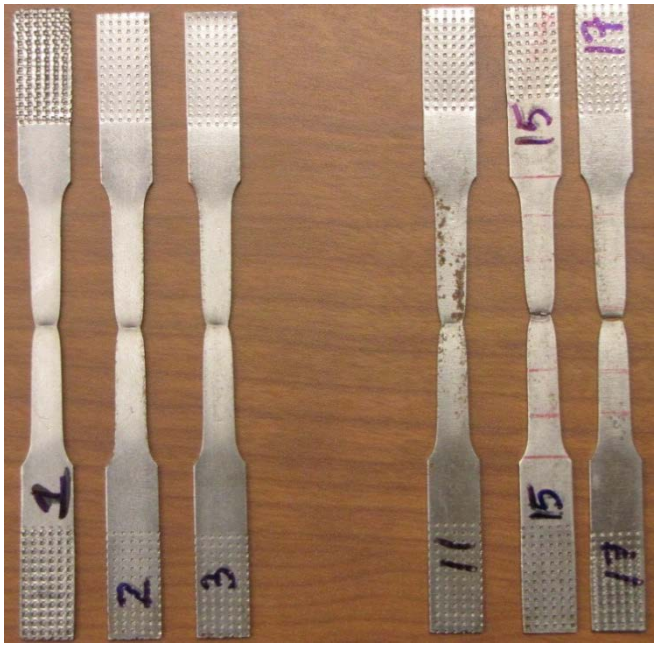

Figure 13. Mild steel tensile samples (post-test)

Figure 14. Abrasion-resistant steel tensile samples (post-test)

After close examination of the surface finish of the mild steel plate, it was determined that Tensile Samples 1–3 had been cut parallel to the rolled (i.e., longitudinal) direction, and Tensile Samples 11, 15, and 17 were cut in the transverse direction. This surface roll direction for the abrasion-resistant specimens was not apparent.

Because the roll direction of the abrasion-resistant material was not apparent from the surface finish of the material, further investigation of the stress-strain curves for both the mild steel and abrasion-resistant steel provided information for distinguishing the two directions.

The mild steel is a very ductile material. This is apparent with the load decay rather than abrupt load drop as MS-15 and MS-17 in Figure 15 were pulled to separation. All samples achieved an elongation over 37%. The tensile strengths for the samples were approximately 50.5 ksi for MS-17 and MS-15, and 53 ksi for the other samples.

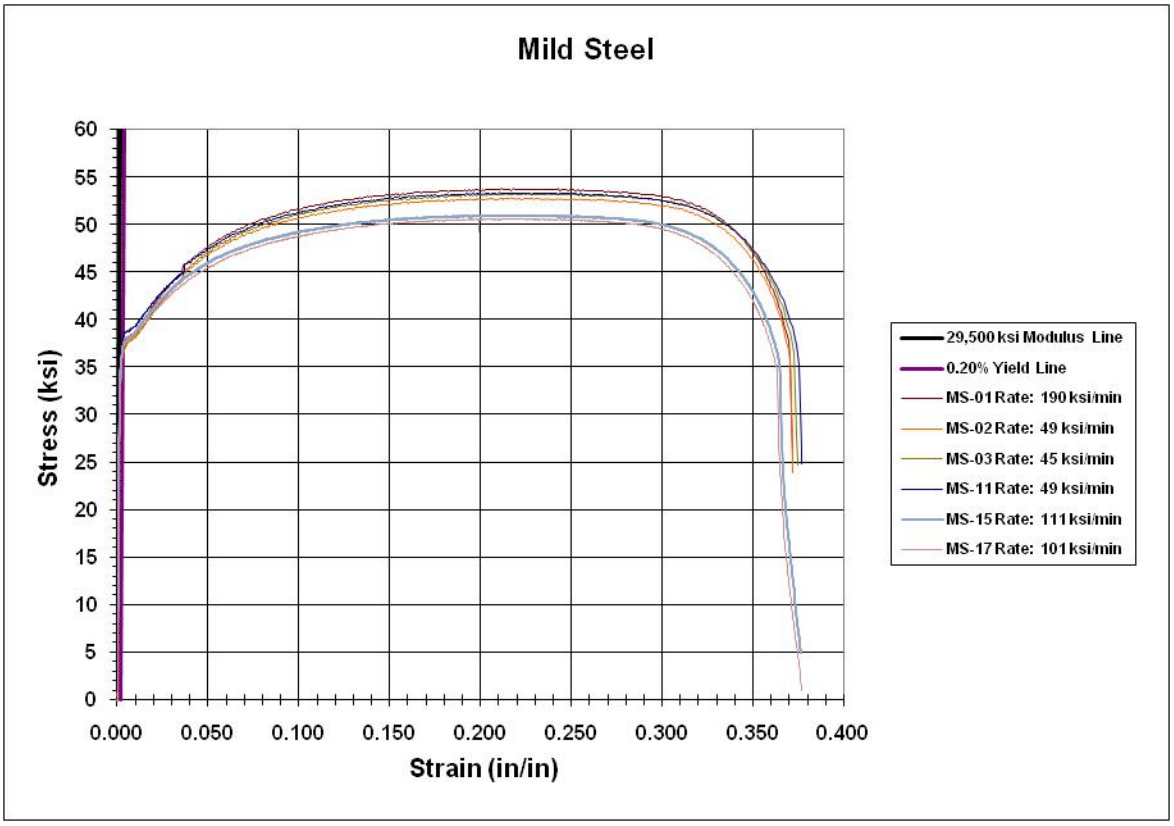

Figure 15. Engineering stress-strain curve for mild steel

A closer look at the stress-strain curve in Figure 16 reveals information regarding the plastic yielding of the material. In addition to similar yield and ultimate strengths, the mild steel tensile samples exhibit close elastic behaviors. That is, the modulus of elasticity, E, is alike for transverse and longitudinal samples. The modulus of elasticity as well as the 0.2% yield offset are plotted in Figure 16. From the 0.2% offset line, a yield stress of approximately 37 ksi is noted.

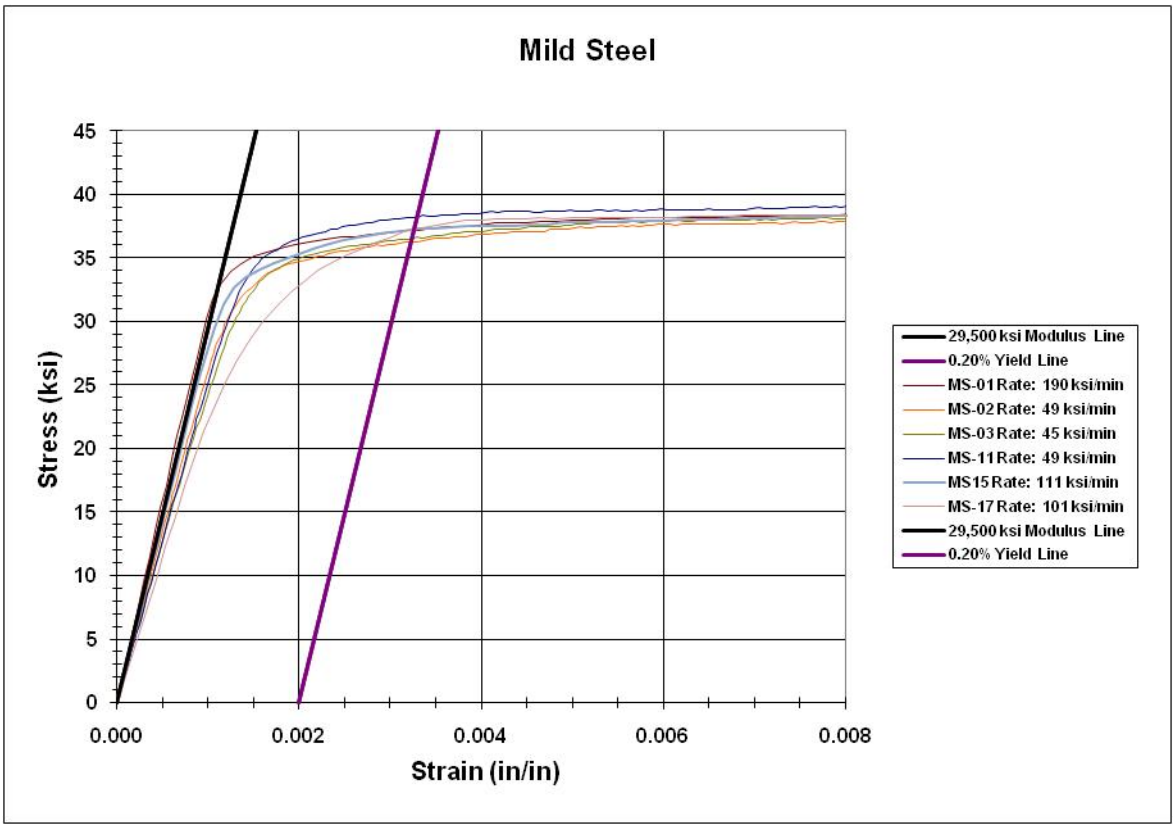

Figure 16. Elastic region of the mild steel engineering stress-strain curve

Figure 17 and Figure 18 compare tensile tests in the longitudinal and transverse directions for the abrasion-resistant steel.

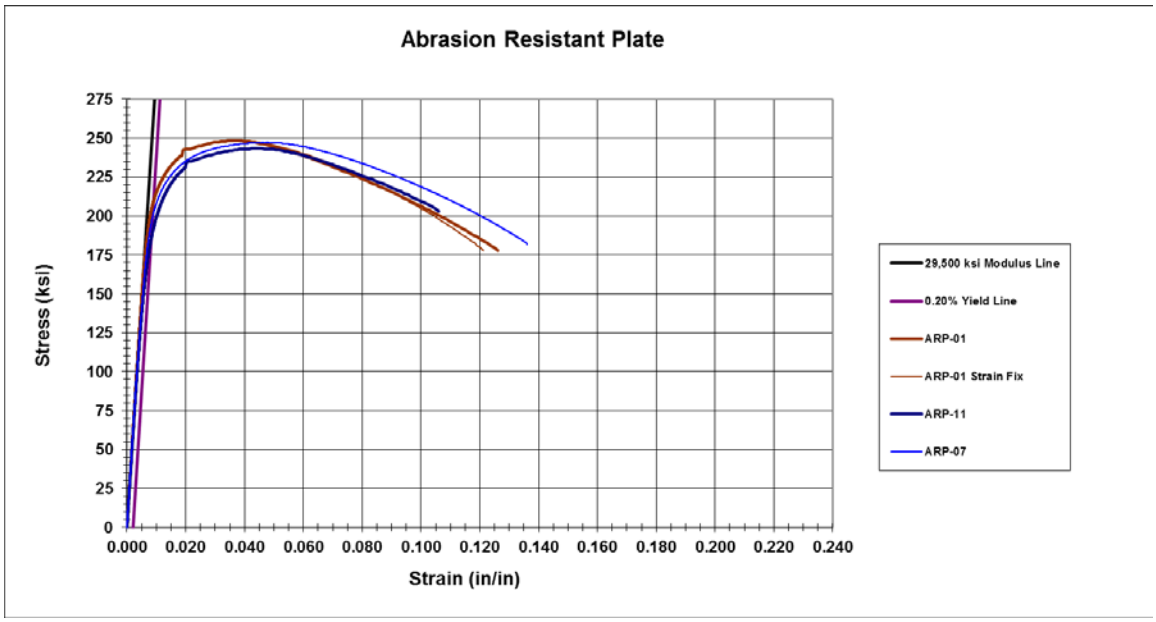

Figure 17. Stress-strain curve for abrasion-resistant plate

One extensometer knife edge for specimen ARP-01 (see Figure 17) was located in the area at which the specimen fractured, so the final elongation displayed for that curve in this graph is incorrect. The ARP-01 Strain Fix curve represents the actuator stroke from the point of ultimate stress and better represents the elongation of the specimen. Including the correction of the strain for ARP-01, the elongation for the specimens tested differed by 3%: it is more ductile in one direction than the other. The ultimate strength is about the same in both directions. According to the supplier, Oregon Steel Mills, a decrease in elongation in the transverse direction as compared to the longitudinal direction is expected. From this information, it was deduced that ARP-01 and ARP-07 represent the longitudinal direction. Without more information from the metal supplier as to the reason for the variance in strain for each direction, it can be assumed that the cause is attributed to the metal forming process of the material.

A magnified view of the initial portion of the stress-strain curve of Figure 18 gives information on the measured modulus of elasticity and yield strength of the abrasion-resistant metal.

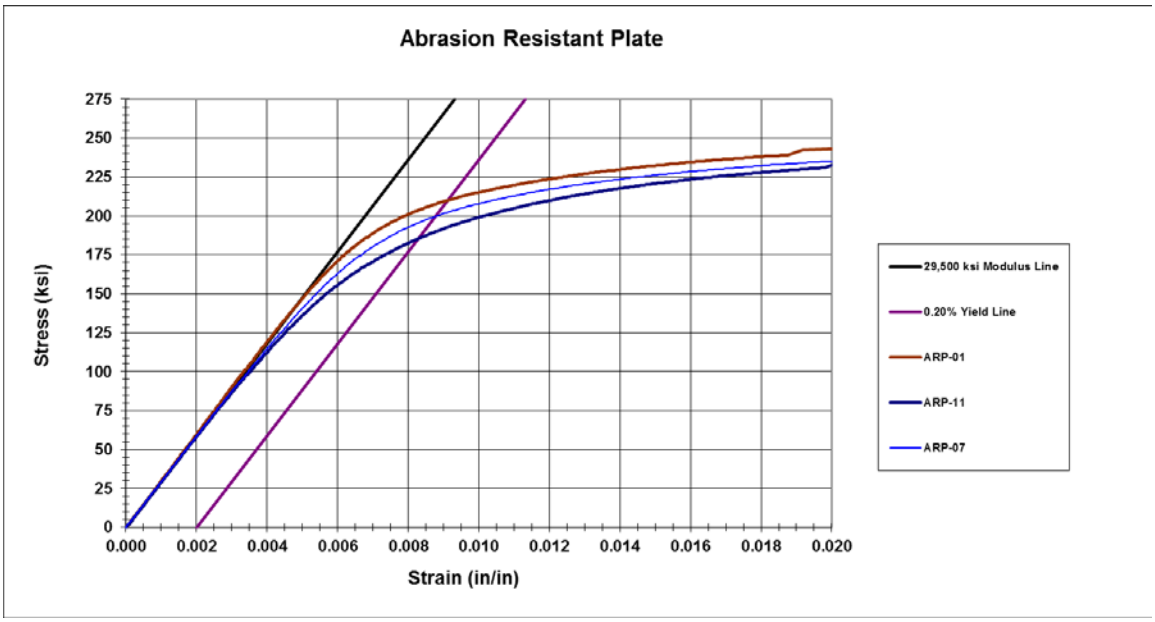

Figure 18. Elastic-to-plastic engineering stress-strain region of ARP steel

Initially, both test coupons follow each other closely in the elastic region of the curve but soon begin to deviate as the slopes of each line become nonlinear. This early separation of curves is viewed throughout the entire stress-strain response of the samples.

Table 2 summarizes the experimental material properties for the mild steel and the abrasion-resistant steel.

Table 2. Engineering Material Properties for ARP and Mild Steel

Steel Type	Sample Number	Modulus of Elasticity (ksi)	Yield Strength (ksi)	Ultimate Stress (ksi)	% Elongation
Mild	1	30,950	37.1	53.8	37.2
	2	26,309	36.5	52	37.2
	3	24,925	36.7	52.5	37.5
	11	25,199	38.3	52.7	37.7
	15	28,836	37.3	50.9	37.6
	17	22,853	37.8	50.6	37.7
Abrasion-Resistant	1	30,043	208.8	248.4	12.1
	7	28,196	202.9	247.1	13.6
	11	28,334	186.8	243.3	10.6

Both materials exhibited typical ductile behavior with tensile specimens necking and producing fracture angles of 45°. The % elongation reported in Table 2 for the mild steel depicts little elongation change for specimens tested to complete failure and specimens tested to near material separation. The abrasion-resistant steel had almost a five times higher ultimate stress than the mild steel but a lower elongation by a factor of three. The abrasion-resistant material met the manufacturer's listed ultimate strength range of 230–255 ksi, but Sample 11 failed to meet the yield strength range of 210–230 ksi. As mentioned previously, the yield strength was found from the intersection between the stress-strain curve and a 0.2% elastic curve offset.

2 QUASI-STATIC TESTING

2.1 Quasi-Static Punch Plate Test Setup

2.1.1 Mechanical

A 150-kip portable actuator was mounted to the rear vertical wall of the structural frame located in the Structural Mechanics Lab in Building 860, Room126. A combination of all-thread rods and square tubing provided spacing and rigidity between the vertical structural frame wall and a 3-inch thick steel mounting plate to which each punch plate was bolted. The 3-inch steel mounting plate was allowed to rest on four steel channels. Figure 19 depicts the test setup without the punch and punch plate installed for clarity. This setup was designed to allow unobstructed visual access to the specimen for DIC measurements. This would not have been practical if testing were performed in a standard uniaxial load frame.

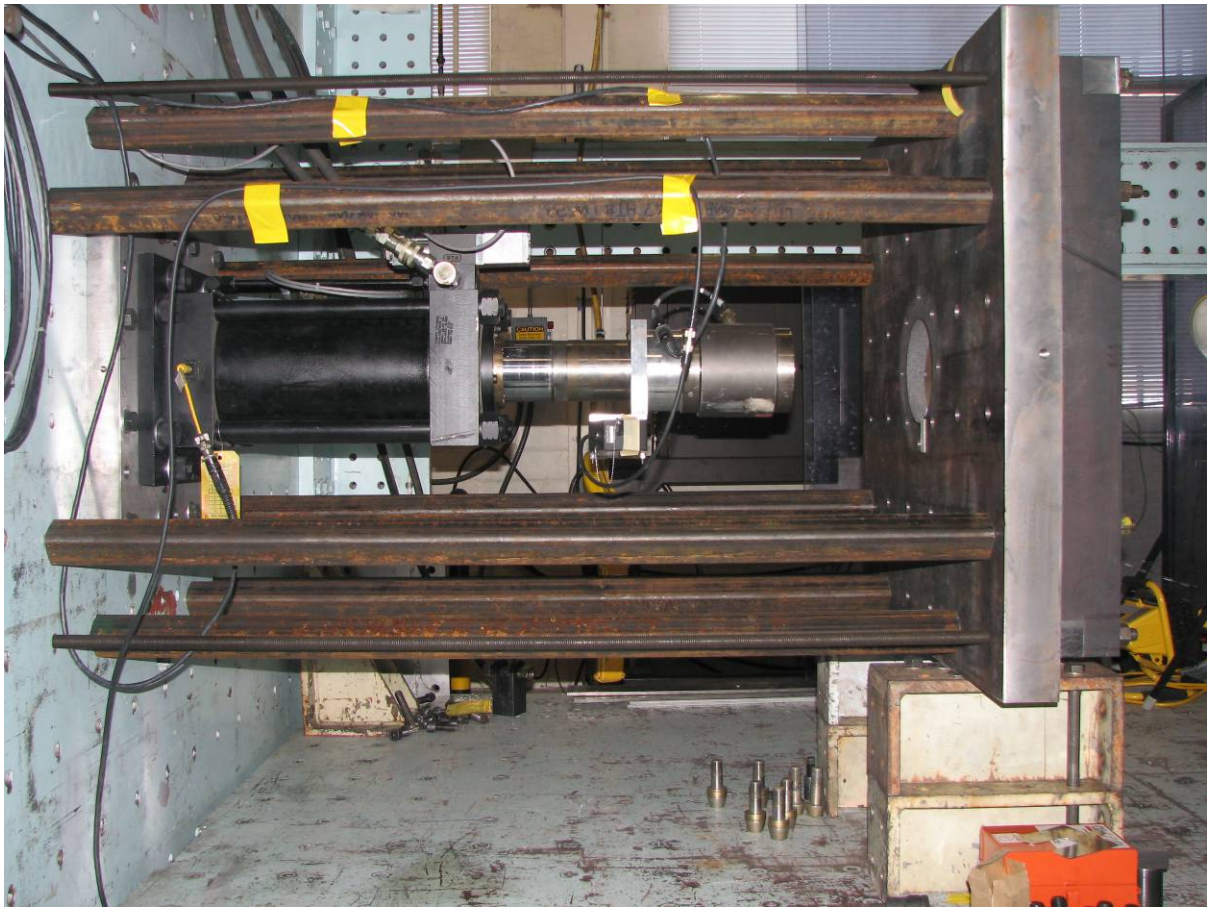

Figure 19. Quasi-static punch plate test setup

Each punch was threaded into the end of the actuator and aligned with the center hole of the mounting plate thus allowing the punch to pierce the center of each plate tested. Displacement control was implemented with an actuator stroke rate of 2 one thousandths of an inch per second (mils/sec) and increased to 40 mils/sec after the punch pierced the plate.

Preliminary testing in the 220 kip uniaxial load frame provided proof that a stronger bonding agent was not necessary. Strain gages were initially applied only to the punch side of the plate to allow full visibility of the opposite plate side for DIC purposes.

Figure 20 shows the cylindrical punch against a mild steel plate using the initial strain gage (SG) layout.

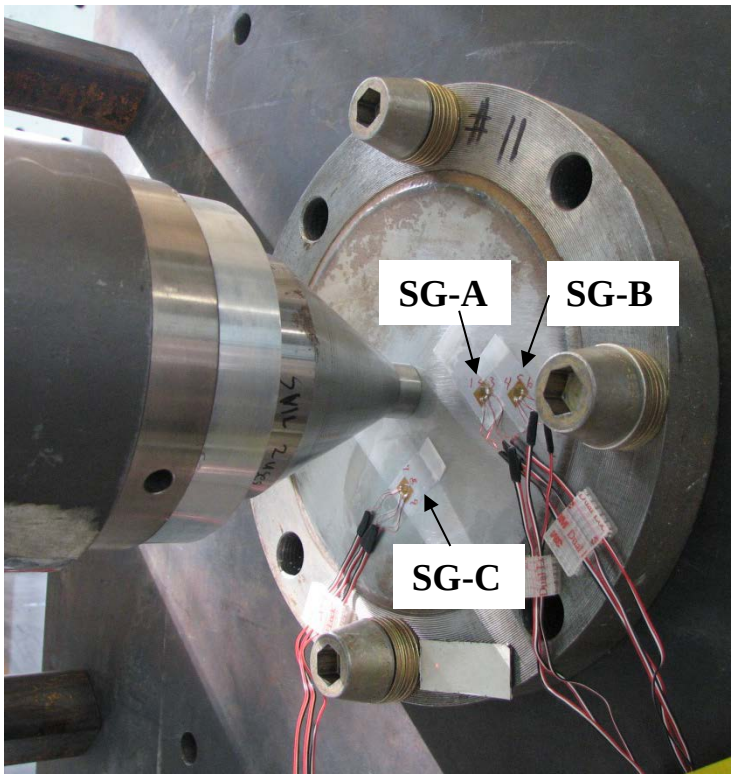

Figure 20. Instrumented punch plate

The same general gage setup shown in Figure 20 was used for the conical punch and is not shown here. Each plate tested quasi-statically contained three rosette strain gages (Micro-Measurements C2A-06-125WW-350). Two of the strain gages were placed along the 0º axis (i.e., parallel to the floor) at distances of 1.75 and 2.5 inches from the center of the punch plate. The third strain gage was rotated clockwise along the plate's surface from the 0º axis by 90° at a distance of 1.75 inches from the center of the plate. Those plates listed in Table 3 that employ three strain gages use the strain gage layout in Figure 20. Those plates listed in Table 3 employing five strain gages used the strain gage pattern shown in Figure 21.

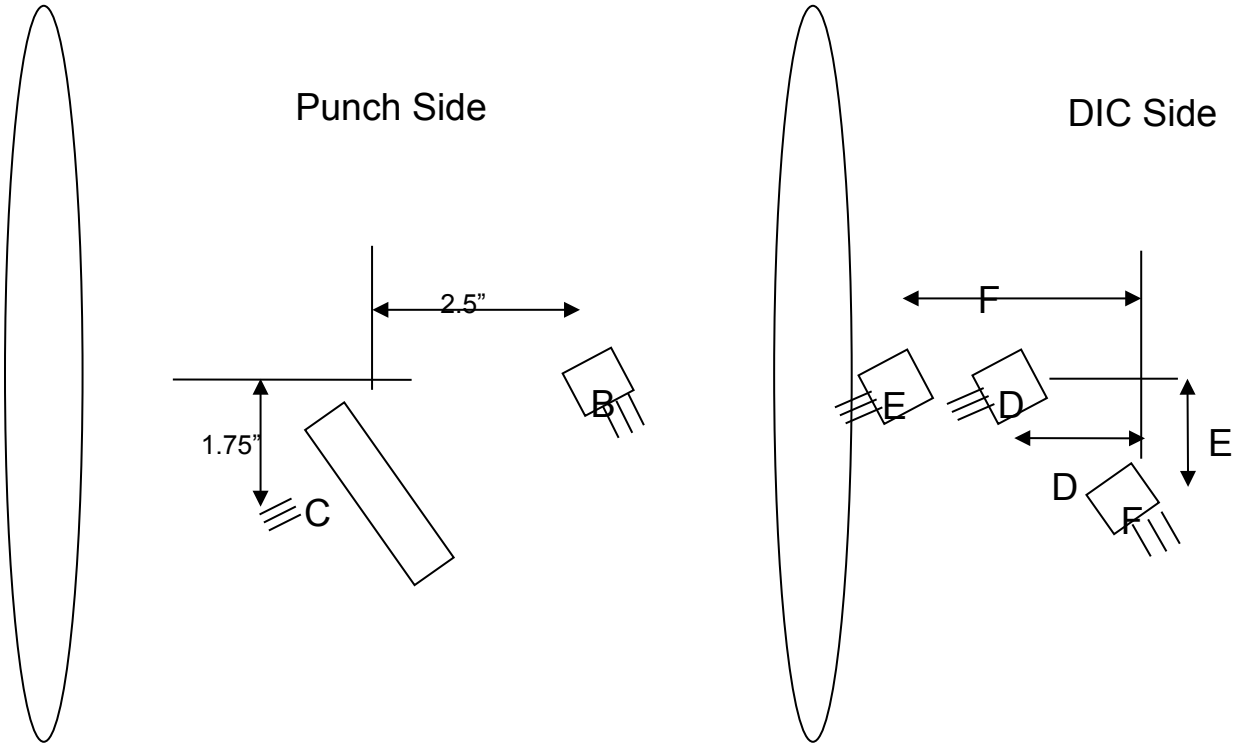

Figure 21. Strain gage location for plates instrumented on both sides (i.e., using 5 gages)

This strain gage pattern shown in Figure 21 placed three strain gages on the DIC side of the plate and two on the punch side. This layout shown in Figure 21 is referred to in the DIC analyses sections presented later.

2.1.2 Digital Image Correlation Setup for Quasi-Static Tests

Digital image correlation (DIC) was used to measure the full-field results from the front surface of the deforming plate (with the front being defined as the side opposite the punch). DIC is a photogrammetric technique using a calibrated camera pair, so-called stereo cameras, to image the deforming sample. Using the stereo images, quantitative, full-field three-dimensional (3-D) information can be extracted and displayed.

Most of the quasi-statically tested plates incorporated DIC to acquire test information. Initially, it was thought that placing instrumentation such as strain gages on the DIC face of the plates would cause interference and bias in the DIC data. However, post-processing of the data revealed that the plates did not model thin-membrane behavior, and additional instrumentation to validate the DIC results was needed. Thus FY09 testing incorporated strain gages to the front (i.e., speckled side) of the plate to resolve strain discrepancies between the front and back locations. An enormous amount of DIC data were available for each test, and only highlights are presented in this document.

For the quasi-static testing of the plates, high-resolution cameras were used to increase both the spatial resolution and the measurement resolution of the system. The optical setup consisted of two 4-megapixel Redlake cameras, which are shown in Figure 22. These were used in conjunction with DIC software from Correlated Solutions, Inc.

The cameras were placed in front of the samples, and the samples were illuminated with indirect lighting to provide an even light over the surface, minimizing any highlights during the deformation. Preparation of the samples for the DIC measurements consisted of a light sanding and cleaning with alcohol before coating with an SEM brand metal primer and then speckled with a contrasting color (see Figure 22). A Keyence sensor was also used with a limited number of samples to measure the center deflection as illustrated in Figure 22. A comparison could then be made between three or four independent measurements, the DIC results extracted at the center, the Keyence detector, the stroke on the load hydraulics, and on some tests, the LVDTs.

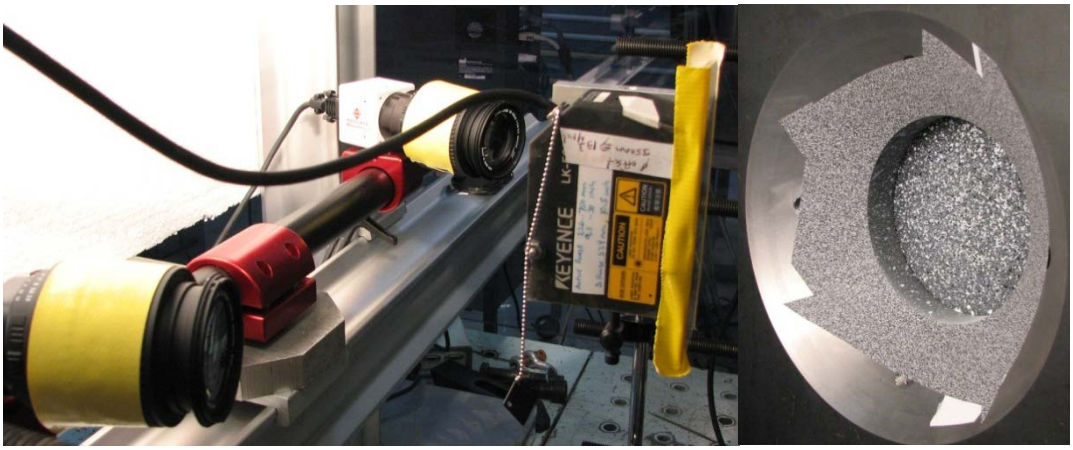

Figure 22. Camera setup and Keyence sensor looking at a speckled sample mounted in the test fixture

2.1.3 Quasi-Static Test Instrumentation

A Keyence laser sensor was used to measure the relative displacement between the actuator and the edge of the plate being tested. The laser can be seen in Figure 20 reflecting off the white magnet located on the lower region of the plate's flange. Other instrumentation in FY08–FY09 included rosette strain gages that were bonded to the punch and DIC sides of the plates using M-bond 200. A Bessel low-pass filter was used for the strain gage data. Three channels were recorded for each strain gage, and the principal strains and principal angles were calculated from these readings. Test equipment included an MTS Flex Test GT controller, a Parker 150 kip portable actuator, a Lebow load cell (Model #3156) with a calibration expiration date of 20 May 2009, and an HBM MGCplus data acquisition system. Servo-hydraulic control was used for all tests. Load, displacement, and strain gage data were recorded for each quasi-static test and are presented with the experiment results.

2.2 Quasi-Static Punch Plate Testing

2.2.1 Quasi-Static Tests Performed

Quasi-static testing was initiated in the 220 kip uni-axial load frame to determine the maximum load achieved for each material. This initial testing required the rewelding of the abrasion-resistant plate to the flange because separation at the union was evident (see Figure 23).

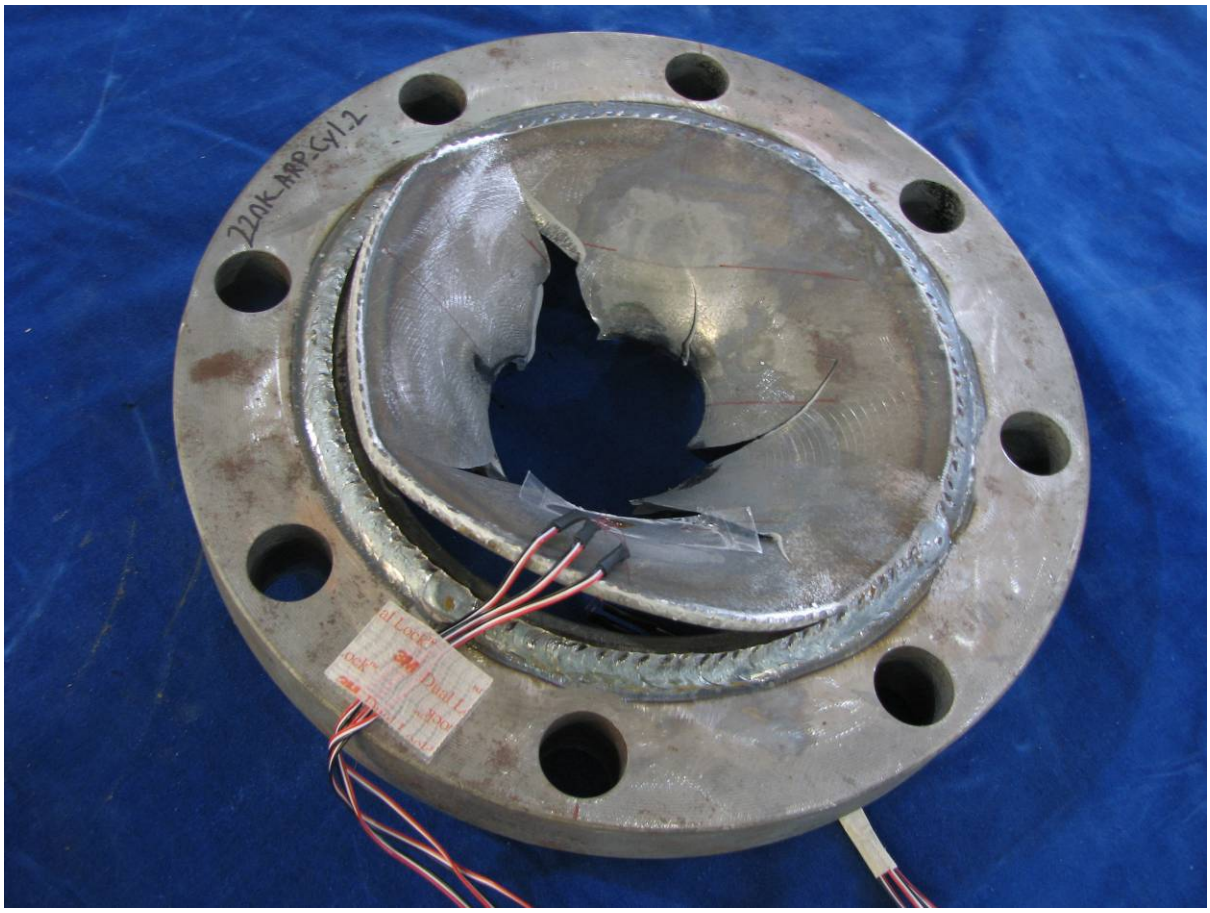

Figure 23. Weld failure for cylindrical punch on ARP

As a result of the higher load reached with the cylindrical punch and the uncertainty that the weld on the abrasion-resistant steel plates would remain intact, further cylindrical punch tests through the abrasion-resistant material were not performed. Table 3 lists the plates tested in the Structural Frame with the associated dimensions and reference file names.

Table 3. FY08–FY09 Quasi-Static Test Matrix

Steel Type	Plate Number	Plate Thickness (inch)	Number of Strain Gages	Punch Type	File Name
Mild	1	0.060	3	Conical	16MS-Con-1
	2	0.060	3	Cylindrical	16MS-Cyl-2
	3	0.060	3	Conical	16MS-Con-3
	7	0.060	3	Cylindrical	16MS-Cyl-7
	8	0.060	3	Conical	16MS-Con-8
	9	0.060	3	Cylindrical	16MS-Cyl-9
	10	0.060	3	Conical	16MS-Con-10
	11	0.060	3	Cylindrical	16MS-Cyl-11
	MS101	0.060	5	Conical	MS-Con-101
	MS102	0.060	5	Conical	MS-Con-102
	MS103	0.188	5	Cylindrical	MS-Cyl-103
	MS104	0.188	5	Cylindrical	MS-Cyl-104
Abrasion-Resistant	4	0.188	3	Conical	ARP-Con-4
	5	0.188	3	Conical	ARP-Con-5
	6	0.188	3	Conical	ARP-Con-6
	ARP101	0.060	5	Conical	ARP-Con-101
	ARP102	0.060	5	Conical	ARP-Con-102

All gages used on the plates were rosette gages. Those plates that show five strain gages in Table 3 contained three strain gages on the DIC side of the plate and two on the punch side. The strain gage locations for the punch side are depicted in Figure 21. Those plates containing only three strain gages did not have any of the gages on the DIC plate side.

A total of seventeen quasi-static tests on the metal plates were completed in FY08–FY09 on the Structural Frame. These included twelve mild steel plates and five abrasion-resistant plates.

2.2.2 Anomalies from Quasi-Static Tests

The thinner mild steel plates produced petaling failure patterns in the material as the punch was moved through the plate. This was the case for both punches used (i.e., cylindrical and conical). An anomaly was observed with one mild steel plate that produced a five-petal pattern (see Figure 24, upper left image) that had not been observed in the FE simulation model. This phenomenon provoked further testing in an attempt to replicate the pattern. Although the boundary conditions, actuator stroke rate, and pierce location remained the same for each test, the five petal pattern could not duplicated.

After a test of an abrasion-resistant steel plate, slight movement in the entire quasi-static test setup was observed and required a realignment of the setup. The variation in the spiraled failure patterns of these thicker and stronger plates may have been influenced by the movement in the setup. It would be prudent for further testing of these plates to be repeated with modifications made to the setup to prevent movement of the actuator perpendicular to the direction of travel through the plate.

2.2.3 Observations from Quasi-Static Tests

Different failure behaviors were observed between the two dissimilar metals. A petaling pattern was seen with the conical and cylindrical punches for the mild steel material. Figure 24 and Figure 25 display post-test pictures of some of the mild steel plates tested that display this phenomenon.

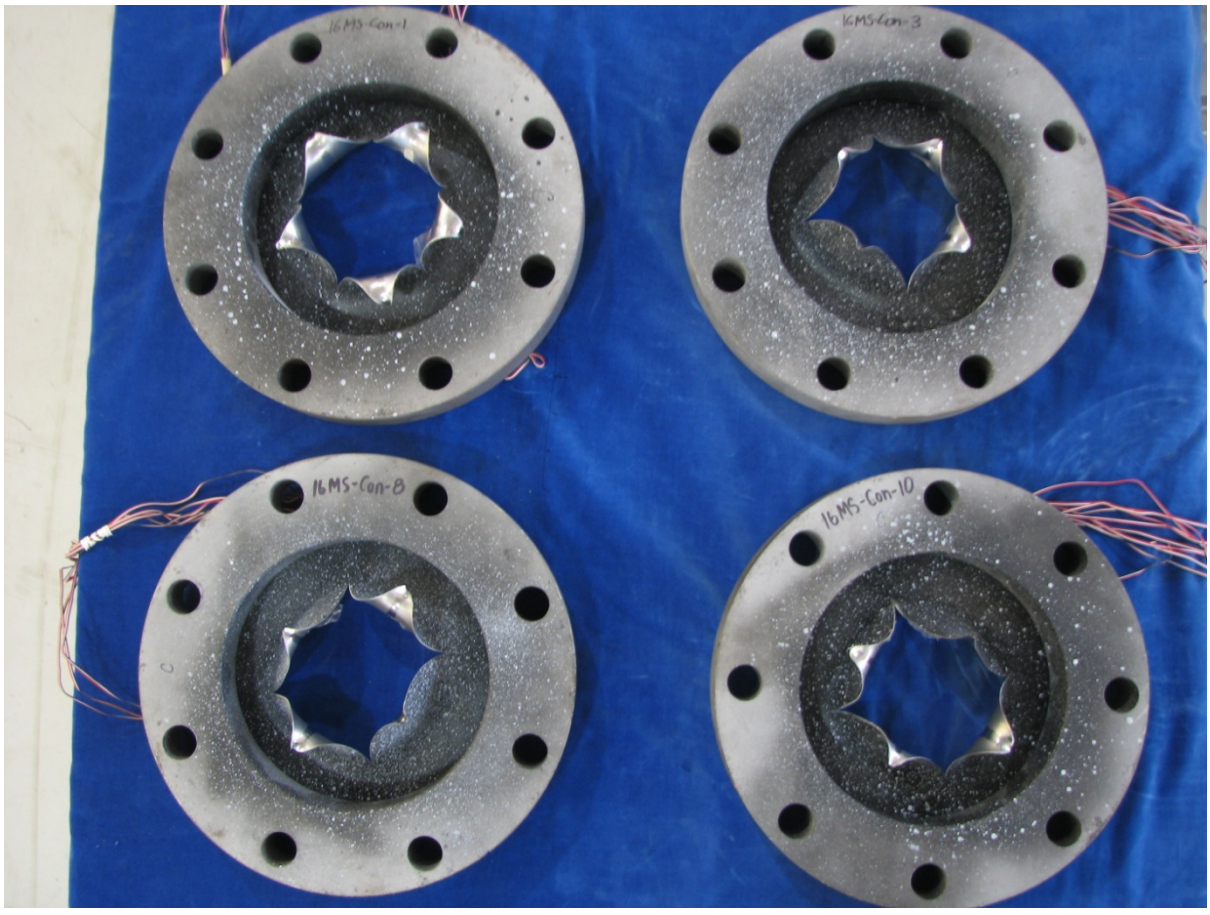

Figure 24. Mild steel plates punched with conical punch

MS-Con-101 and MS-Con-102 produced similar patterns to those shown in Figure 24. Similar to the plates tested using the conical punch, the cylindrical punch produced a comparable failure pattern as shown in Figure 25.

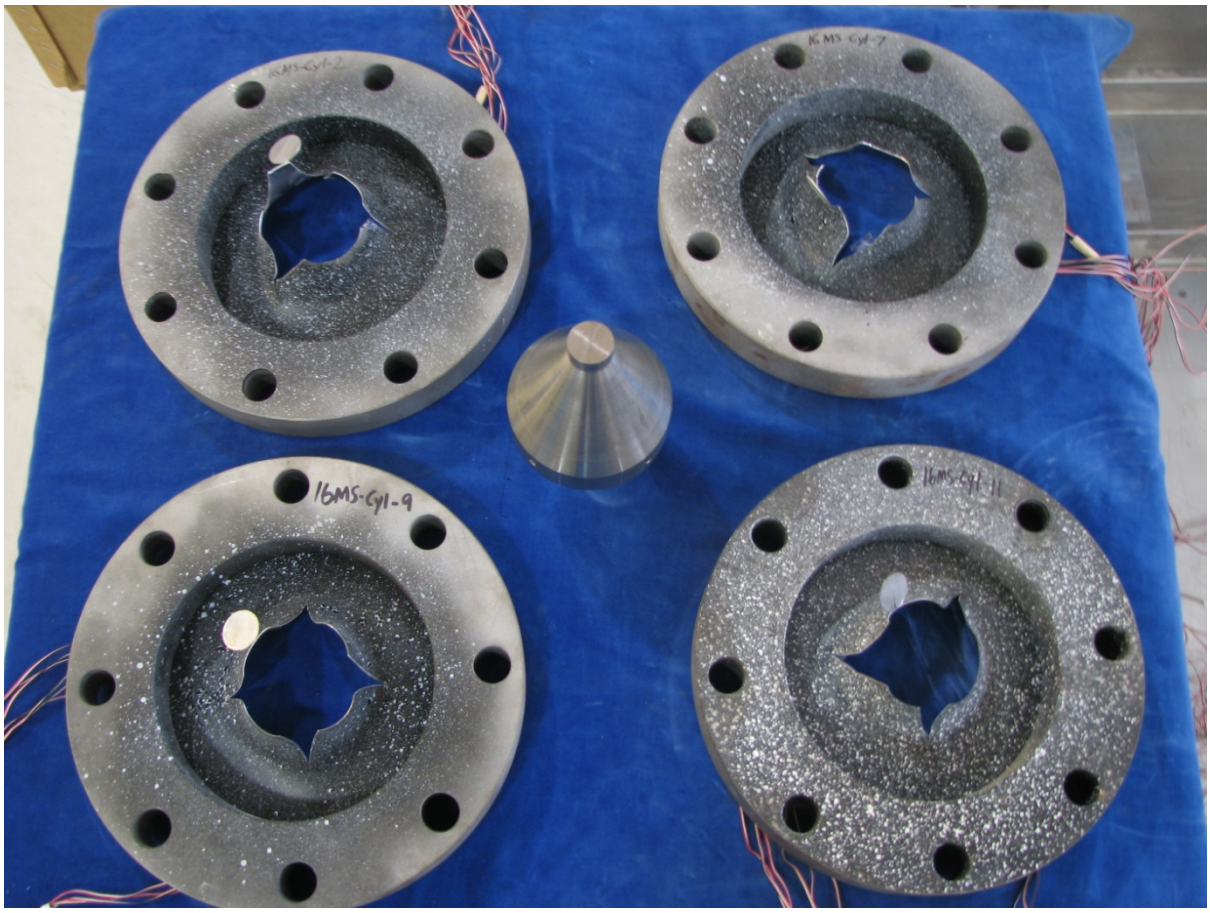

Figure 25. Mild steel plates punched with cylindrical punch

MS-Cyl-103 and MS-Cyl-104, which are not shown in the preceding figures produced patterns similar to the other plates tested with a cylindrical punch. An overall general petaling pattern was noted when the cylindrical punch was used. In all cases, a center circular area matching that of the punch end surface remained attached to the metal. Two of the cylindrical-punched plates (the upper left and lower left images in Figure 25) produced four petals. The other two plates produced three petals. Four petals were produced on MS-Cyl-103 and MS-Cyl-104. The punch used for testing is shown in the center of Figure 25.

Unlike the mild steel, the abrasion-resistant steel produced vastly different failure patterns as shown in Figure 26. Only the conical punch was used during testing of this material.

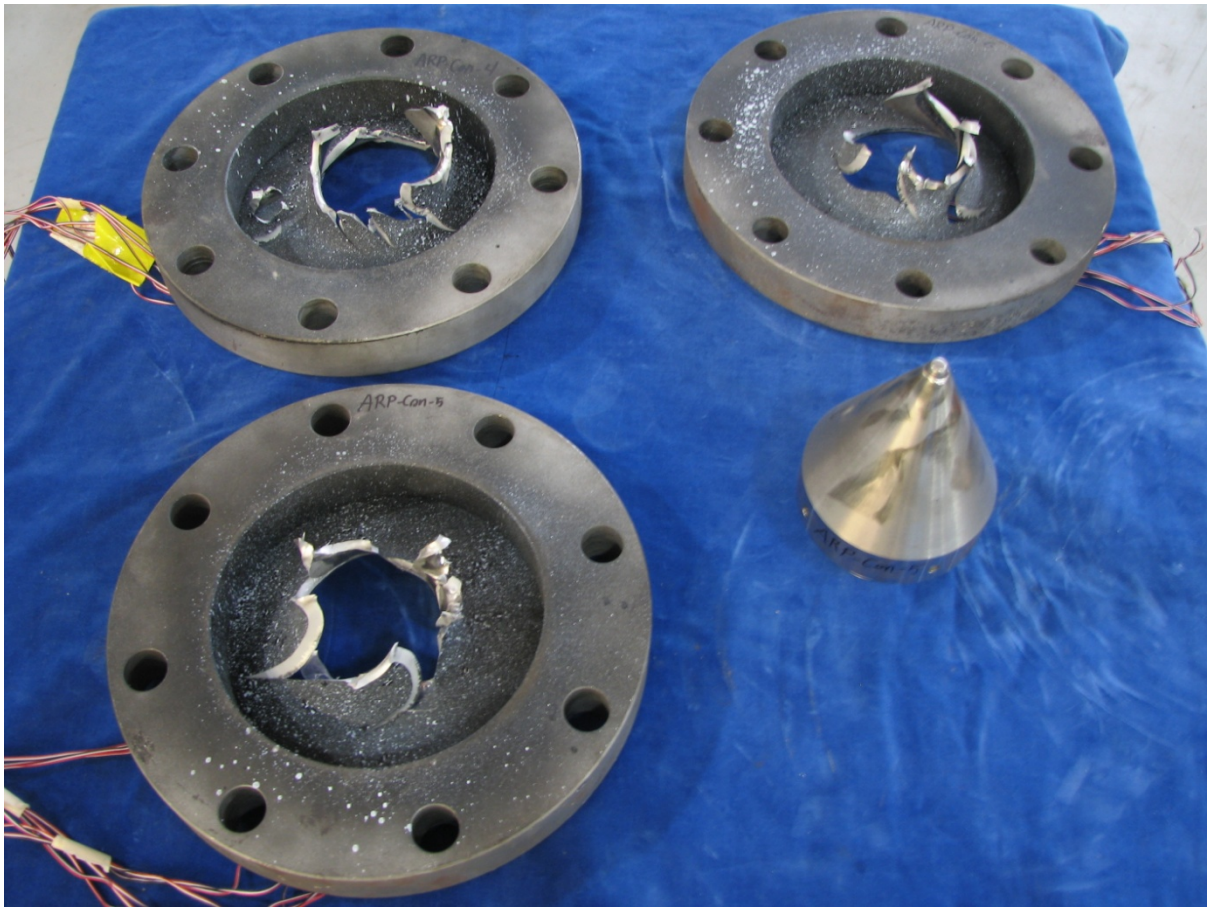

Figure 26. Abrasion-resistant steel punched with a conical punch

A punch used for a single test is shown in Figure 26. It is immediately obvious that the punch incurred damage from testing. As a result, a conical punch was only used for one test. It was initially suspected that the punch rotated during contact with the plate, so the other punches used for the final abrasion-resistant plate tests were marked to determine whether the spiraled petaling on the plates was caused by punch rotation. The mark placed on the punch, however, indicated that the punch had not rotated, and the spiral affect could, therefore, not be attributed to the movement of the punch itself. ARP-Con-101 and ARP-Con-102, which are not shown in here, displayed failure patterns similar to those shown in Figure 26.

2.3 Load versus Displacement

The load versus displacement response for the mild steel plates that were pierced with the conical punches are shown in Figure 27. Although Plate 1 produced the five petals versus the four produced by the other plates, it is not obvious from the data as to the reason for this result.

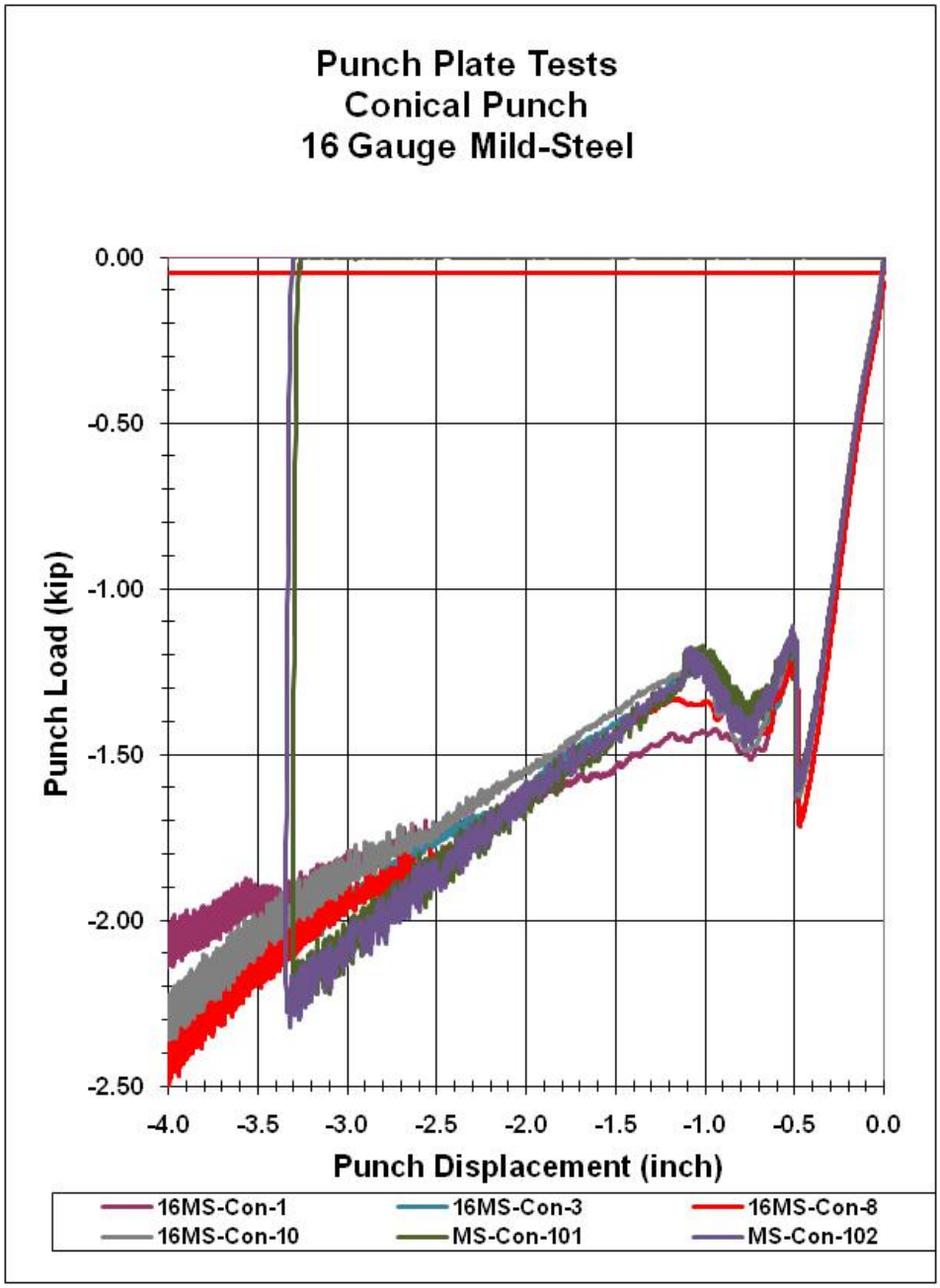

Figure 27. Load versus displacement response for mild steel plates punched with a conical punch

The load applied to the plate was a compressive load. The *y* axis (i.e., *Punch Load*) in the plot of Figure 27 is shown as negative and is in units of kip: as such, a higher compressive load is indicated by a more negative number. The distance between the punch and the plate decreased as the plate pushed into the punch. MS-Con-101 and MS-Con-102 commanded the punch to travel a total of 3.25 inches, versus the 4 inches commanded travel for the other plates shown in Figure 27. This compressive load continued to increase until the punch pierced the plate. The plate experienced elastic recovery and rebounded back. Because the conical punch increased in diameter, the compressive load placed on the plate was quickly recovered. The curves begin to differ as the plate experiences petaling.

The results from testing of the mild steel plates with cylindrical punches are shown in Figure 28.

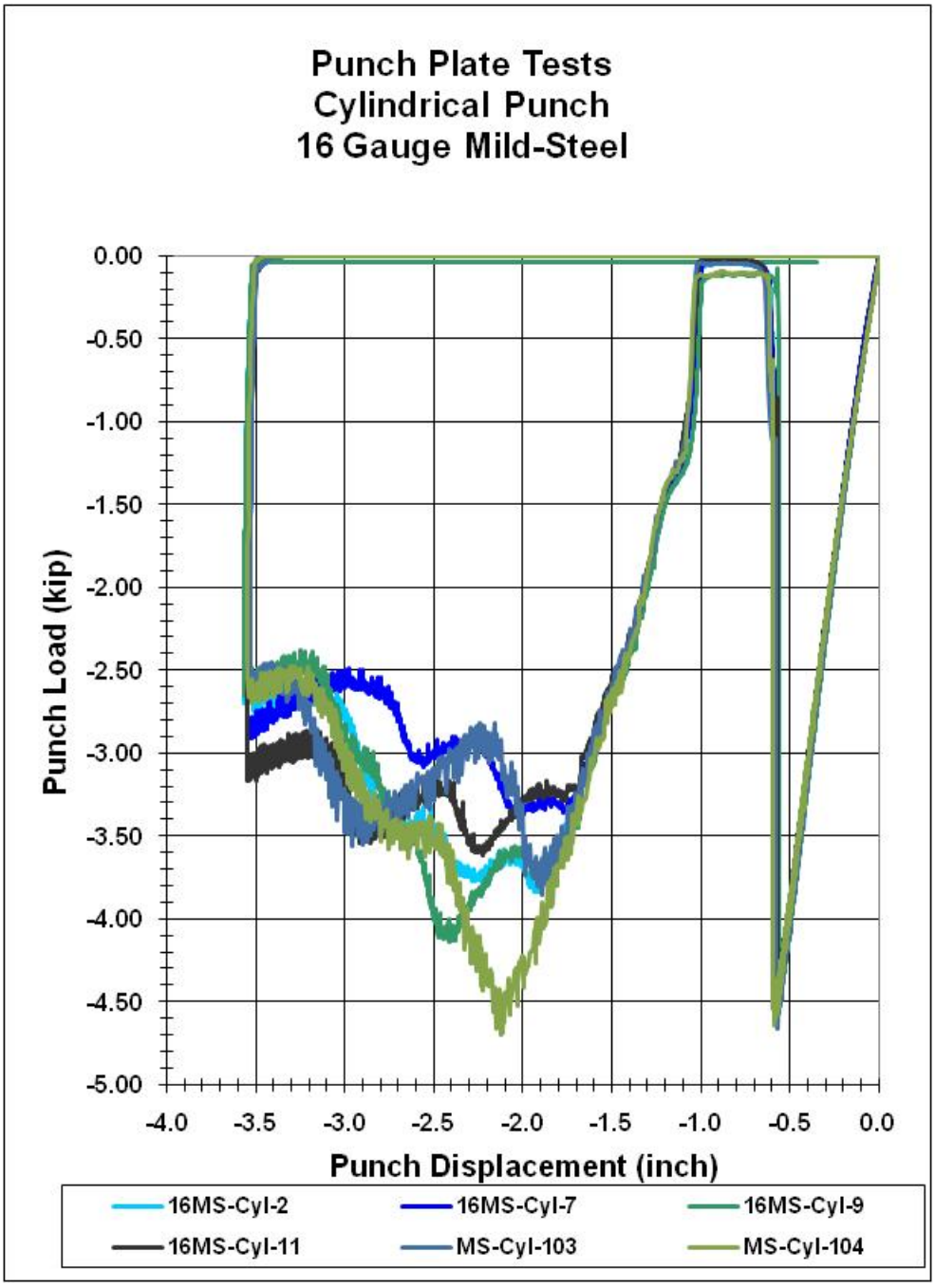

Figure 28. Load versus displacement behavior for mild steel plates punched with a cylindrical punch

As the actuator moved closer to the plate, the distance between the two decreased, so moving from right to left in Figure 28 provides a chronological sequence of events. As the cylindrical punch contacted the plate and pushed on the plate, the load applied to the plate increased until it reaches a maximum load. Once the circular area of the punch end pierced the plate, the load immediately decreased (at ~ −0.6 inches, see Figure 28) from this maximum load.

The cylindrical punch allowed more rebound of the plate because the diameter of the punch was constant along the cylinder, and the plate is allowed to move back to a zero-load condition. Thus the compressive load on the plate is lost. The load remained near zero until the tapered region of the punch began to engage the plate, at which point the compressive load rose again. Once petaling began, variations in the failure behavior are indicated by curve deviations. As shown in Figure 28, all failure patterns closely follow one another until petaling occurred.

Initially the load versus displacement behavior for the abrasion-resistant plate behaved similarly to the mild steel but with much higher loads achieved (see Figure 29).

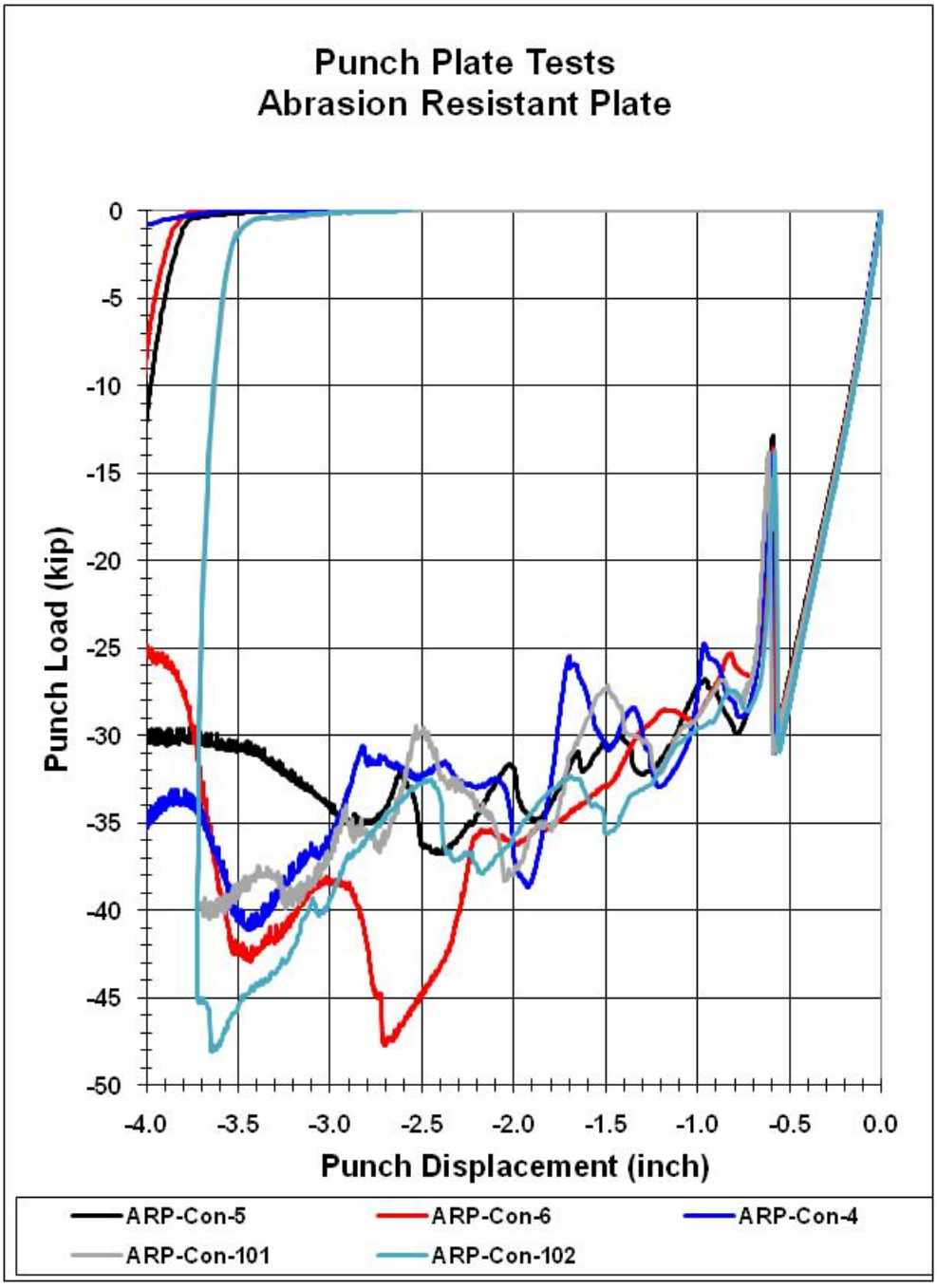

Figure 29. Load versus displacement response for abrasion-resistant steel punched with a conical punch

The thickness as well as the strength of the abrasion-resistant material contribute to the higher loads achieved as compared to the mild steel. Similar to the mild steel plate behavior, load is lost after the punch pierces the plate. As the plate experiences petaling or spirals in this case, the curves begin to differ, and the differences are quite large and sporadic.

2.4 Strain Analysis for Mild Steel Plate 102 with Punched with a Conical Punch

Strain channel readings for the radial, circumferential, and 45° axes were obtained for each working rosette strain gage. The principal strains and principal strain angles were calculated from the three measured channels. Results for the radial strain of mild steel Plate 102 punctured with a conical punch is shown in Figure 34. Responses for other mild steel plates pierced by a conical punch are similar to those shown in the figures below and are, therefore, not presented nor are they discussed in this document.

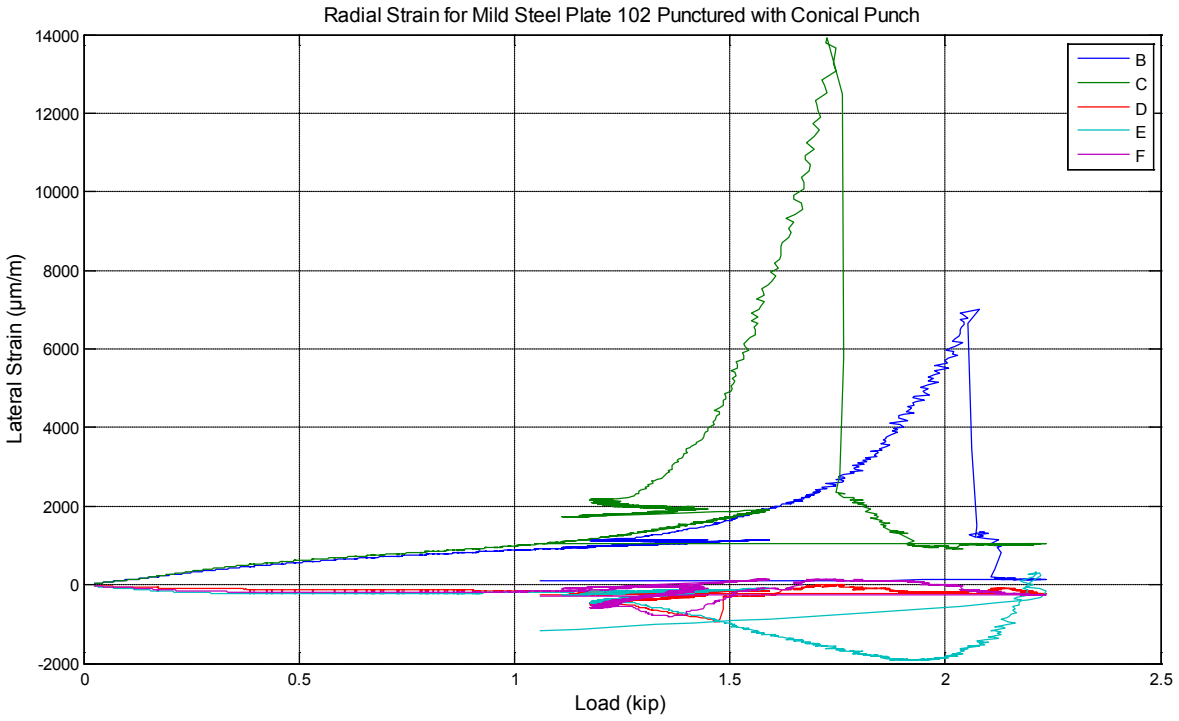

Figure 30. Radial strain for mild steel Plate 102 punched with a conical punch

Referring back to Figure 21, which laid out Gages B and C on the punch side of the plate and the remaining gages on the DIC plate side, it makes sense that the radial strains on the punch side, i.e., the side with Gages B and C, reflect higher strains and an elongation in the material. Material along radial axes on the punch side of the plate, denoted by B and C, stretch while material along the same axes on the opposite side of the plate shorten in length. The material on the DIC speckled side of the plate compresses as the punch pierces through as indicated by negative strain readings. The strain gage magnitudes of Gages E and F are not comparable to Gages B and C, respectively. These differences in strain magnitudes show the effect that the thickness of the material has on the plate behavior and reveal that a thin-membrane assumption for failure prediction is not applicable. Strain Gages B and C were located closest to the punch contact and are thus greater in magnitude than strains registered by Gages D, E, and F.

Similar behaviors are noted for the circumferential readings for each side of the plate as presented in Figure 31.

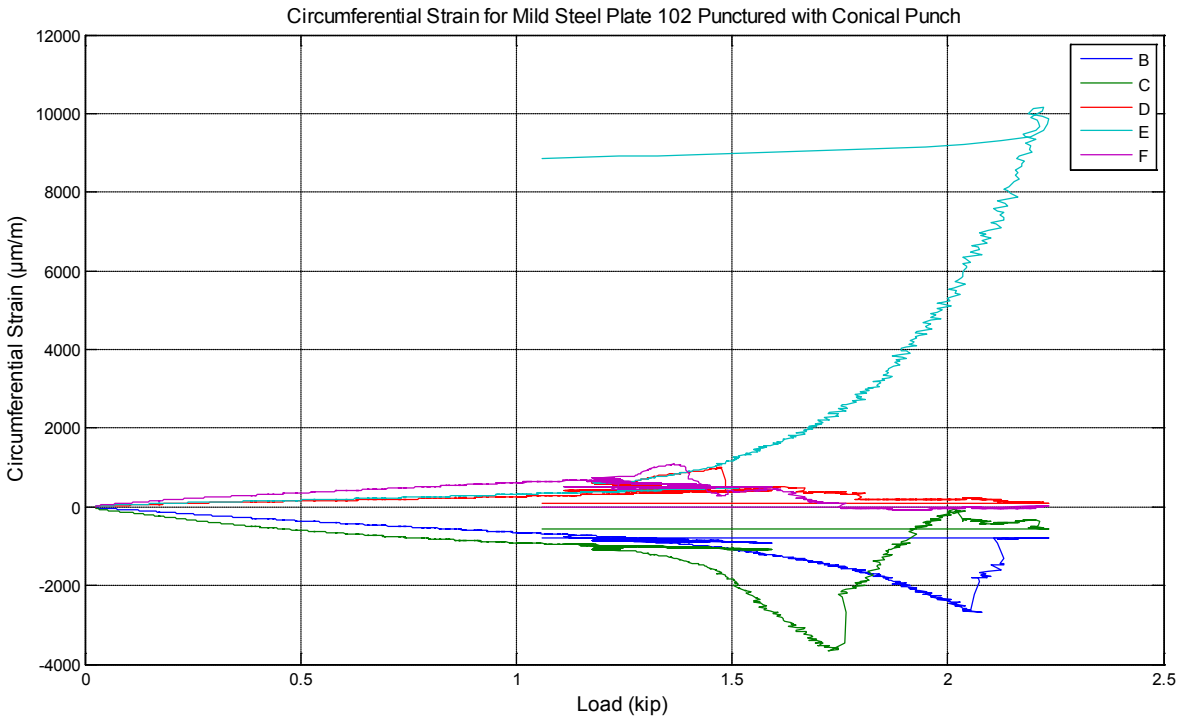

Figure 31. Circumferential strain for mild steel Plate 102 punched with a conical punch

Material in the circumferential orientation on the punch side, denoted by B and C, experienced compression while material on the opposite side of the plate with the same circumferential orientation elongated. Once again, the strain values are slightly higher on the punch side as compared to the DIC side, but the general strain response behaviors observed on one side of the plate appear to be mirrored by those on the opposite side until puncture of the plate.

Consistency in the cluttering of strain readings are again obtained for the 45° reading of the rosette gages as shown in Figure 32.

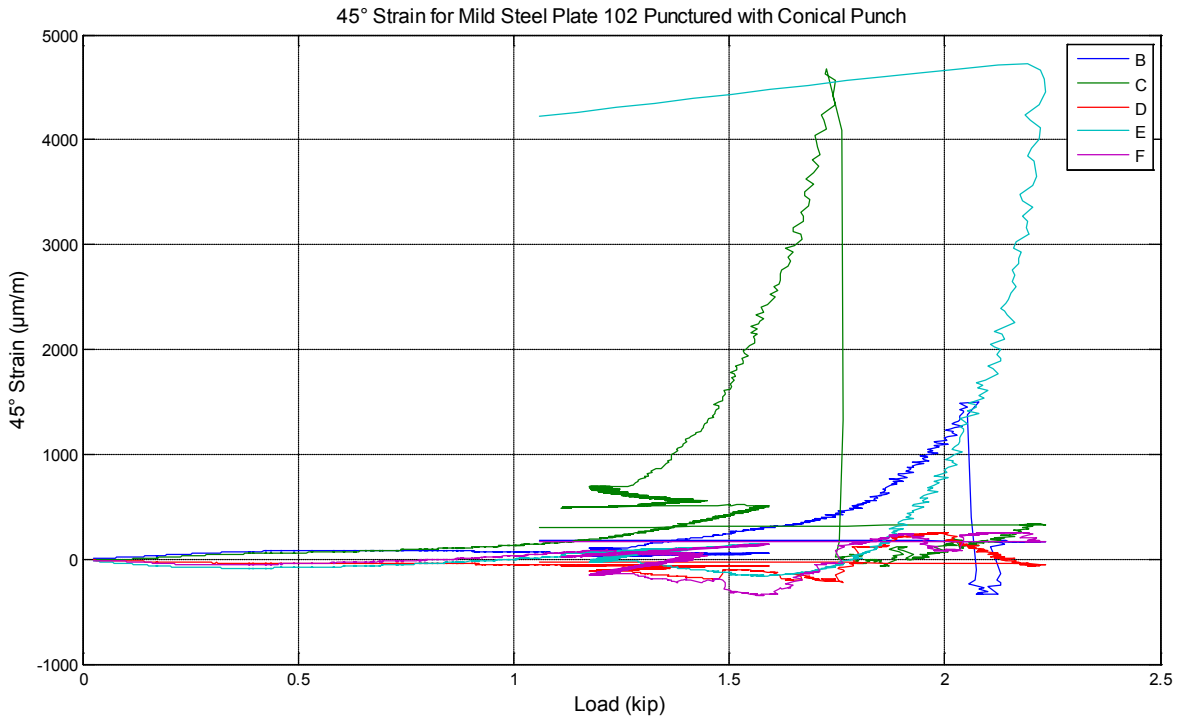

Figure 32. 45° strain for mild steel Plate 102 punched with a conical punch

A similar response observed for the radial and circumferential strain is repeated for the 45° strain reading. The strains on one side of the plate are closely cluttered and mirrored by the readings on the opposite side of the plate. Comparisons of strains along these directions show very little difference in magnitude compared to those observed by the radial and circumferential readings.

A comparison of the principal strains as shown in Figure 33 and Figure 34 reveal similar response patterns for principal-1 and principal-2 calculated strains.

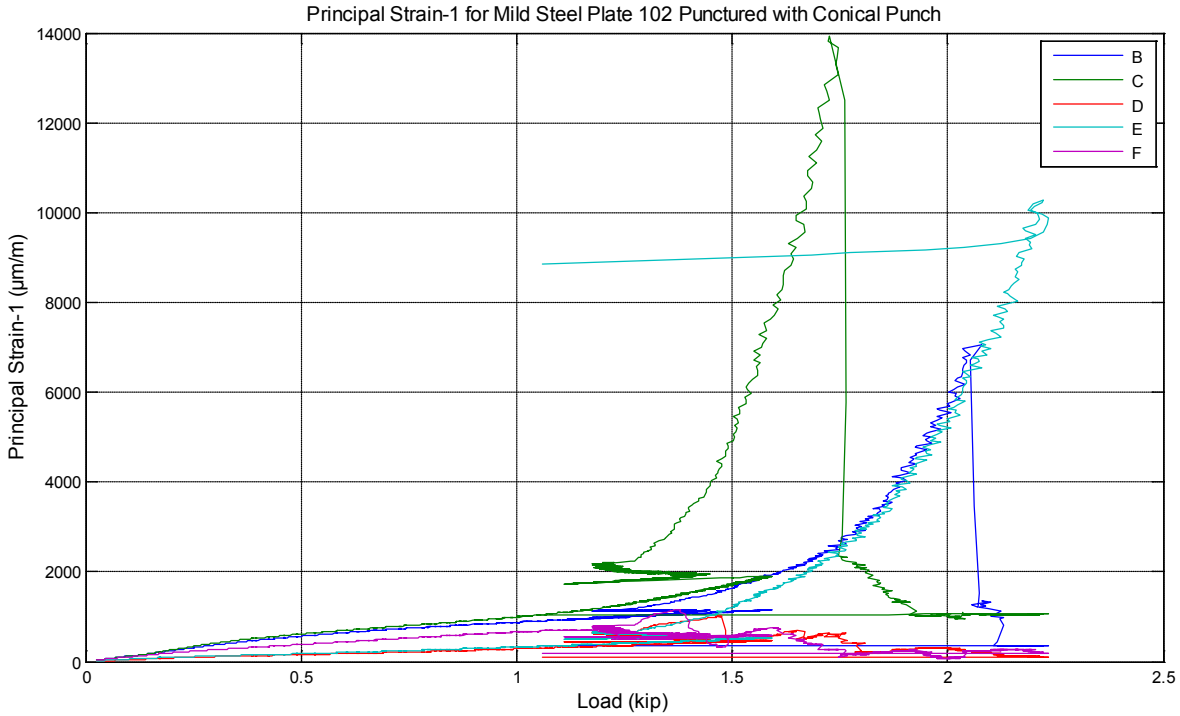

Figure 33. Principal strain 1 for mild steel Plate 102 punched with a conical punch

It should be noted from Figure 33 that the calculated principal-1 strain until puncture for Gage F differs significantly from Gages D and E. Given the axisymmetric geometry of the setup and the 1.75-inch location from the center of Gages D and F, it was expected that Gages D and F would have closer principal-1 strains than Gages D and E. Gage E was located along the same radial axis as Gage D but 0.75 inches further away from the center.

It is not surprising to notice that the calculated principal strain magnitudes are higher for those readings located on the punch side of the plate and, therefore, closer to the point of contact as again demonstrated in Figure 34 for the principal-2 strain.

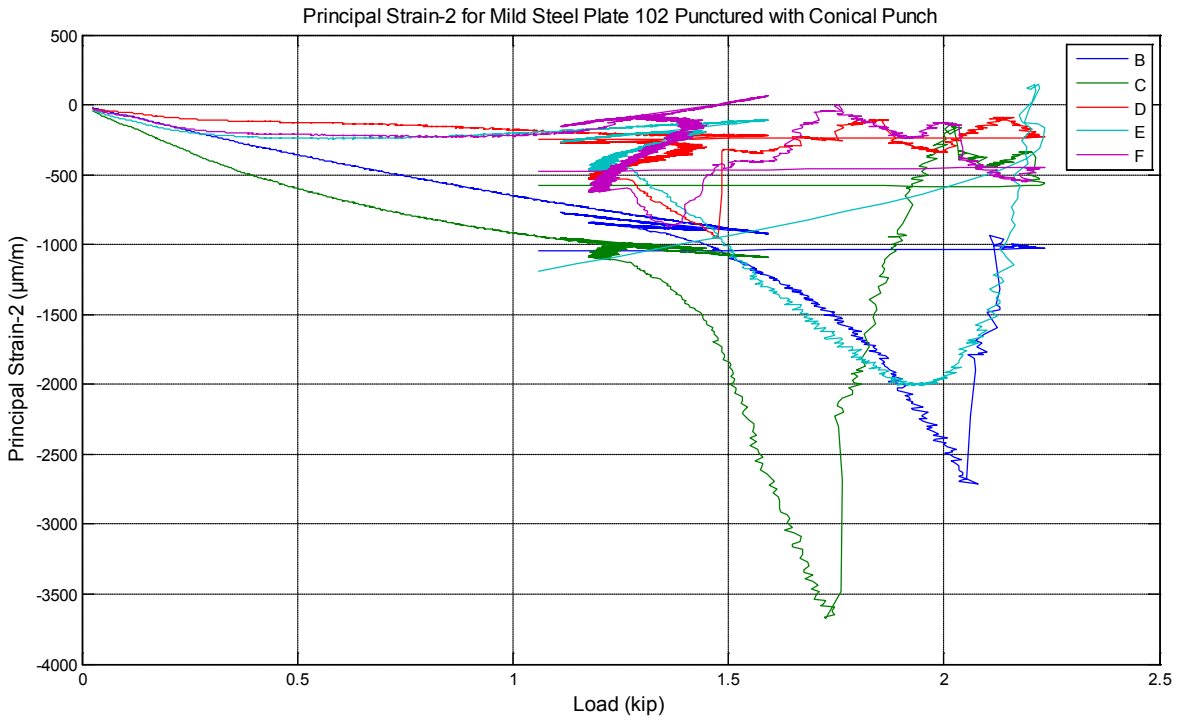

Figure 34. Principal strain 2 for mild steel Plate 102 punched with a conical punch

Again, Gages D and F show slightly different principal strain magnitudes. As with the principal-1 strains, principal-2 strains for Gages E and F are more alike than Gages D and F. After closer examination of the failed MS-Con-102 plate, it was noted that the line of fracture that spread further along the Gage F axis was comparable to the axis of Gages D and E. This may explain the increased strain illustrated in Figure 33 and Figure 34 for Gage F when compared to Gages D and E.

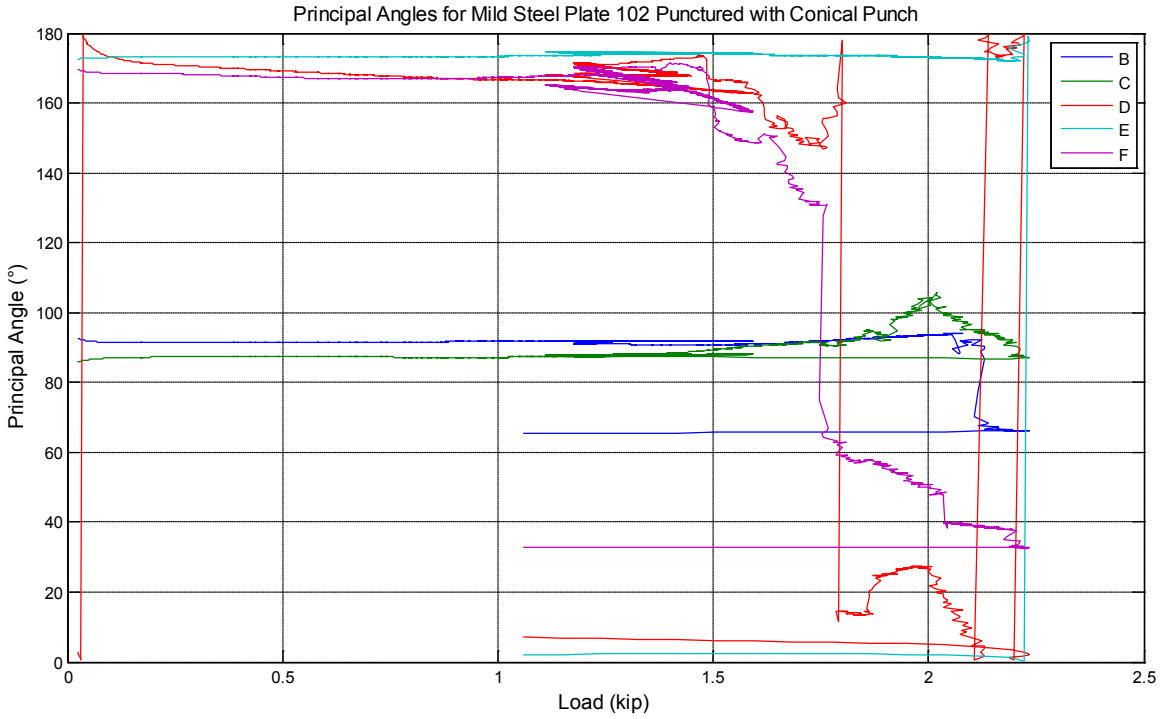

Figure 35. Principal strain angles for mild steel Plate 102 punched with a conical punch

As shown in Figure 35, the two gages located in the punch side of the plate have similar principal angles. The gages on the DIC side of the plate were a mirror image of those on the punch side and would present principal angles 90° off from those on the punch side. Interpretation of Figure 35 indicates that all principal angles point toward the center of the plate, just as was observed in the heavily gaged FY07 plate (see Figure 1).

2.5 Strain Analysis for Mild Steel Plate 104 Punched with a Cylindrical Punch

As with the mild steel punched with a conical punch, the mild steel plate punched with a cylindrical punch produced symmetric results. A look at radial and circumferential strains gives a better understanding of the symmetry in failure (see Figure 36 and Figure 37).

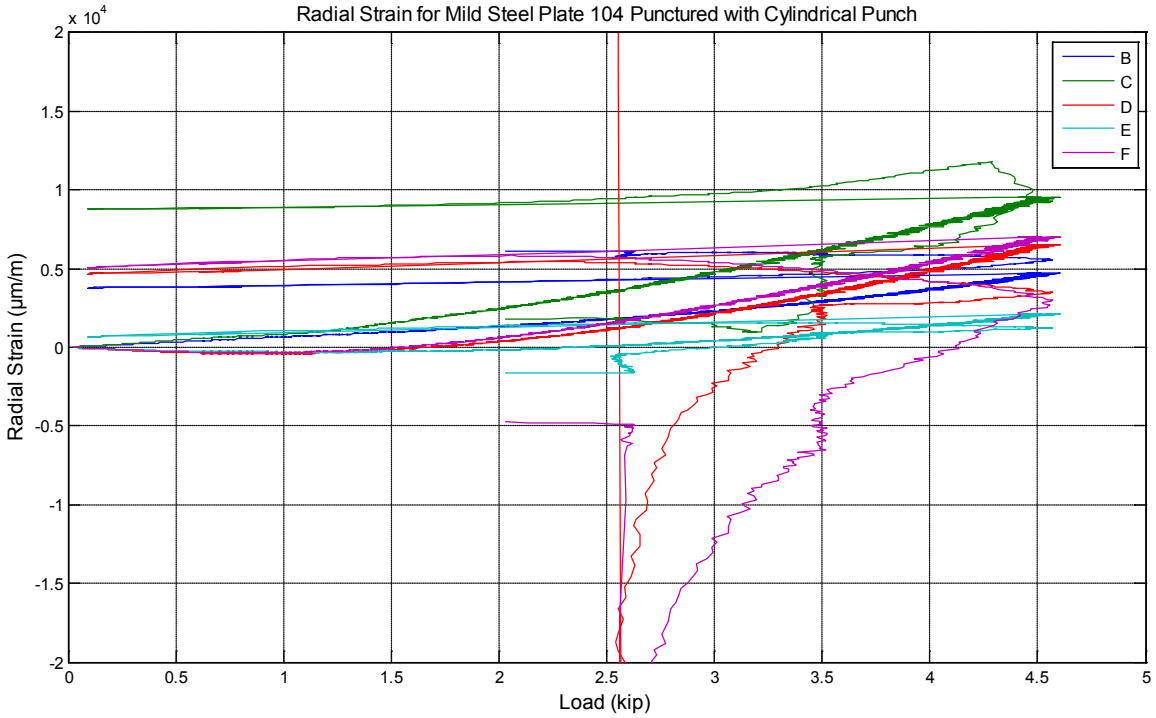

Figure 36. Radial strain for mild steel Plate 104 punched with a cylindrical punch

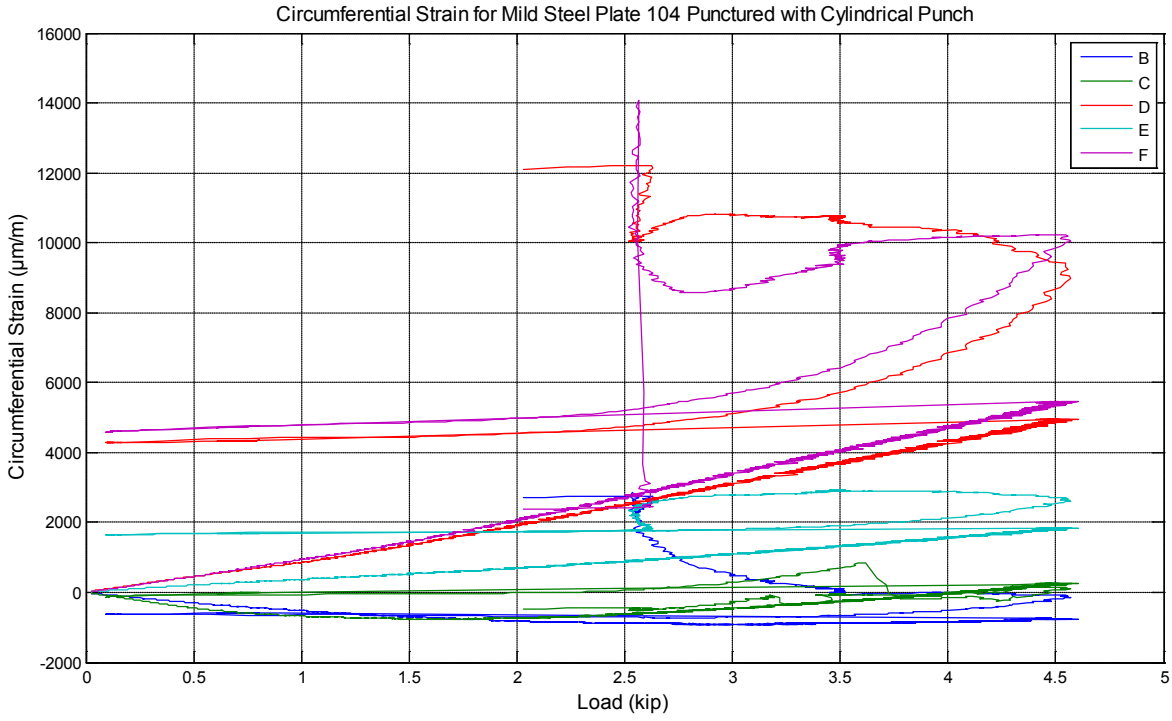

Figure 37. Circumferential strain for mild steel Plate 104 punched with a cylindrical punch

As shown in Figure 36 and Figure 37, strains on the punch side of the plate are again higher than on the DIC side. More symmetry is observed between Gages D and F than when the mild steel was punched with a conical punch. Petaling of this plate did not create cracks along the strain gage axes in this case. Strain gage readings for the axis lying between the circumferential and radial readings are shown in Figure 38.

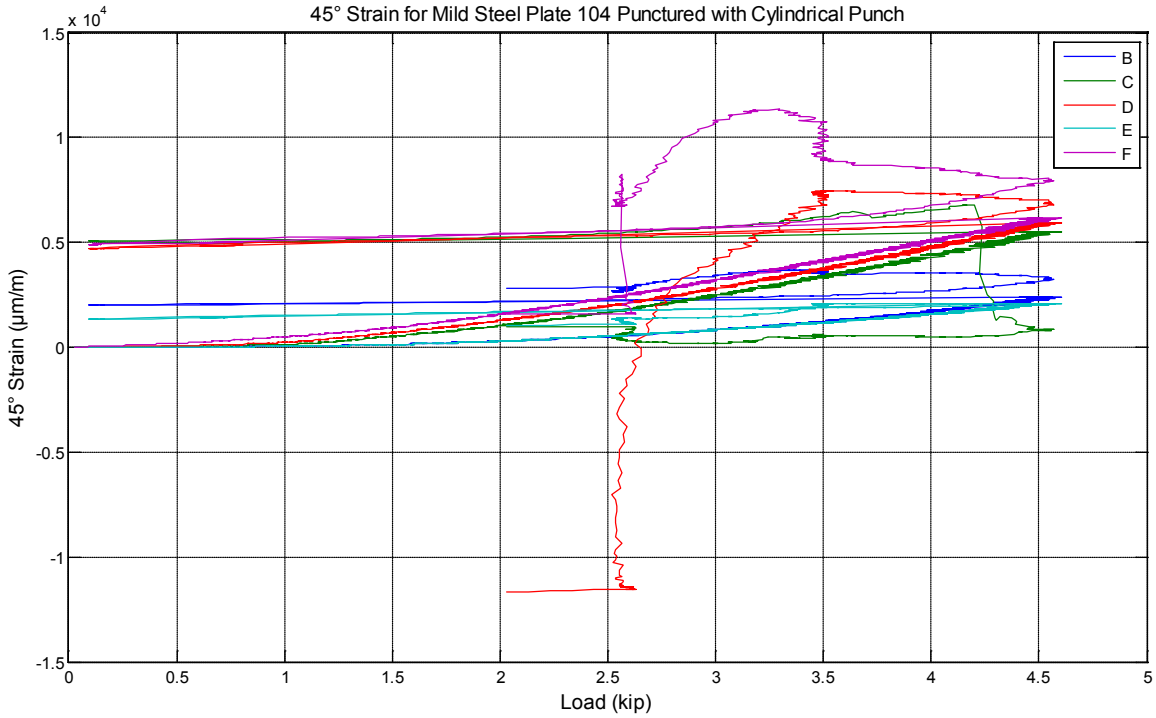

Figure 38. 45° strain for mild steel Plate 104 punched with a cylindrical punch

As shown in Figure 38, the gages located further from the center appear to be grouped together. There is no distinguishable difference of readings based on which plate side the gages resided. Instead the distinguishing characteristic and grouping of gages is based on their location from the center of the plate. Gages C, D, and F, which are 1.75 inches from the plate's center are closely clustered. Gages B and E, located 2.5 inches from center, are grouped together with smaller strains than those located nearer to the plate center. Principal strains and principal angles are displayed in Figure 39 through Figure 41.

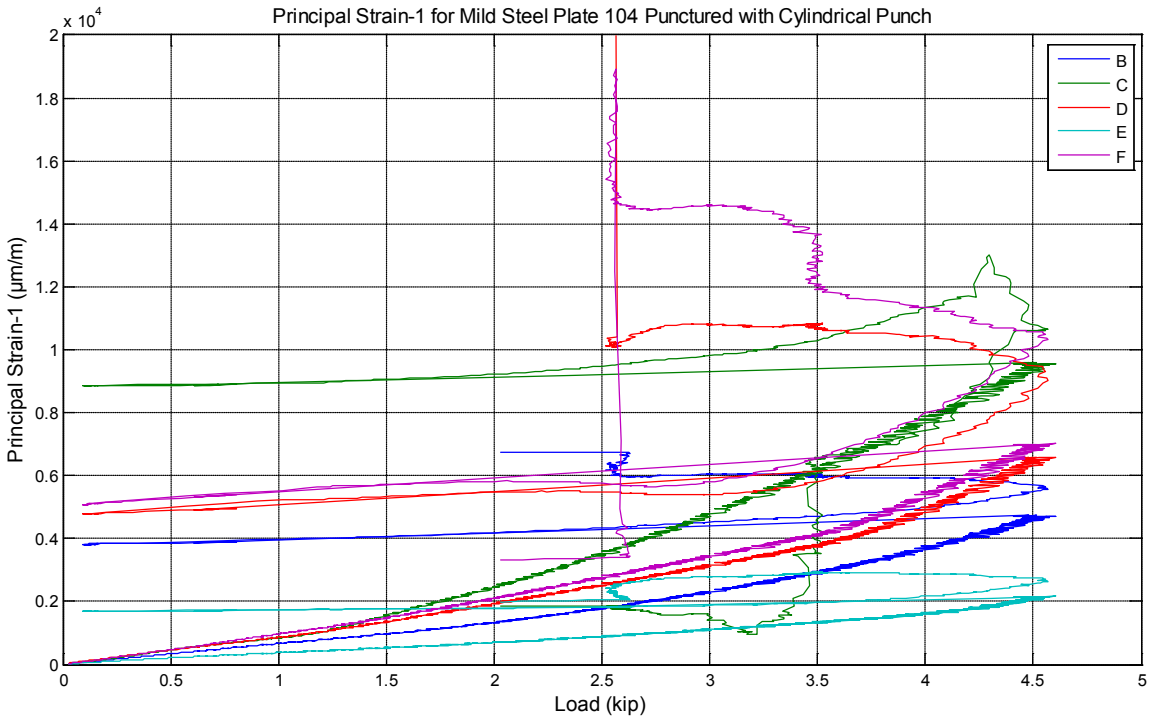

Figure 39. Principal Strain 1 for mild steel Plate 104 punched with a cylindrical punch

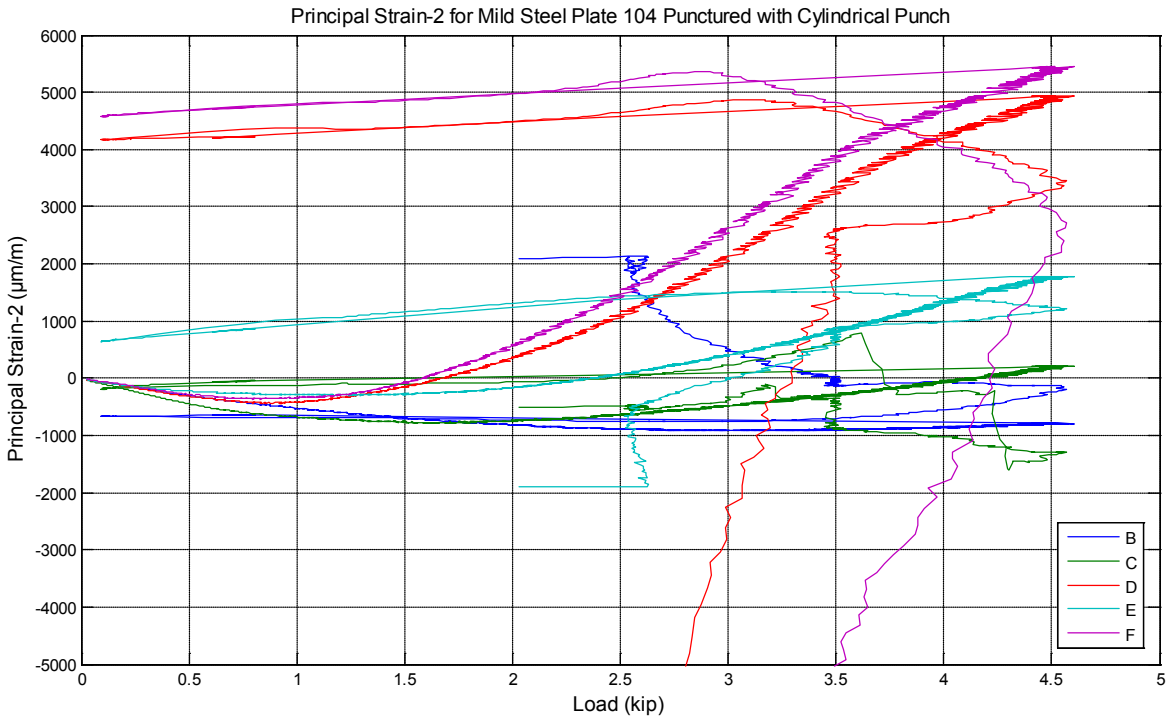

Figure 40. Principal Strain 2 for mild steel Plate 104 punched with a cylindrical punch

As shown in Figure 40, similar to the 0°, 45°, and 90° channels of each strain gage, principal-angle responses for Gages D and F follow the behavior of one another.

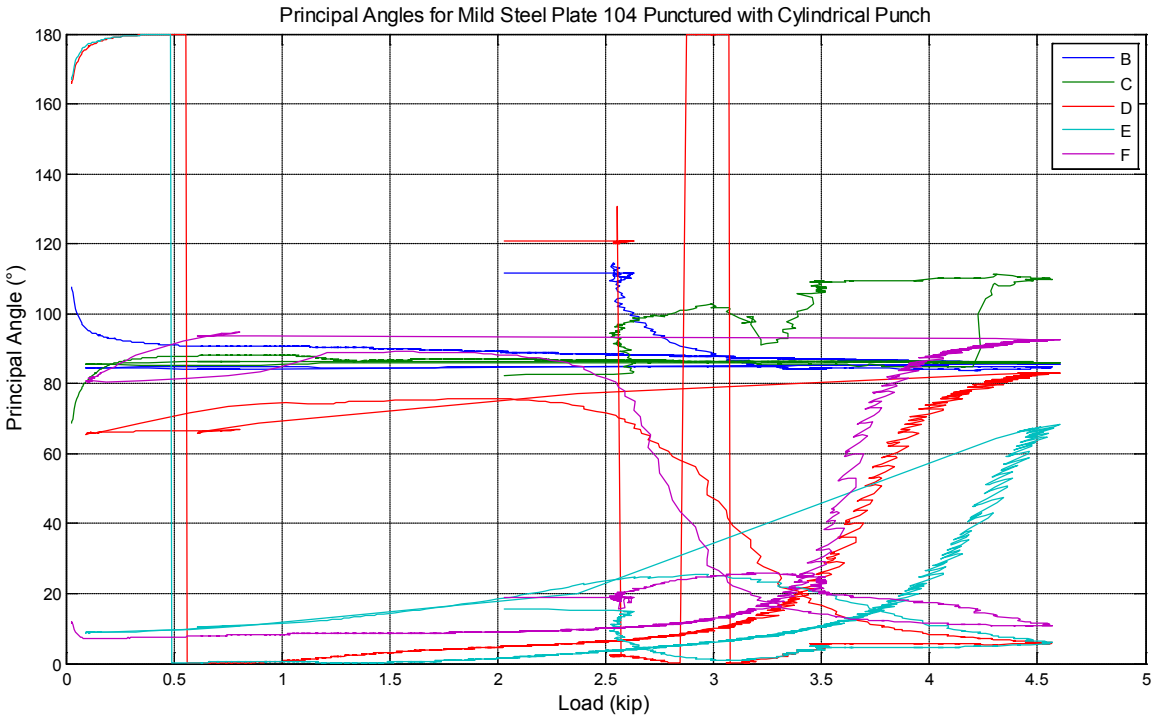

Figure 41. Strain angles for mild steel Plate 104 punched with a cylindrical punch

As shown in Figure 41, the principal angle for Gages D, E, and F, located on the DIC plate side approach 90° as the load increases. The strain channels on the DIC plate side were assigned to correspond with the strain directions on the punch side of the plate. Interpretation of the assigned channels reveals that the principal angle points of all strain gages radially point toward the center of the plate.

2.6 Strain Analysis for Abrasion-Resistant Steel Plate 102 Punched with a Conical Punch

Strain gage results for the abrasion-resistant plate punched with a conical punch are shown in Figure 42 through Figure 44.

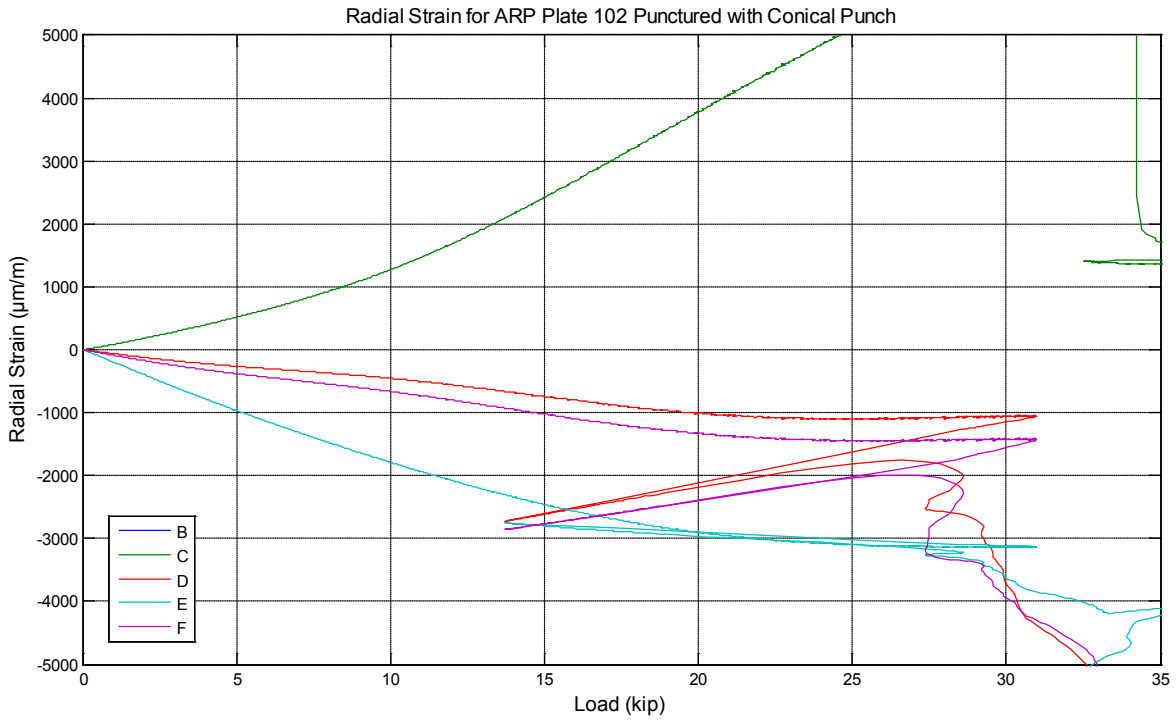

Figure 42. Radial strain for abrasion-resistant Plate 102 punched with a conical punch

As shown in Figure 42, Radial Strain C on the punch side of the plate is positive as the punch pressed through the plate and stretched the material along the radial direction. The radial strain reading for Gage B was a bad signal and is not shown in Figure 42. The DIC side of the plate was compressed radially, revealing negative strain.

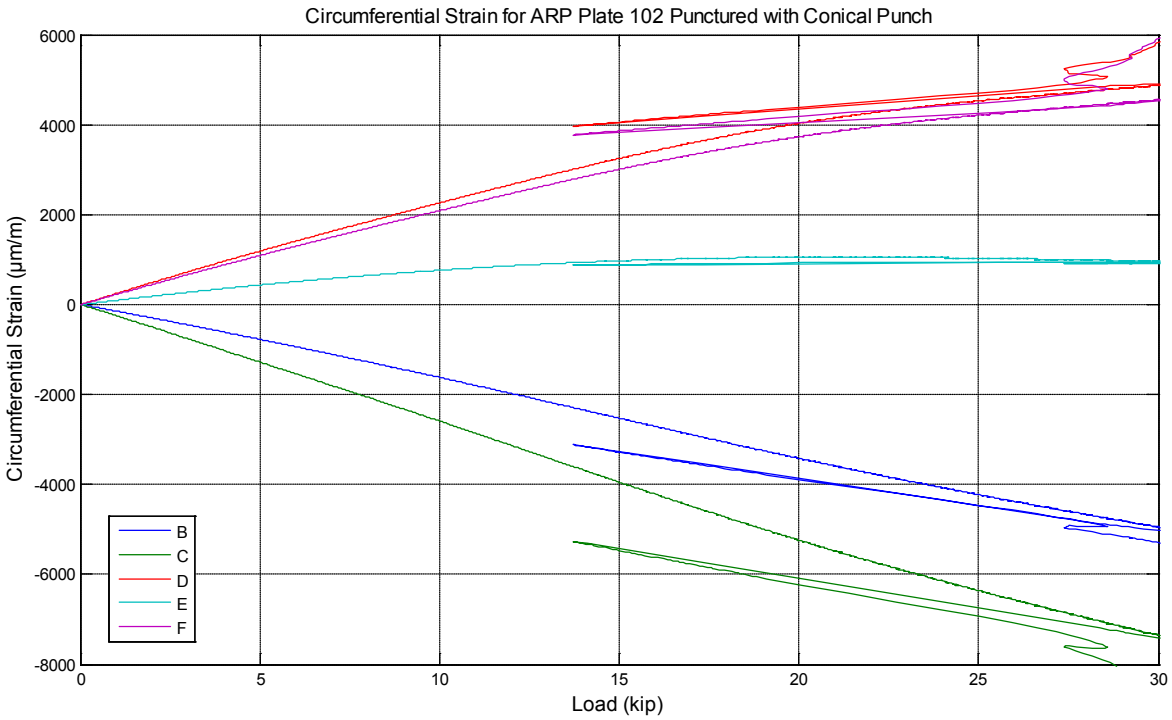

Figure 43. Circumferential strain for abrasion-resistant Plate 102 punched with a conical punch

As shown in Figure 43, the circumferential channel for Gage B was in working condition and followed the same response as Gage C located on the punch side of the plate. Grouping of signals as well as signal sign indicating compression of elongation appear to correlate to plate side. Circumferential readings for the DIC side of the plate are shown as positive strains.

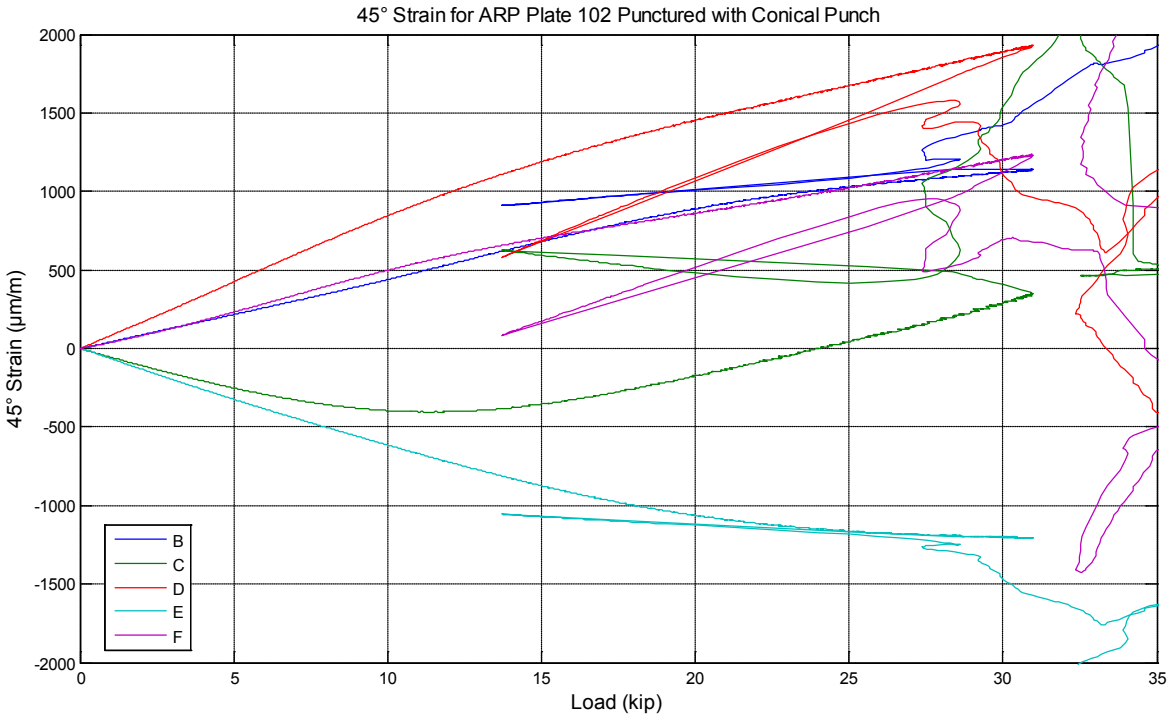

Figure 44. 45° strain for abrasion-resistant Plate 102 punched with a conical punch

In Figure 44, unlike similarities observed for other strain gages, a correlation to strain gage location and plate side was not apparent for the 45° strain readings. An interpretation of the strain readings and their direction is gained by examining at Figure 45 through Figure 47.

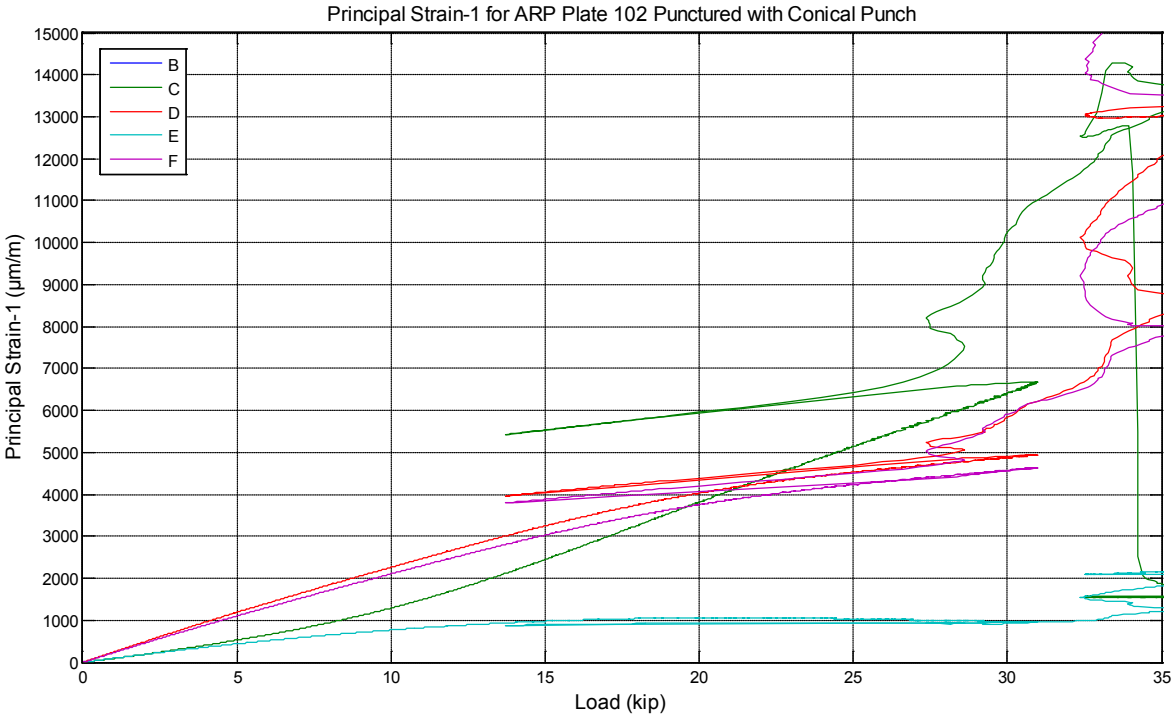

Figure 45. Principal strain 1 for abrasion-resistant Plate 102 punched with a conical punch

The radial reading for Gage B was incorrect, which produced erroneous principal strains and angles as shown in Figure 45. Those readings will be ignored for the following figures. It is noted that all principal-1 strains increase with increasing load. Strain Gage E, located furthest from the punch, naturally displays a lower principal strain reading.

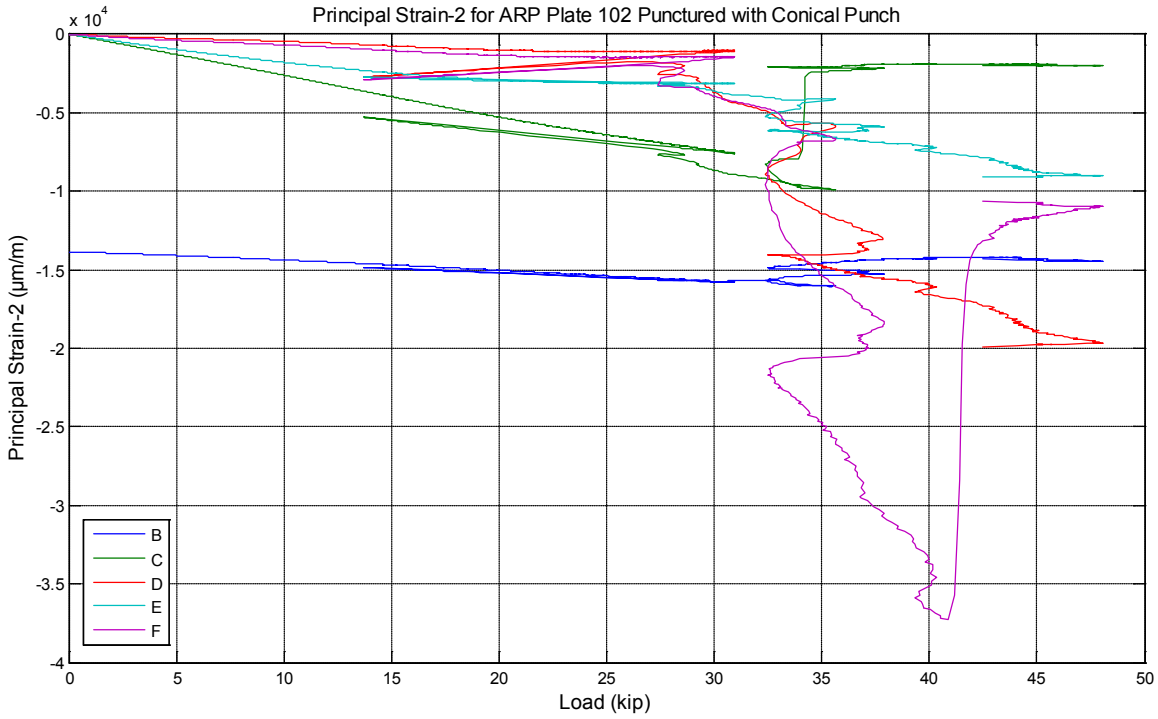

Figure 46. Principal strain 2 for abrasion-resistant Plate 102 punched with a conical punch

As shown in Figure 46, similar behavior is observed for principal-2 strains in that they become increasingly negative as load increases.

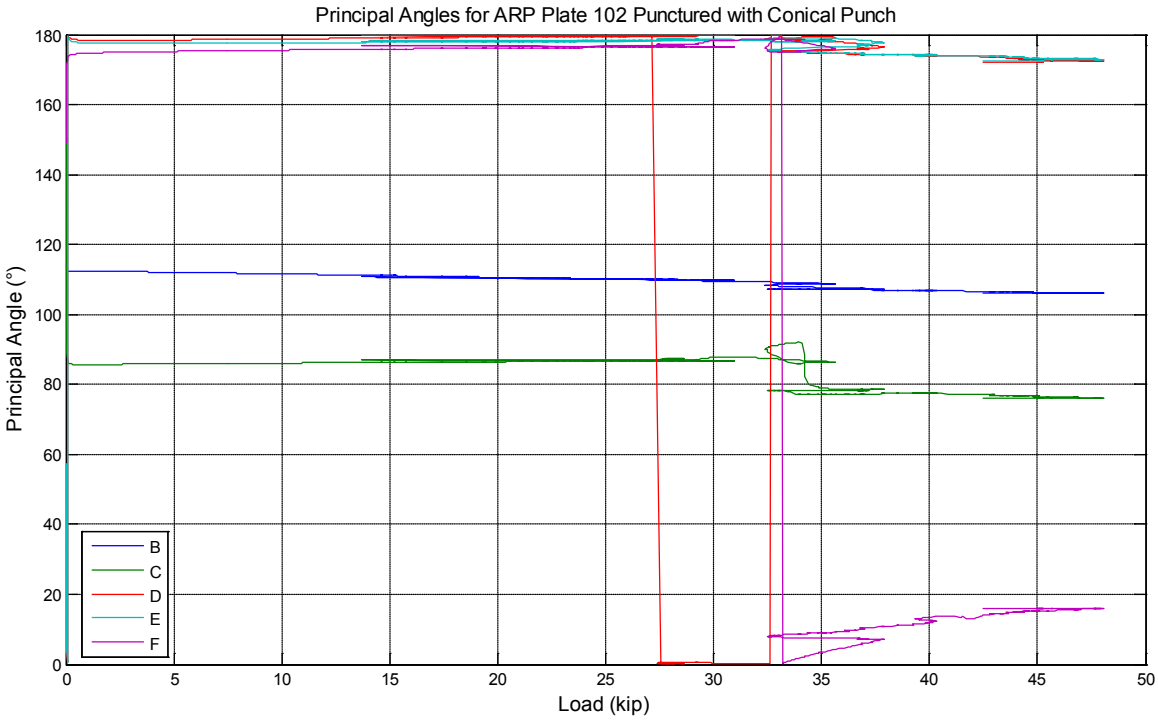

Figure 47. Principal angle for abrasion-resistant Plate 102 punched with a conical punch

As a a result of the orientation of all strain gages on the abrasion-resistant plate, interpretation of Figure 47 reveals that the working strain gages produce a principal angle that points radially toward the center of the plate.

For all plates tested, it was observed that strain gage readings and in-depth interpretation of that data provided insight to the behavior of the material at various locations. Once perforation occurred, however, there was more randomness and separation in the strain readings as the plate petaled or spiraled as was the case with the abrasion-resistant plate. Because these failure modes are dependent on defects in the material, the metal-forming process, and the application of the force, a full-field strain reading was required to provide additional information. Strain readings provided by strain gages offered information only on those areas where the strain gages were located. The complicated failure patterns produced required a more in depth study into the experimental results to confidently elaborate on the validity of the failure patterns obtained. DIC provided validation of the strain gage readings, and a full-field strain behavior of each plate and is presented in the next section.

2.7 Digital Image Correlation of Static Results

Digital image correlation (DIC) provides full-field and 3-D displacement information as its primary measurement. The default coordinate system is between the stereo cameras. This, however, is typically not useful, so a coordinate transformation can easily be done in the DIC software to place the coordinate system at nearly any location. For all of the data presented in this paper, the coordinate system is at the center of the plate, with a best-fit plane fit to the undeformed plate defining the *x*-*y* plane. The *x* axis is then located horizontally and the *y* axis vertically, with the *z* axis following the right-hand rule. This is shown in Figure 48.

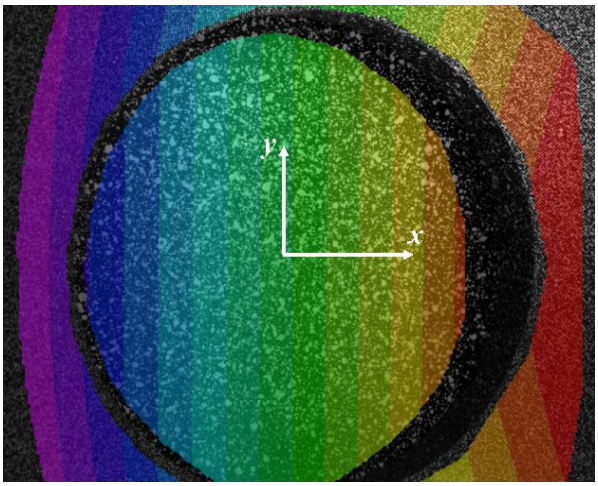

Figure 48. Coordinate system for DIC results

Once translated to the center coordinate system, different data can be extracted from the DIC results. This includes shape, displacement, and strain data. Examples of this are shown in Figure 49, with the original shape shown on the left and out-of-plane deformation shown on the right. The deformation can be displayed in two ways; either as a deformed shape or as a deformation only. For all of the data in this report, deformation only is displayed. This is denoted by the variable *W*. It is also important to note that the data either displayed or plotted in this document are Lagrangian strain, which for small strains is identical to engineering strain, but at large values, diverges.

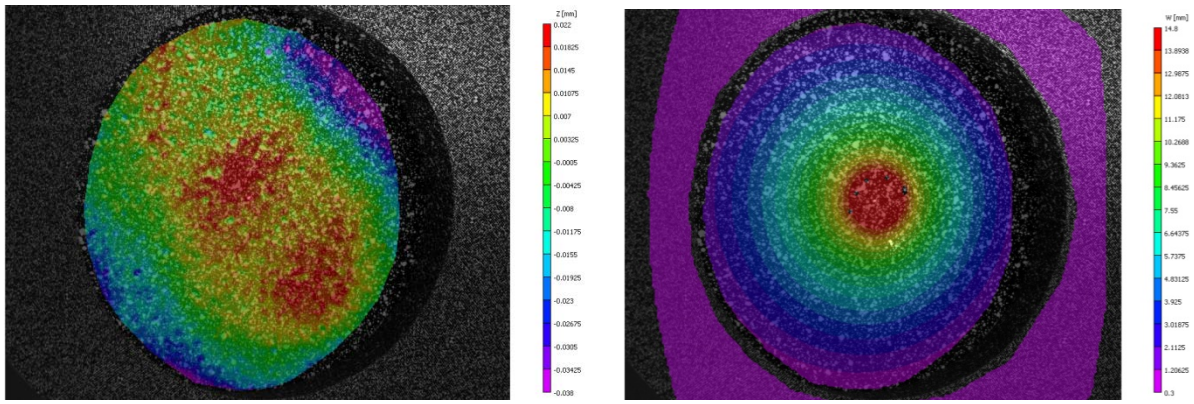

Figure 49. Example DIC results showing shape results and out-of-plane deformation results

2.8 Center Point Deflection

The primary measurement desired by the simulation community for model development was the center-point deflection versus load. With this in mind, on some measurements four different techniques (i.e., DIC, LVDT, Keyence sensor, and actuator) were used to measure this quantity. An example of this is shown in Figure 50.

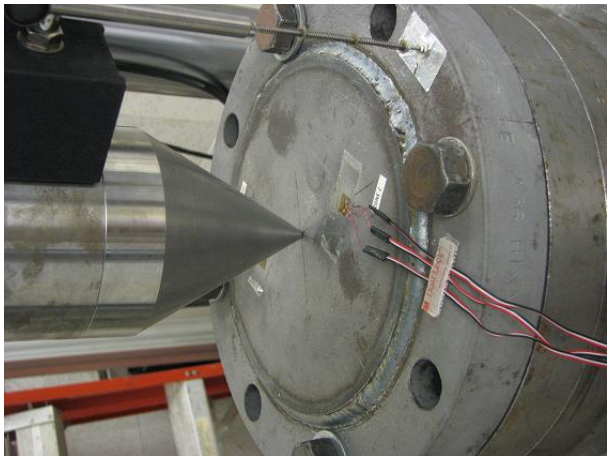

Figure 50. Punch-to-Plate displacement lvdt

As can be seen, there is good agreement between the three measurement techniques, with the actuator being the least reliable of the four. The actuator sensor was employed only for setup positioning.

The DIC results, *W*, show better agreement with the LVDT results when the rigid body motion of the frame is removed. This was done by extracting points around the outside frame area, averaging the results, and subtracting them from the extracted center-point data. The Keyence detector agreed better with this result than with the uncorrected result because the Keyence

measurement included the frame deformation and was mounted and referenced on the same structure as the DIC cameras. Subsequent petaling punch series replaced a Keyence sensor with an LVDT to provide the full perforation-petaling displacement. This is not true of the LVDT measurement because it was mounted in such a way as to remove the rigid body frame motion.

A further complication in analyzing the data when comparing to the LVDT is that the LVDT measured the displacement to the outer punch diameter rather than to the center point of the plate. Figure 51 shows a correction for the bow of the plate around the punch during the test. This bow can be seen in the cross-sectional view from a 12-inch sample using a 1-inch punch as shown in Figure 52.

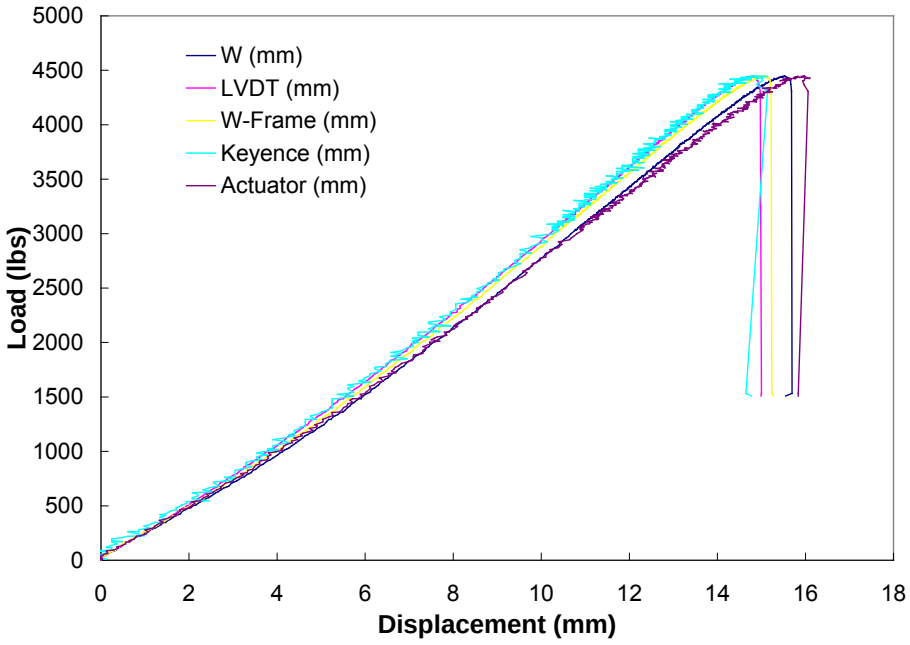

Figure 51. 6-inch plate, 1-inch punch, Sample 6, showing DIC, LVDT, Keyence, and actuator results

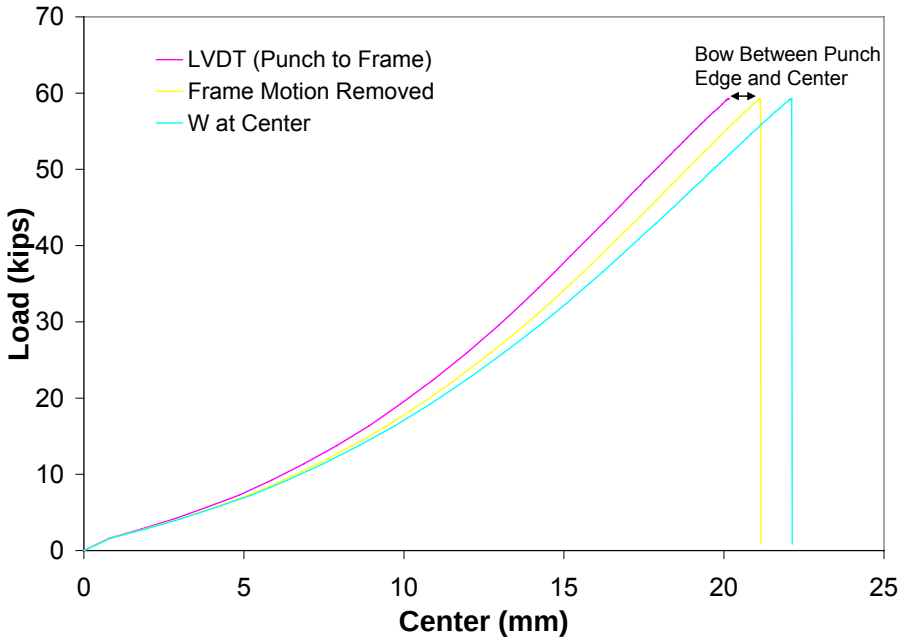

Figure 52. Data showing the difference between the center-point measurement and the LVDT from plate bowing around the punch

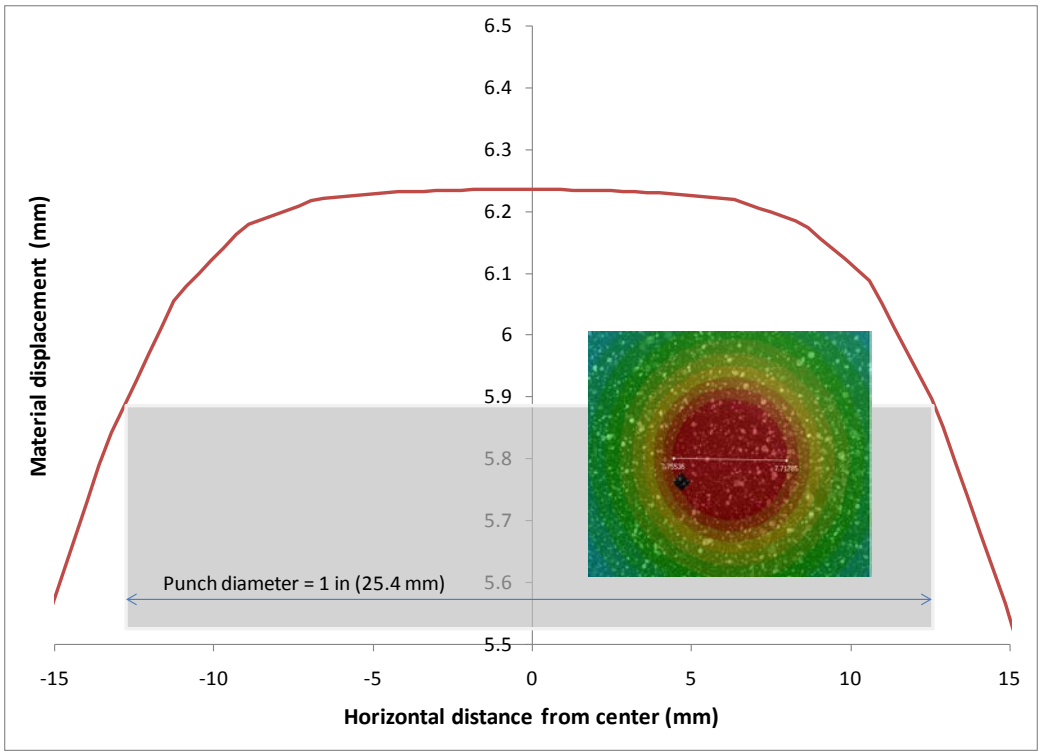

Figure 53. 12-inch sample, 1-inch punch, Sample 2, showing bow around punch tip at around 8 millimeters (mm) of displacement. (The error in Figure 52 is approximately 0.4 mm.)

The center displacement results were extracted for all of the tests, with an image of a typical extraction location illustrated in Figure 54, in which the Keyence laser spot can be seen. While the system correlated over the spot, it did cause an anomalous bump in the data. We abandoned using the Keyence sensor after a few tests had confirmed that the DIC results were at least as good, if not better than, this single-point measurement. These are uncorrected results; that is, the small but measurable rigid-body motion has not been removed from the data. Good repeatability in the data is seen. Results for the 6-inch samples are shown in Figure 55, and results for the 12-inch samples are shown in Figure 56.

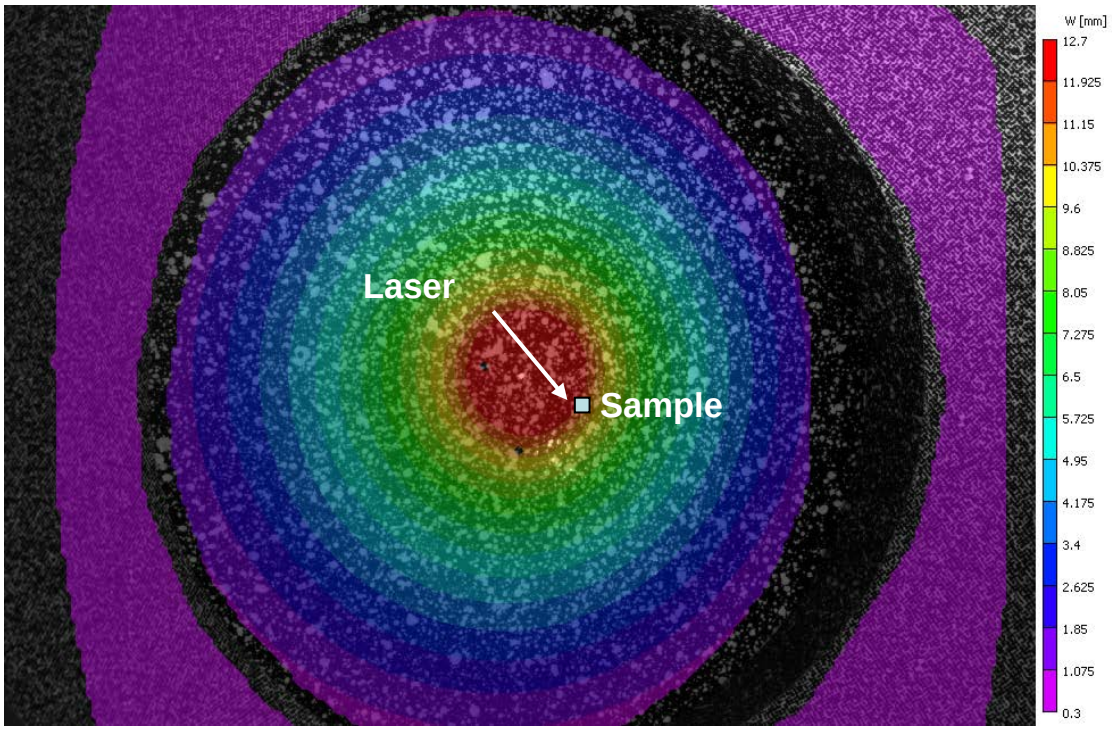

Figure 54. Image of typical extraction location (from 6-inch Sample 6)

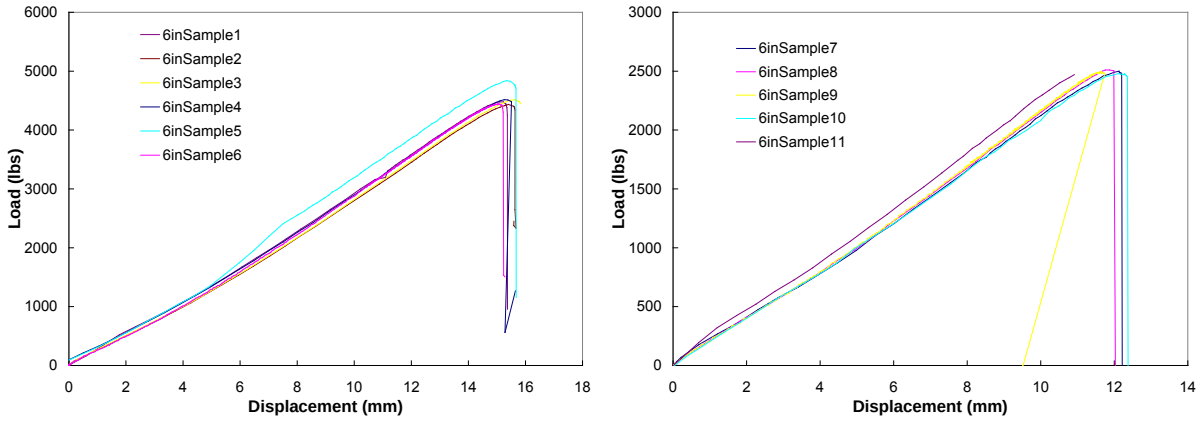

Figure 55. Center displacement results (*W*) for all of the 6-inch tests (1-inch punch tests are shown on the left, 0.5-inch results are shown on the right.)

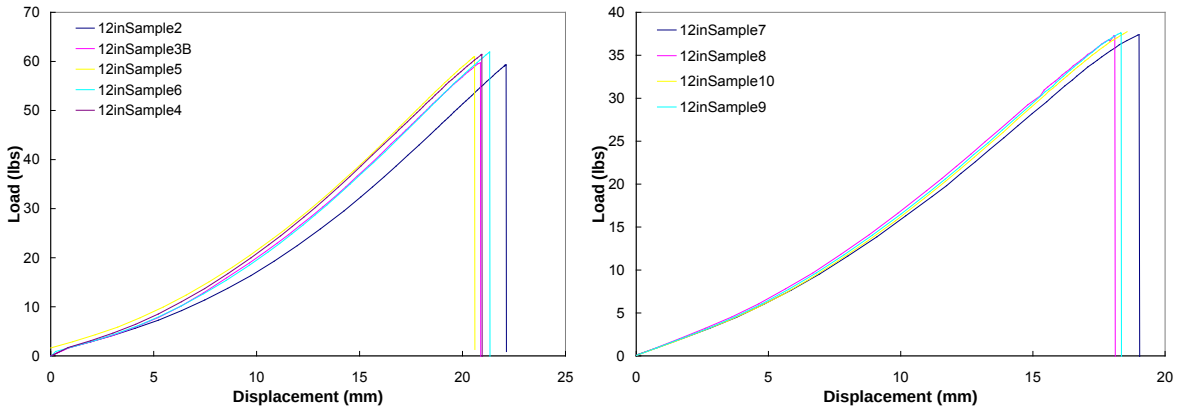

Figure 56. Center displacement results (*W*) for all of the 12-inch tests (1-inch punch tests are shown on the left, 0.5-inch results are shown on the right.)

2.9 Maximum Strain Location

In a similar manner, the principal strain location was extracted for all of the test cases. The location was chosen in a load step where the maximum strain location could easily be found. A typical extraction point is shown in Figure 57. A second consideration was taken into account where possible, which was to find a location where the data existed for as many load steps as possible. The punch edge location often exhibited a loss of data because of correlation problems. As the problem was axisymmetric, any location around the punch edge was equal (to a first approximation). On some tests, a higher strain region was seen, which corresponded to an earlier failure at that location. The cause of this lack of symmetry is unknown, but it was most likely caused by slight misalignments of the punch with the specimen. The plots for the 6-inch samples

are shown in Figure 58 and for the 12-inch samples in Figure 59. Jumpiness or noise in the data is caused by a loss of correlation at that point.

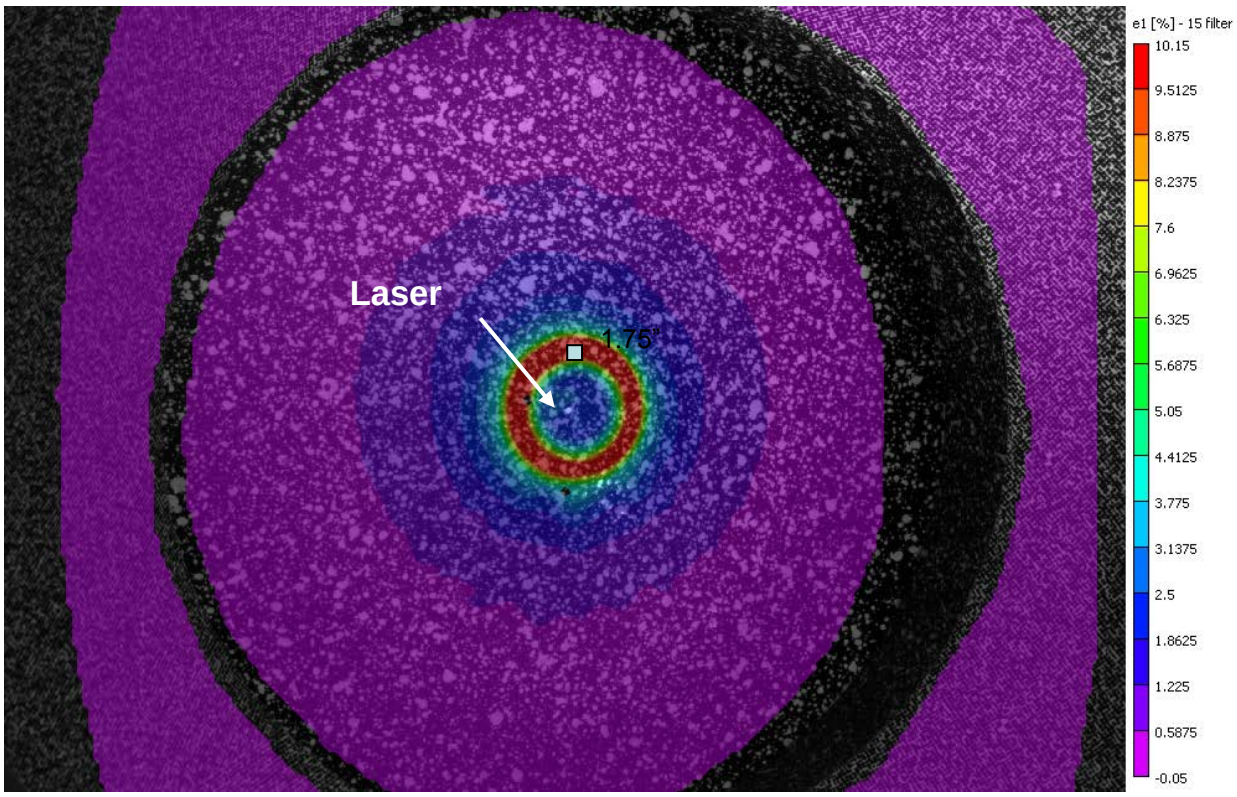

Figure 57. Sample location of extraction of principal strain (from 6-inch Sample 6)

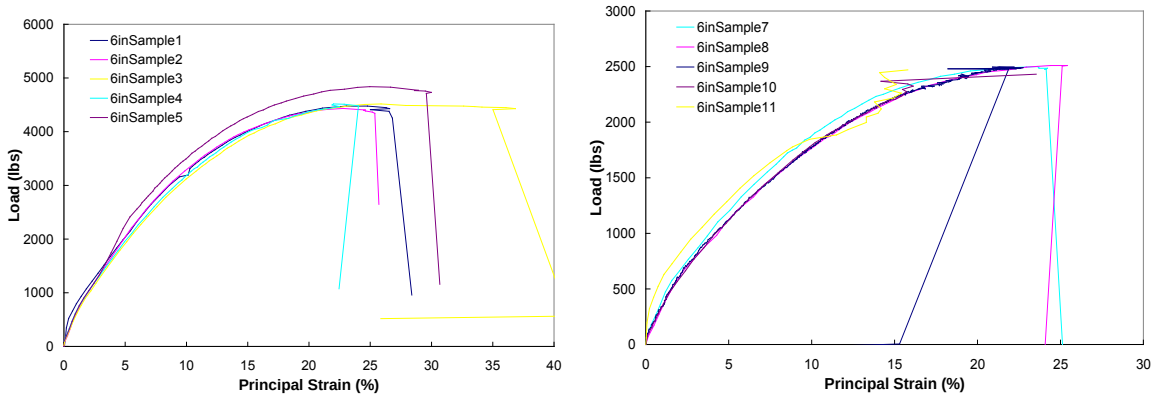

Figure 58. Principal strain at maximum location for the 6-inch samples

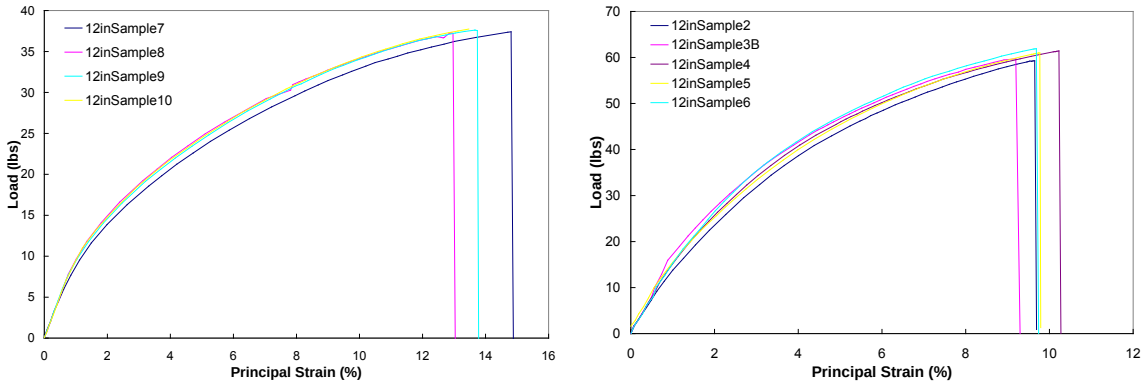

Figure 59. Maximum principal strain for the 12-inch samples

2.10 Strain Gage Comparison for Static Tests

2.10.1 Preliminary Comparison

The data were analyzed using image correlation software that calculated the displacements and the Lagrangian strain over the entire surface. Data at three strain gage locations were then extracted from the strain gage locations illustrated in Figure 20; two of the locations, A and C, both at identical distance from the center, are shown in Figure 60. As can be seen, the repeatability between the three mild steel-conical punch tests was excellent. As mentioned previously, strain gages were also applied to the opposite side of the plate from the DIC work. Finite element modeling has confirmed that the thickness and diameter of the plates violated our original membrane assumptions making comparison of the DIC results and the strain gages qualitative at best. Results from these tests are not shown.

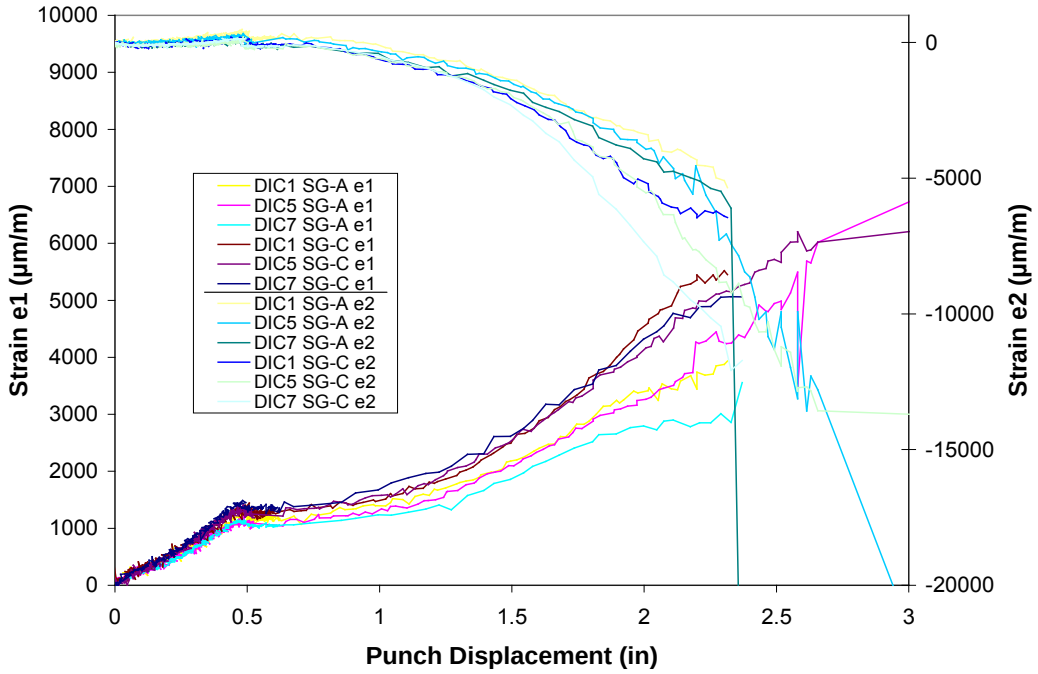

Figure 60. Quasi-static testing of mild steel plates punched with a conical punch: plot showing principal strains versus punch displacement at two gage locations, both at the same radius from the center

2.10.2 Front-Side Strain Gage Comparison

After determining that the plate thickness violated the membrane assumption, strain gages were applied to the front surface at two different radii as illustrated in Figure 21. On the DIC surface, after the gages were applied, they were painted over and speckled along with the rest of the metal surface. This allowed the strain to be extracted at the same location as the strain gage. There were some issues associated with data loss in this area caused by the wires from the strain gages.

Mild steel plates were tested with both the conical and cylindrical punch. One abrasion-resistant plate was also tested using a conical punch. For the analysis, only Gages at D and F are presented. (The results are similar for Gage E although of much lower strain values due to being further from the center of the plate.)

Figure 61 shows the strain results at locations D and F for both the strain gages and the DIC results. As can be seen the comparison is excellent. The deviation at later punch displacements between Gage D and Gage F is caused by the petaling behavior, with one of the tears being located closer to Gage F as seen on the Figure 59 inset from the DIC results. The results also indicate the higher loading of the cylindrical punch and the sudden relaxation when the punch penetrates observed in earlier studies.

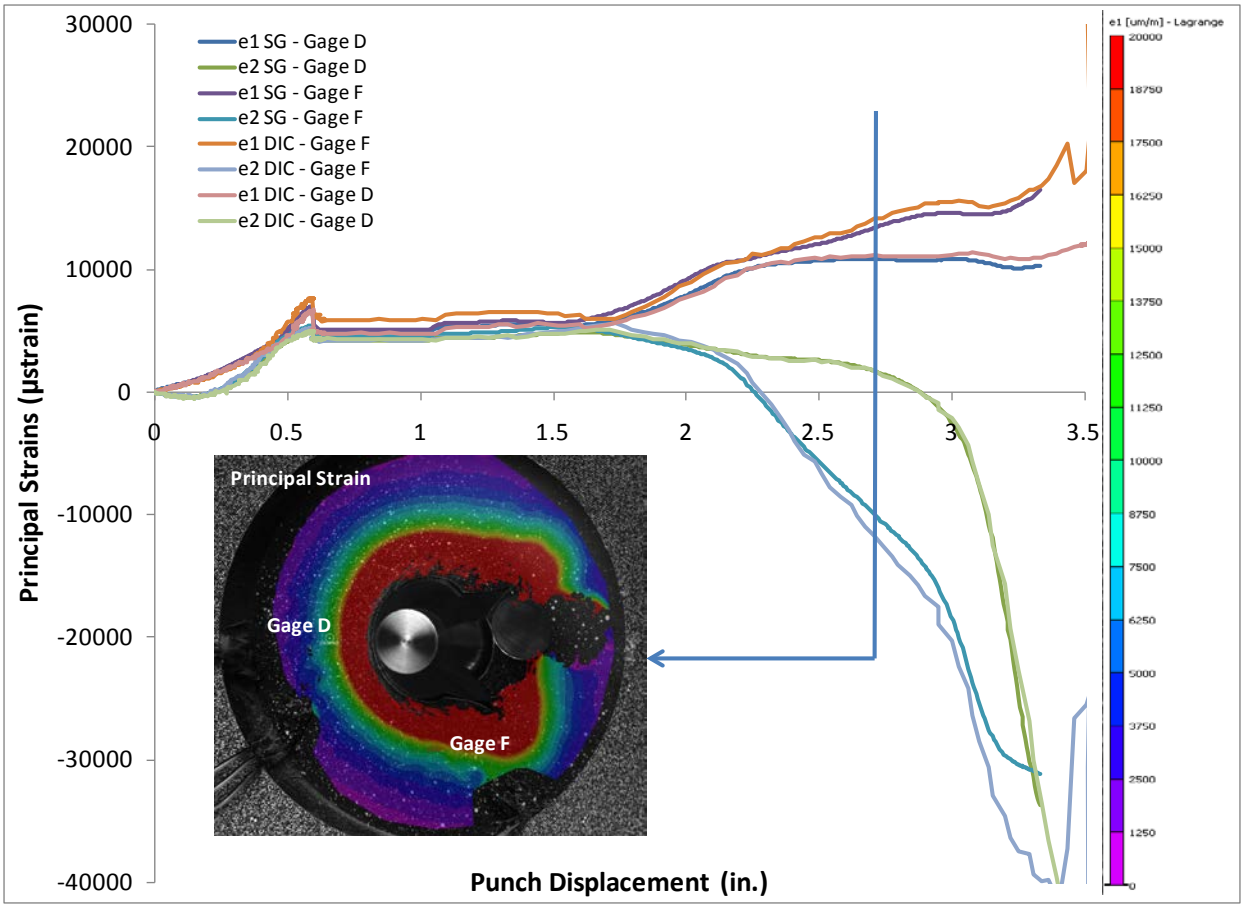

Figure 61. Test 14: mild steel plate punched with a cylindrical punch

Further analysis was conducted on these later tests to check the axisymmetric nature. This was done by extracting the strain results around a circle at the radii of Gage D and Gage F (both at 44.45 mm). This is graphically shown in the inset to Figure 62 by the green dots in a circle plotted on the initial shape. These results were then exported and a mean and standard deviation for each load step were then found. These are plotted in Figure 61 as *Radius Mean*, with the error bars reporting the plus/minus standard deviation of the strain for the points around the circle. Early on in the loading, the error bars are small, which indicates that the loading of the plate is reasonably axisymmetric. After failure, the error bars get larger. This does not indicate that the data are getting noisier, only that the plate is failing, and the strain is no longer a uniform value at the extracted radius. This should be expected because the strain around the tearing locations of the petaling is much higher than on other points of the radius.

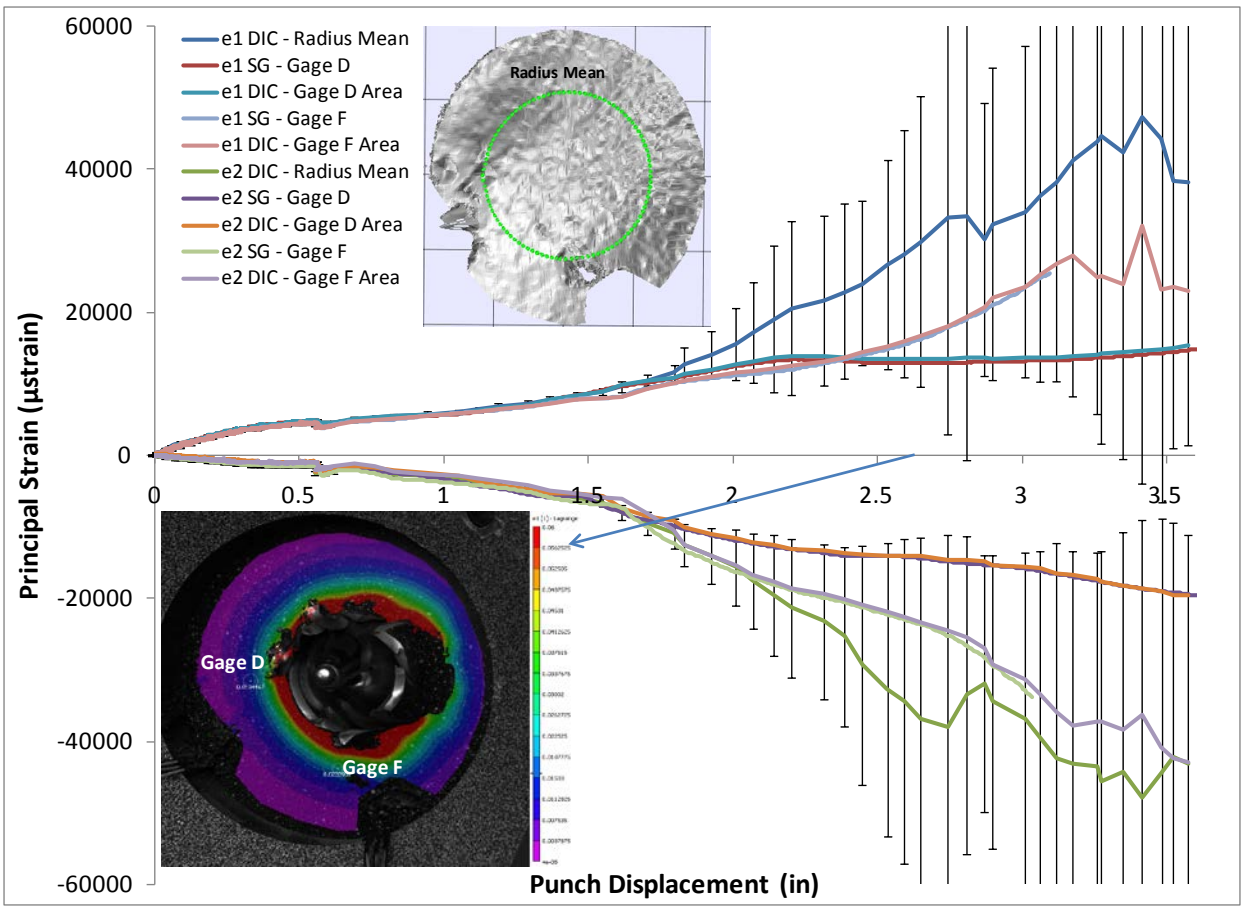

Figure 62. Test 12: abrasion-resistant plate punched with a cylindrical punch

The results for the other four tests, Tests 9–11 and 13 are similar and are reported in Figure 63 through Figure 65.

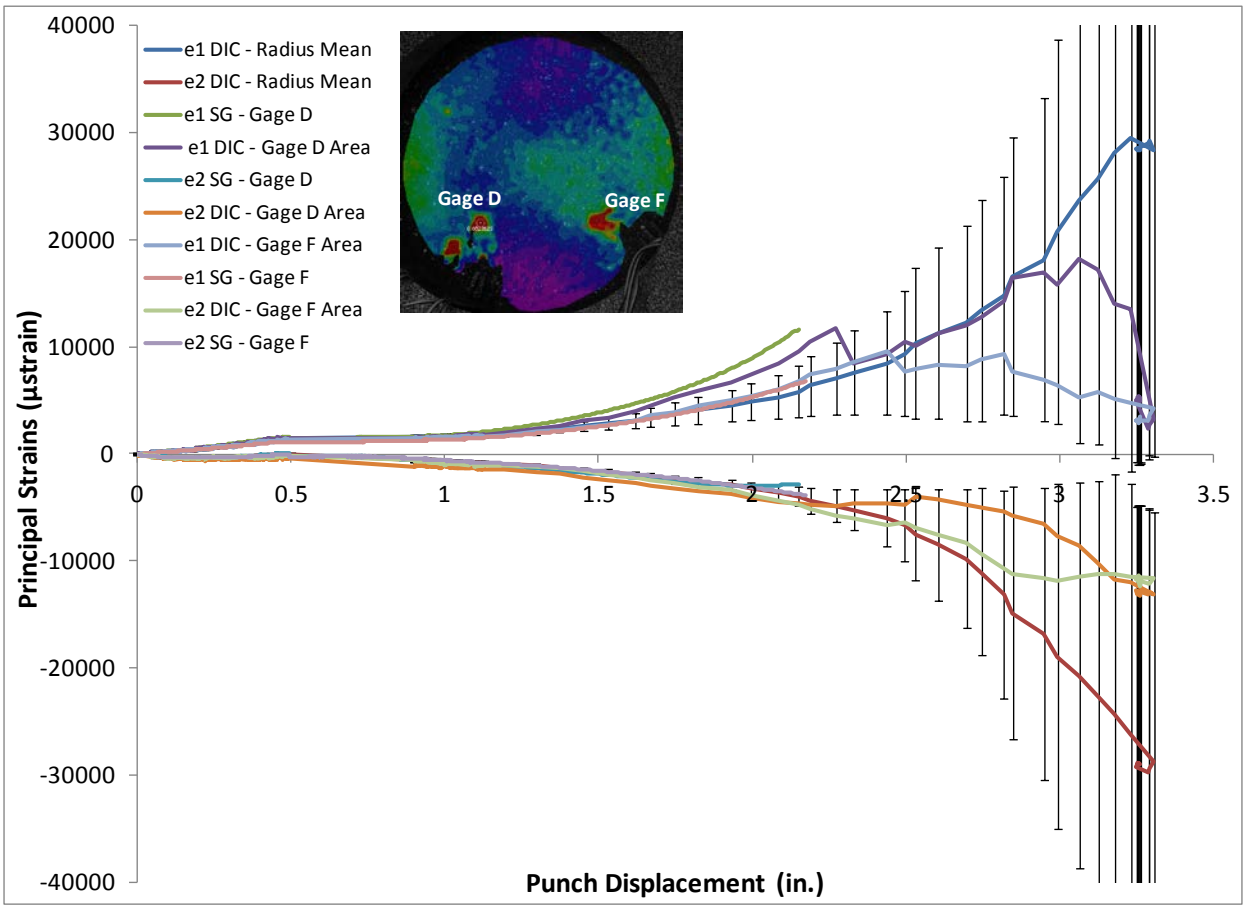

Figure 63. Test 9: mild steel plate punched with a conical punch

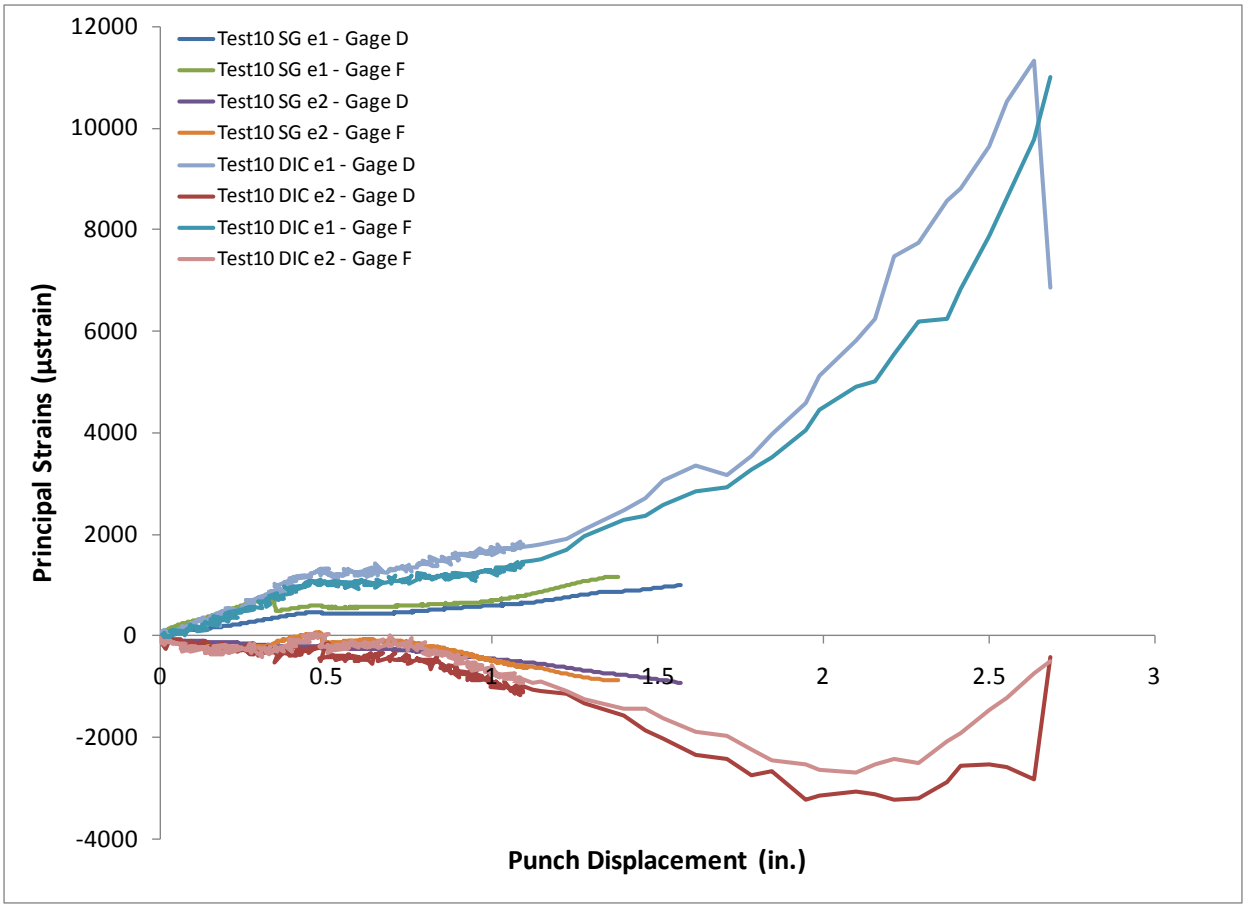

Figure 64. Test 10: mild steel plate punched with a conical punch

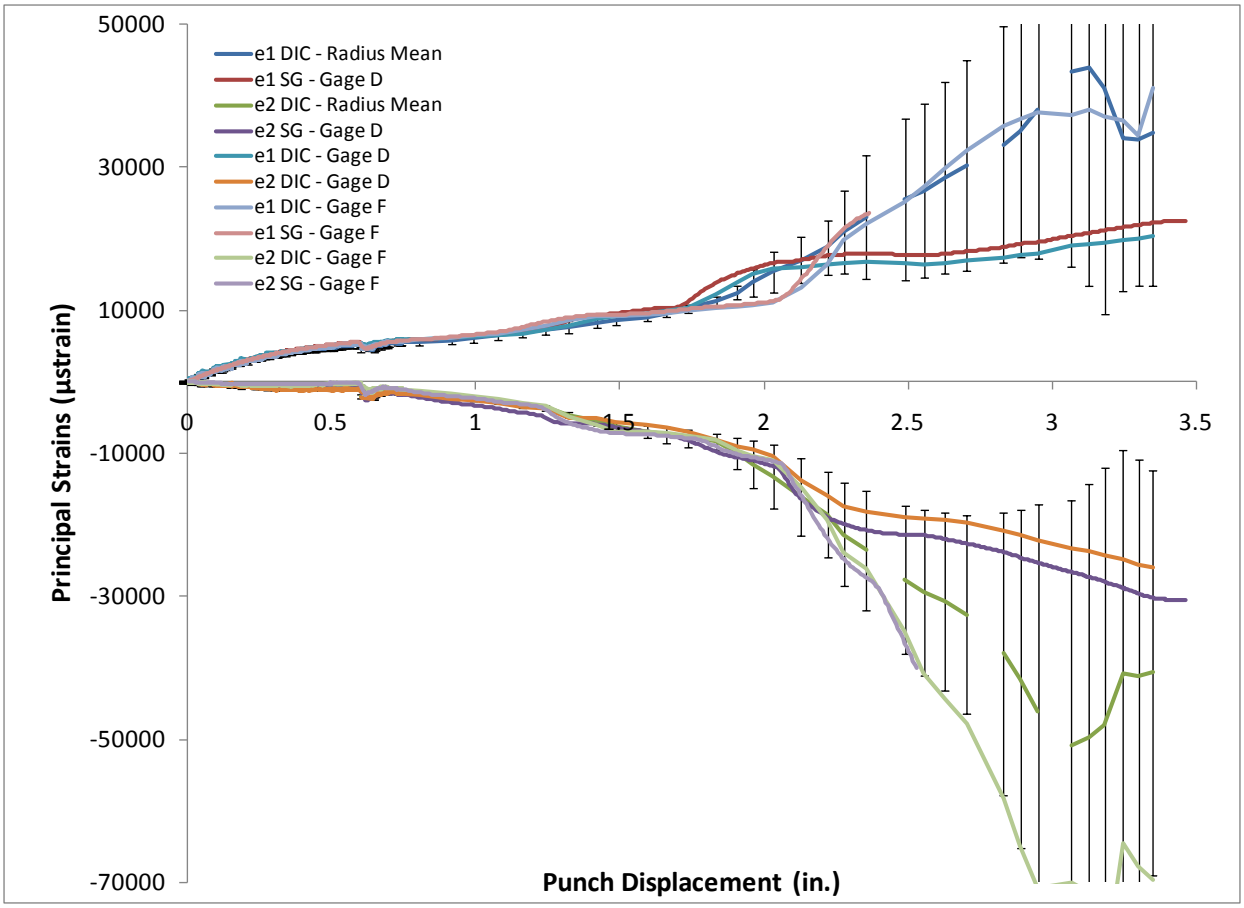

Figure 65. Test 11: abrasion-resistant plate punched with a conical punch

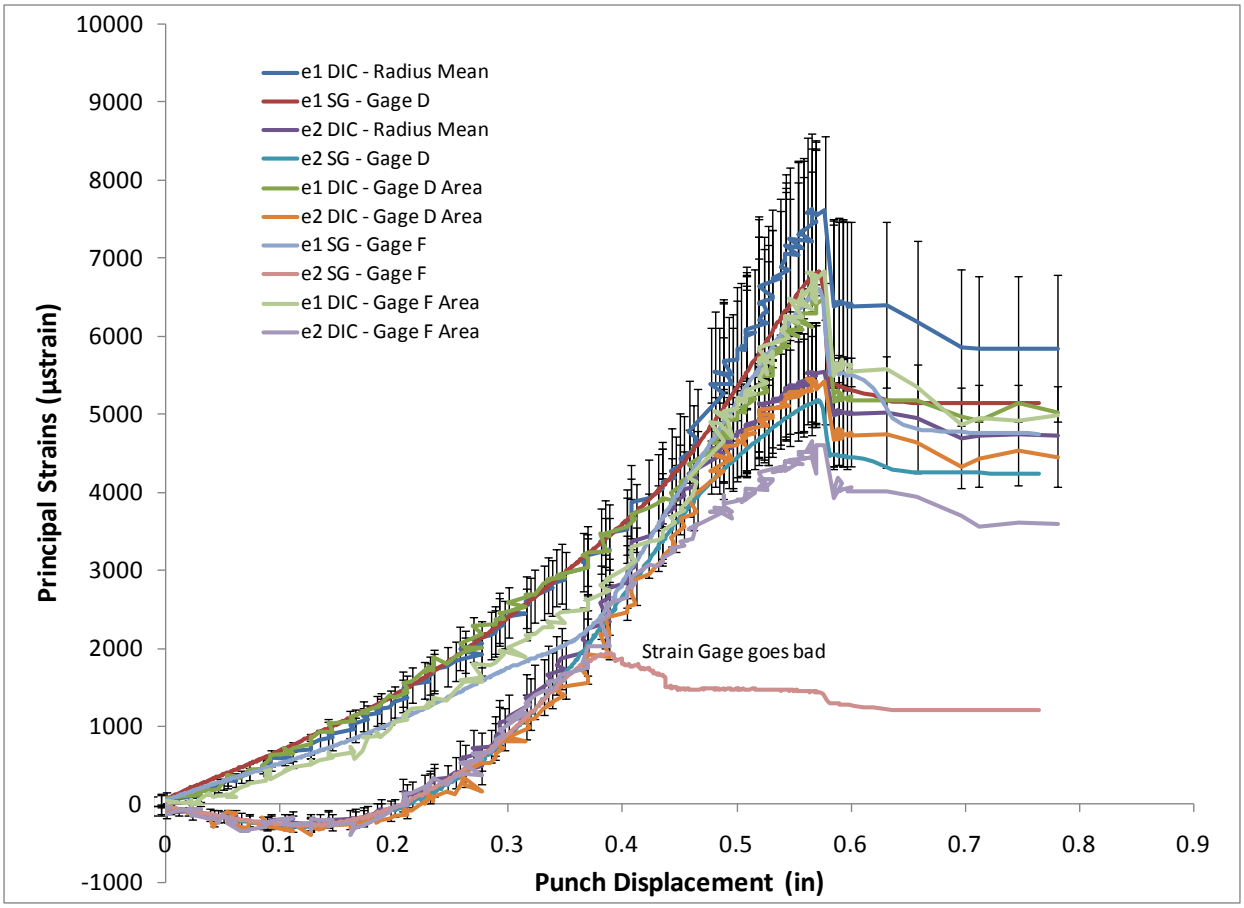

Figure 66. Test 13: mild steel plate punched with a cylindrical punch

3 DYNAMIC TESTING

3.1 Dynamic Punch-Plate Test Setup

3.1.1 Mechanical

An elastic cord, drop table shock test machine was adapted for use in material testing. The machine used is referred to as DT-67 and is located in Building 860, Room 132A. The setup immediately following a test is shown in Figure 67. A four-sided box fixture was fabricated to allow visual access to the bottom surface of the plate. This fixture was attached to the reaction mass via four 3/16-inch screws in the top of the reaction mass and four 3/4-inch threaded rods to 1-inch-thick by 2-inch-wide steel bars running underneath the reaction mass.

This reaction mass is a solid piece of steel weighing 3,000 pounds supported on air-oil shock absorbers. The pipe flange specimen is bolted to the top of the fixture. A load-spreading ring with clearance for the bolt heads is placed on top of the flange. Annular felt rings are stacked on top to engage the circular plate bolted to the bottom of the carriage. (Typically, 3 inches of height were provided by the felt rings.) This is needed to safely absorb the excess kinetic energy of the carriage after the punch penetrates. The load cells are located between this stop plate and a threaded steel block where the punch mounts. This means the load cells will go into tension when the felt stop engages.

3.1.2 Digital Image Correlation Setup for Dynamic Tests

Imaging for correlation purposes was performed with two Phantom® model v7.3 high-speed digital cameras made by Vision Research that captured images at 416 × 400 pixels. Illumination was provided by three high-intensity 1,000-watt quartz lights (see Figure 68). Because of the geometry of the test machine, direct line-of-sight imaging was not possible, so a technique using a first-surface mirror was devised. It is not apparent in the pictures, but the mirror is supported independently from the fixture mounted on the reaction mass. The fixture had two open sides to allow visual access and a means for the mirror support structure to pass through. This was done to minimize image distortions caused by camera shake or mirror vibration during the test. This mounting arrangement delayed the onset of these effects until after the time of interest. A reduced camera resolution of 416 × 400 was used to increase the frame rate to 17,021.3 pictures per second (pps). This frame rate yielded an adequate temporal response while maintaining good spatial resolution.

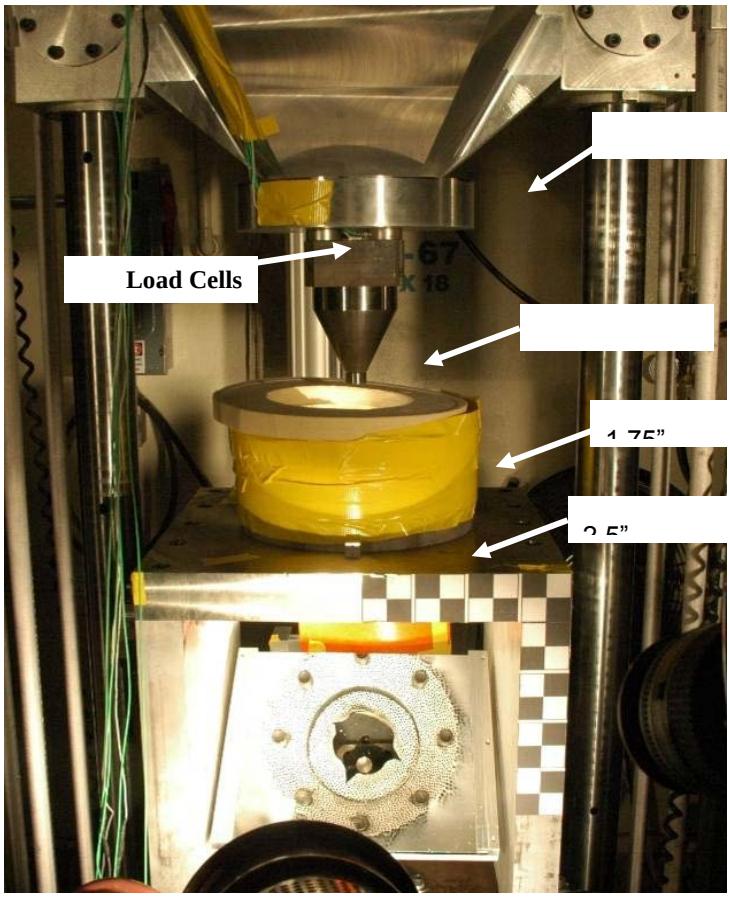

Figure 67. Dynamic punch test setup

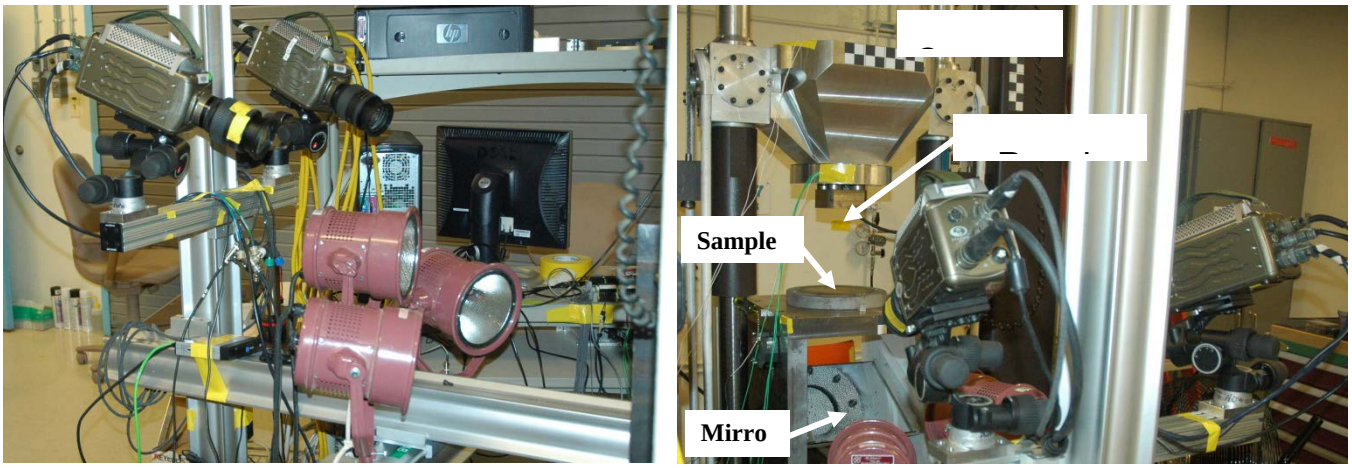

Figure 68. Phantom® cameras setup for high-speed image acquisition and related illumination hardware

Exposure time was 13 microseconds (µs), and the framing interval was 58.75 µs (17,021.3 pps). The cameras were sent an Inter Range Instrumentation Group (IRIG) time code generated by a Symmetricom® IRIG receiver allowed to freewheel without an antenna. The cameras were synchronized using the fsync signal generated by one camera designated the master. A 9-µs frame delay was added as an empirical correction to ensure that the cameras were taking frames within 2 µs of each other.

The cameras viewed the bottom side of the plate through a first-surface mirror. Calibration of the stereo rig was performed while imaging through the mirror. The inside of the fixture was painted white to maximize diffuse reflected light. The cameras and lights were supported on an X-brace structure that straddled the reaction mass. A fan was also employed to minimize heating of the parts and fixture and the scintillation distortions in the video.

Additionally, a third camera was used to capture the overall rigid-body motion of the test. A Phantom® model v9 camera was used running with a frame interval of 33.25 µs (3,000.75 pps), 200 µs exposure, and 624 × 864-pixel resolution. The camera was located as far away as practical in the room. It was 72 inches above the floor and 176.5 inches from the front of the plate fixture. Quad markers were placed on the carriage, fixture, and vertical column for automated point tracking using Trackeye software. Additional illumination was provided by two 1,000-watt quartz lights set back on tripods.

The cameras were triggered by an output from the Spectral Dynamics Corporation VXI Data Acquisition System (VIDAS). The trigger lines of all Phantom® cameras were connected in parallel to the mini-DIN trigger output on the VXI 2824 digitizer board. This output generates a low-to-high TTL step change when the data system triggers. The data system is set to trigger on an acceleration level from an accelerometer mounted on the drop table carriage. Occasionally, a sufficient acceleration level was not reached until the carriage impacted the felt stop ring. This is not a problem because both the data system and cameras have circular buffers and can easily be configured with enough pretrigger time to capture the event. This setup provides one level of time synchronization between the cameras and data system by aligning Frame 0 of the *cine* files

with the trigger time. A second level of time synchronization is provided by comparing IRIG times recorded by the cameras with the IRIG time recorded on the data system via a BC637 PCI IRIG capture card. A significant wrinkle in this approach was uncovered and a workaround developed in preliminary testing. The Phantom® cameras can accept either a voltage input or a switch closure as a trigger. However, there is only one trigger line and no setting to force the camera to look for one or the other. The small voltage supplied by the Phantom® camera trigger line on three cameras wired in parallel was enough to raise the low value of the trigger circuit above the threshold value of the BC637 card. This caused the data system to miss the IRIG time of several events in preliminary testing. Other testing with a single camera did not show this problem but using three cameras did. The workaround developed used a 2:1 voltage divider with 1,000-ohm resistors that had the low legs tied to ground and the divided voltage sent to the input of the BC637 card. This reduced the TTL logic LOW level below the threshold, but the divided voltage after trigger was still high enough to produce a trigger.

3.1.3 Dynamic Test Instrumentation

In the dynamic punch tests, all transducer data were recorded on the Spectral Dynamics Corporation VIDAS. This is a semiportable system using the VXI bus standard controlled by a personal computer (PC). This system utilizes a sigma-delta analog-to-digital converter and provides 1-megahertz (MHz) bandwidth when sampling at 2.5-million samples per second. A Symmetricom® BC637 PCI IRIG card was used to record the IRIG time of system trigger for synchronization with the DIC cameras.

Both a 7270-20K accelerometer and a 7270-6K accelerometer were mounted on the carriage. During preliminary testing, accelerations as high as 1,500 G were recorded when the carriage hit the stop. Lower-range–higher-sensitivity accelerometers provide more accurate velocity change integration but have lower resonant frequencies and are more susceptible to ringing. Allowing the taper of the punch to engage the plate should absorb additional energy and reduce the acceleration caused by hitting the stop.

Force is measured using Kistler 9051A load washers. These load washers are piezoelectric and are used in conjunction with a Kistler 5011B charge amplifier. The output of each load cell was recorded separately to check for uniformity of loading. Summation of the outputs to a single channel can be pursued if the individual outputs are uniform. A fixture using four load washers in parallel between the punch and the carriage stop plate was fabricated. The load cells need to be preloaded to 40 kilonewtons (kN) when the fixture is assembled. Then the range of each load cell will be −40 to +80 kN, and the range of the assembly will be −160 to +320 kN (−9,000 to 72,000 lb_f).

Pretest analysis indicated the dynamic forces required to puncture the abrasion-resistant plate with a 1-inch-diameter cylindrical punch would be less than 35,000 lb_f. The amount of preload can be reduced some to achieve a greater compressive range, but the preload needs to be sufficient to keep the load washers under compression when the carriage hits the stop. Also, a 7270-20K accelerometer will be mounted on the back side of the punch adapter to allow for acceleration compensation of the load-cell reading for the mass of the punch and adapter plate (18.25 lb). A lower-range–higher-sensitivity accelerometer would give more accurate

compensation data (only ~100 G accelerations were observed during the penetration event). However, this location will have the most high-frequency acceleration content, and lower-range gages would be too susceptible to ringing.

A subset of samples will have strain gages applied for comparison to the DIC data. Two strain gage rosettes (Micro-Measurements C2A-06-125WW-350) were placed at 1.75 inches from the center of the plate, 90° apart. In the dynamic tests, the strain gages have the advantage of providing the most direct, highest bandwidth measurement of the plate response. Displacement measurement will be sample-rate limited, and the force measurement may be convolved with structural response of the carriage.

Carriage displacement will be measured with a Keyence LK-G407 laser displacement sensor. This sensor can output at 25 kilohertz (kHz) full range (7.9 inches) with 0.05% full-scale output (FSO) linearity (0.004-inch). It will be mounted to the fixture measuring a spot near the side of the carriage. This will account for the rigid body motion of the reaction mass. Fixture deflection will be measured with a Keyence LK-G157. This sensor can output at 25 kHz full range (3.1 inches) with 0.05% FSO linearity (0.0016-inch). This sensor will be mounted using a bracket attached to the reaction mass and will measure on the bottom side along the centerline of the flange fixture plate at a radius near the outside diameter (OD) of the flange (~11 inches in diameter). A lower-range–higher-accuracy sensor could be used here because of the smaller expected displacements, but it would not gain much because to get punch displacement, this measurement must be subtracted from the measurement of the LK-G407 sensor, which dominates the uncertainty.

3.2 Dynamic Punch Plate Testing

3.2.1 Dynamic Tests Performed

Testing was performed under EDP Mech-642, and raw instrumentation data and shot set-up information is archived in the Building 860 EDP system. The dynamic tests performed are summarized in Table 4. The tests have been sorted according to sample identification (ID) in order to group similar rows next to each other. The VXI test number refers to the raw data files associated with each test. These test numbers are used in the legends of the plots shown in Figure 93 and those presented in Appendixes A and B. A total of eight mild steel plates were tested with the flat (i.e., cylindrical) punch and five with the conical punch. Three abrasion-resistant plates were tested with the conical punch. Also tabulated in Table 4 is the impact velocity calculated from the carriage displacement data. This indicates that the impact velocity is fairly repeatable for the same drop height.

Table 4. Dynamic Tests Performed

VXI Test	Drop Height (inch)	Impact Velocity from Displacement (fps)	Felt Stop (inch)	Sample ID	Material	Punch	Strain	Notes
1	48	—	2	WMS_FP1	0.060" Mild Steel	Flat	No	Adapter hit plate: strain, load cell, and displacement, data not useable.
3	120	—	3	WMS_FP2	0.060" Mild Steel	Flat	No	Displacement data not useable.
6	120	47.6	3	WMS_FP3	0.060" Mild Steel	Flat	No	No strain data.
7	120	47.2	3	WMS_FP4	0.060" Mild Steel	Flat	No	—
8	48	27.6	3	WMS_FP5	0.060" Mild Steel	Flat	No	DIC cameras did not capture.
9	48	27.9	3	WMS_FP6	0.060" Mild Steel	Flat	No	Probable bad IRIG trigger time.
10	120	47.5	3	WMS_CP1	0.060" Mild Steel	Conical	No	First of conical punches, triggers on stop ring.
11	120	47.0	3	WMS_CP2	0.060" Mild Steel	Conical	No	—
12	48	25.4	3	WMS_CP3	0.060" Mild Steel	Conical	Yes	—
13	120	47.3	3	WMS_CP4	0.060" Mild Steel	Conical	Yes	—
14	48	27.5	3	WMS_CP5	0.060" Mild Steel	Conical	No	—
15	120	46.1	3	WMS_FP7	0.060" Mild Steel	Flat	Yes	—
16	48	27.4	3	WMS_FP8	0.060" Mild Steel	Flat	Yes	SG1-R not measured.
17	120	46.2	3	ARP_CP2	0.188" ARP	Conical	Yes	Added 0.045" shims to compensate for bowed fixture.
18	120	46.5	3	ARP_CP1	0.188" ARP	Conical	Yes	Added 1.3" thick empty pipe flange to the felt stop stack.
19	120	45.5	3	ARP_CP3	0.188" ARP	Conical	Yes	Added 1.3" thick empty pipe flange to the felt stop stack.

3.2.2 Anomalies from Dynamic Tests

Some issues in the data acquisition setup were resolved after the first several tests were conducted. The carriage displacement data are not usable for Tests 1 and 3, and the first two attempted strain gage measurements (Tests 1 and 6) were not successful. This is why eight mild steel-flat punch specimens were tested instead of the planned five. Also, on Test 1 the 2-inch felt thickness compressed enough for the punch adapter block to contact the plate. This thickness was increased to 3 inches for subsequent tests. On the first abrasion-resistant plate test, the weld between the plate and the pipe flange failed. An empty pipe flange was added to the felt stack to

further limit the punch displacement. The weld on the remaining two ARP samples remained intact.

On Test 3, the reaction mass traveled further than it had in development testing and the fixture contacted the mirror bracket in late time and the mirror was cracked. Post-test investigation found that the pressure on the reaction mass shock absorbers had decreased over time to ~300 pounds per square inch (psi). The pressure was recharged to ~600 psi and the reaction mass travel was appropriately limited for other tests.

Because of a software error in configuring the pretrigger memory, the DIC cameras did not capture the event on Test 8. Preliminary checks indicate good DIC data were obtained on all other tests.

After repeated high-level tests, the top plate of the reaction mass fixture began showing signs of plastic deformation. The flanges would not sit flat because of bending of the top plate. Strips of steel shim stock 0.045 inches thick and ~1-inch long were added on either side of the center bolt on the front and back of the pipe flange to take up this difference. These were added prior to Test 17. Future work should include the design and fabrication of a more robust fixture.

3.2.3 Observations from Dynamic Tests

Figures 69–71 show pictures of representative test specimens. All mild steel-flat punch specimens had a disk of steel punched out and then formed four petals. The mild steel-conical punch specimens also all formed four petals. The same punch was used repeatedly for the mild steel tests and showed no visible signs of wear. The abrasion-resistant plate specimens showed nonclassic failure patterns. An initial plug was formed in each case with a diameter corresponding to the flattened portion of the punch (see Figure 74). Other irregularly shaped fragments were also generated. Each plate has an irregular pattern of cracks that tend to follow a spiral pattern. The punches were severely damaged in each test. It appears that the round tip of the punch was flattened while creating the initial plug, then a step was created in the conical punch as it was forced into this hole. The large plastic deformation on the surface of the punch even captured fragments of the plate in some tests (see Figure 72). The abrasion-resistant plates and punches used showed heat-induced discoloration caused by frictional heating or plastic work (see Figure 72 and Figure 73).

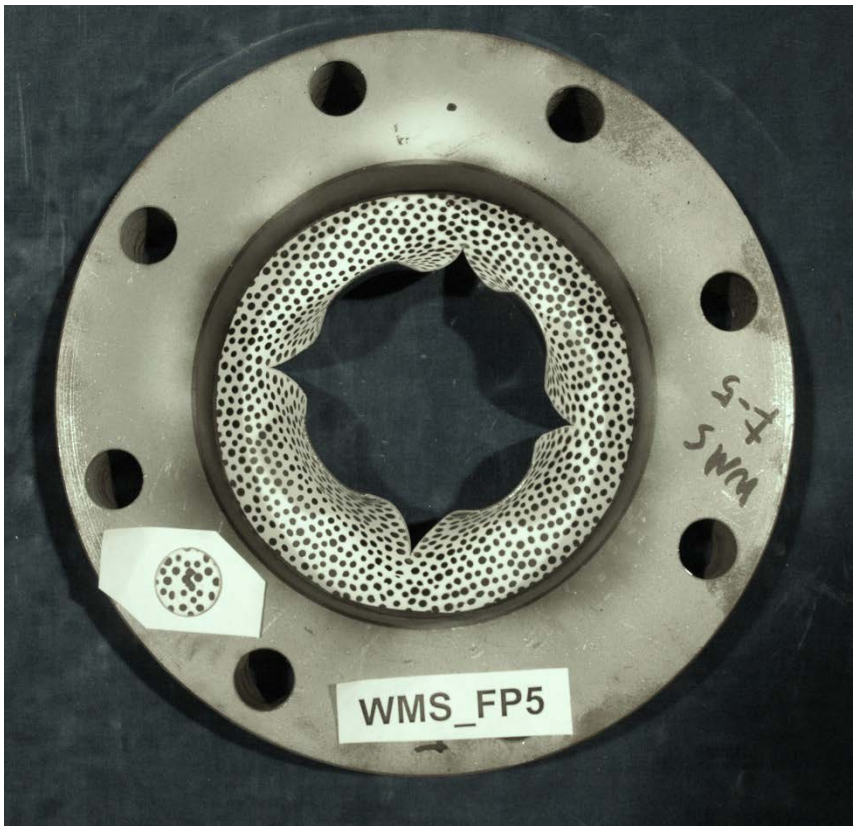

Figure 69. Typical mild steel-flat punch specimen

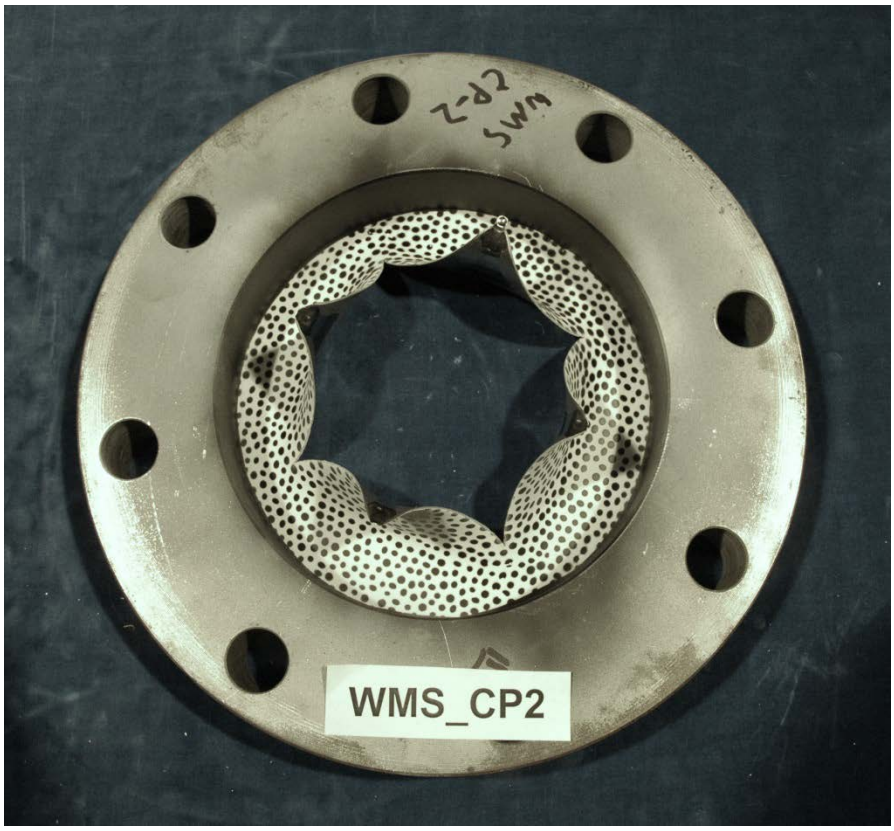

Figure 70. Typical mild steel-conical punch specimen

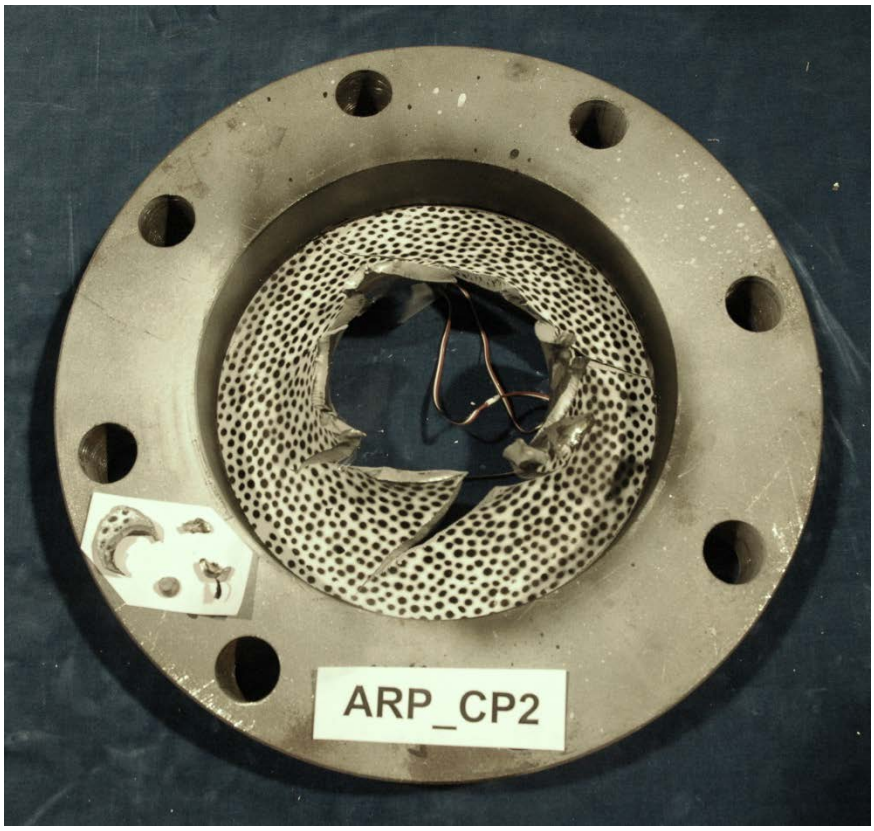

Figure 71. Typical ARP conical punch specimen

Figure 72. Conical punch following ARP_CP2 test

Figure 73. Plate fragment from ARP_CP3 tests showing heat induced discoloration

Figure 74. Plugs recovered from (ARP_CP1 through ARP_CP3 from left to right)

3.3 Dynamic Data Analysis

Significant data processing was employed to get the data into a usable form. The data processing issues are described in the following subsections.

3.3.1 Filtering

Time domain digital filtering is commonly applied to dynamic test data to present relevant information and eliminate noise. This section attempts to describe how the decisions regarding filter levels were made. The filter levels discussed in this report refer the −3-decibel (dB) frequency in hertz (Hz) of an eight-pole, zero-phase shift Butterworth filter.

The laser displacement gage is known to have a discrete update rate (40 µs, 25 kHz) limited by the internal electronics of the sensor. This leads to *stair steps* in the displacement data that are not physical. Filtering at 5,000 Hz or 1,000 Hz eliminates this effect (see Figure 75 and Figure 76).

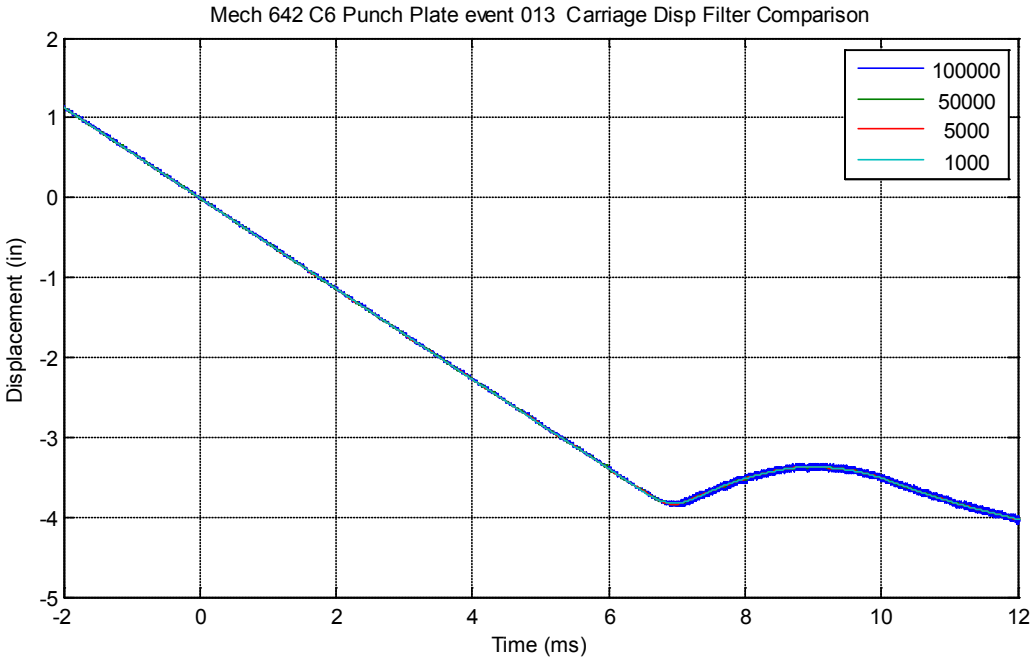

Figure 75. Typical displacement data filter comparison

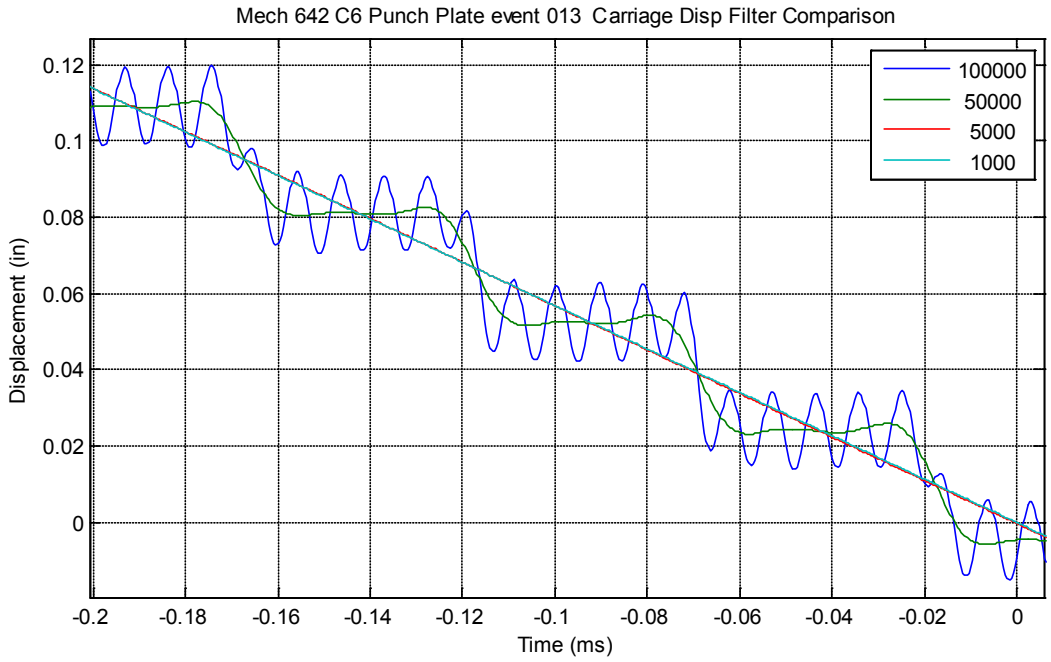

Figure 76. Close-up of displacement filter comparison showing 40-µs update interval

Figure 77 through Figure 79 show typical data for carriage accelerometer, load cell, and strain gage data filtered at different frequencies. Figure 80 through Figure 82 show the fast Fourier transform (FFT) magnitude for this same data. From these figures it is clear that the accelerometers and load cells have more high-frequency content than the strain gages. This is a result of the internal transducer resonance and dynamic structural response of the carriage assembly. Because of this, strain and acceleration should be filtered at a lower level to present the rigid body event.

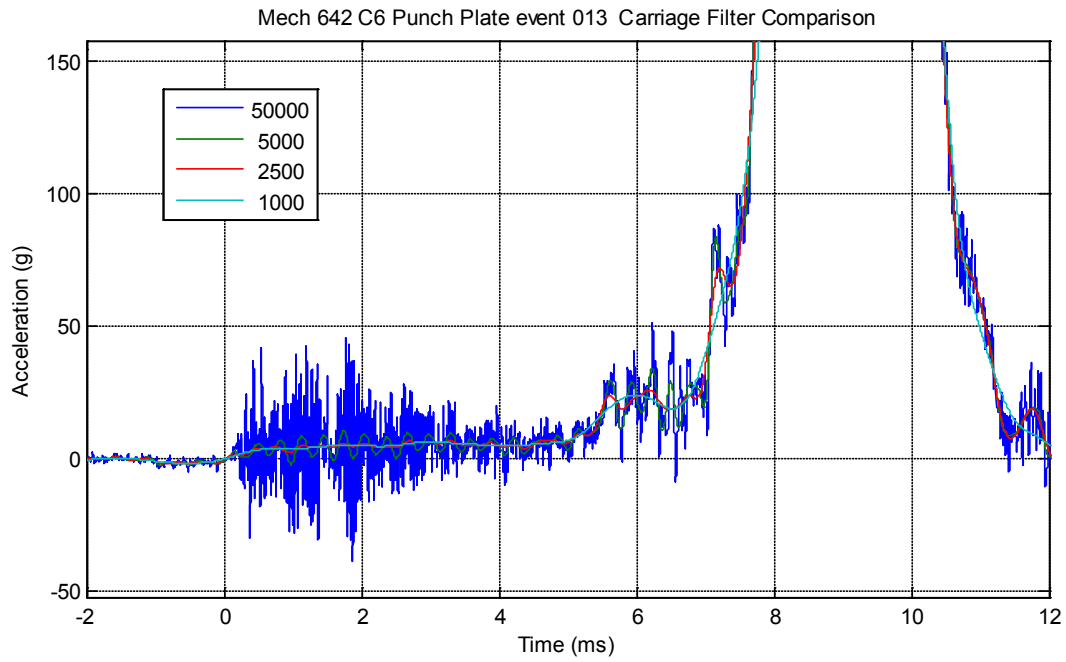

Figure 77. Carriage 6K accelerometer filter-level comparison

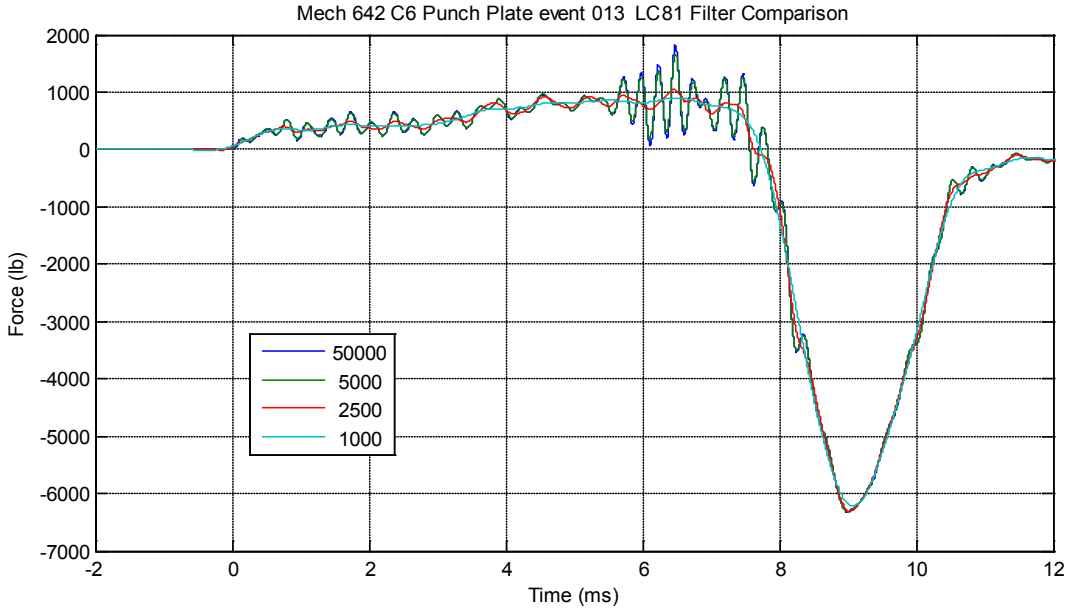

Figure 78. Load cell LC81 filter-level comparison

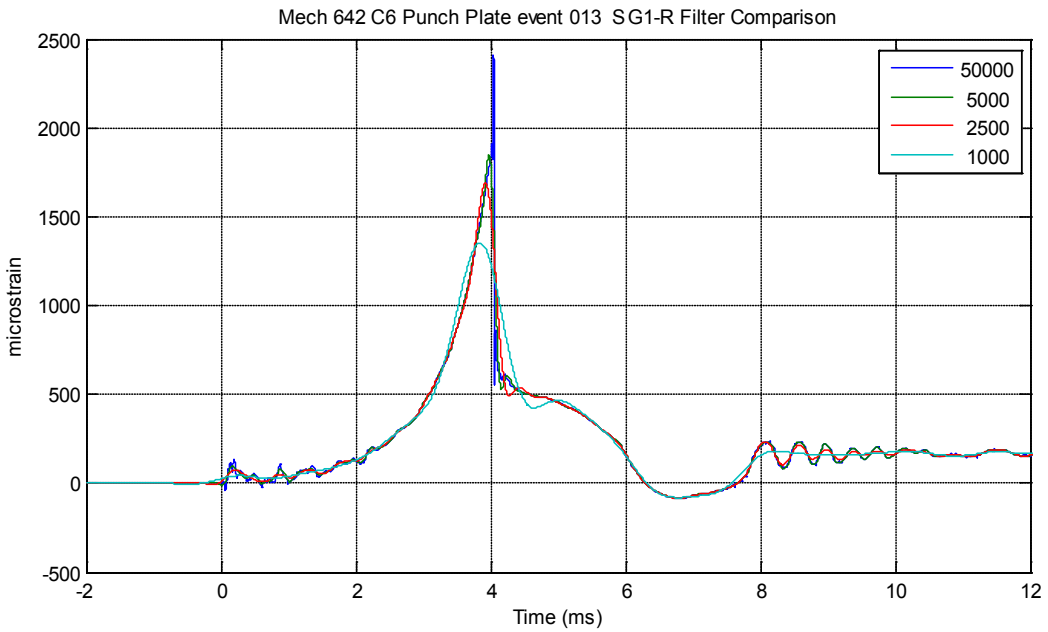

Figure 79. Strain Gage SG1-R filter-level comparison

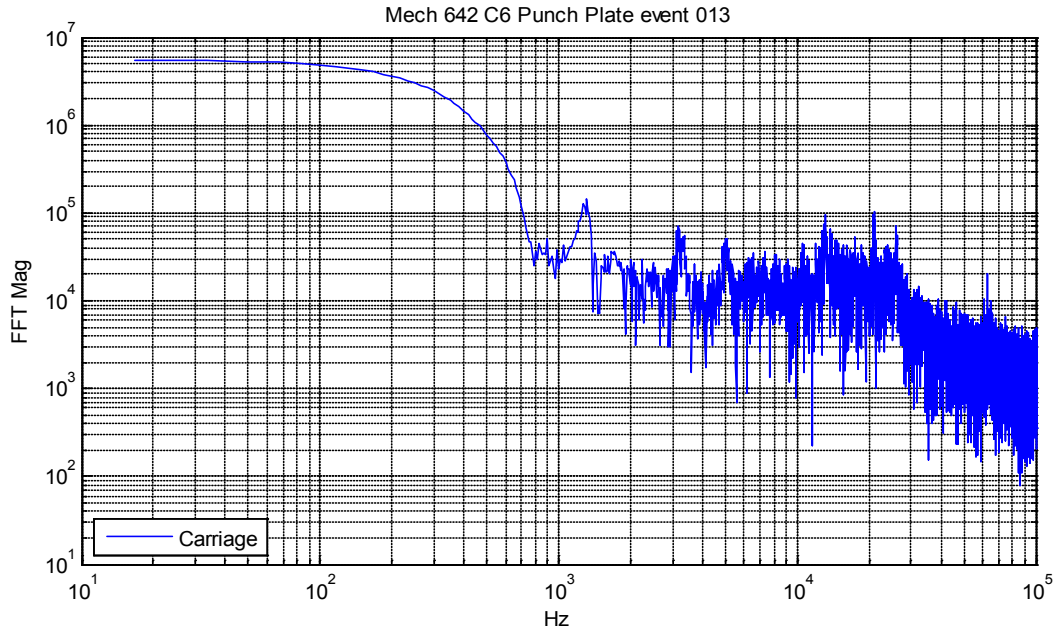

Figure 80. Carriage 6K accelerometer frequency content

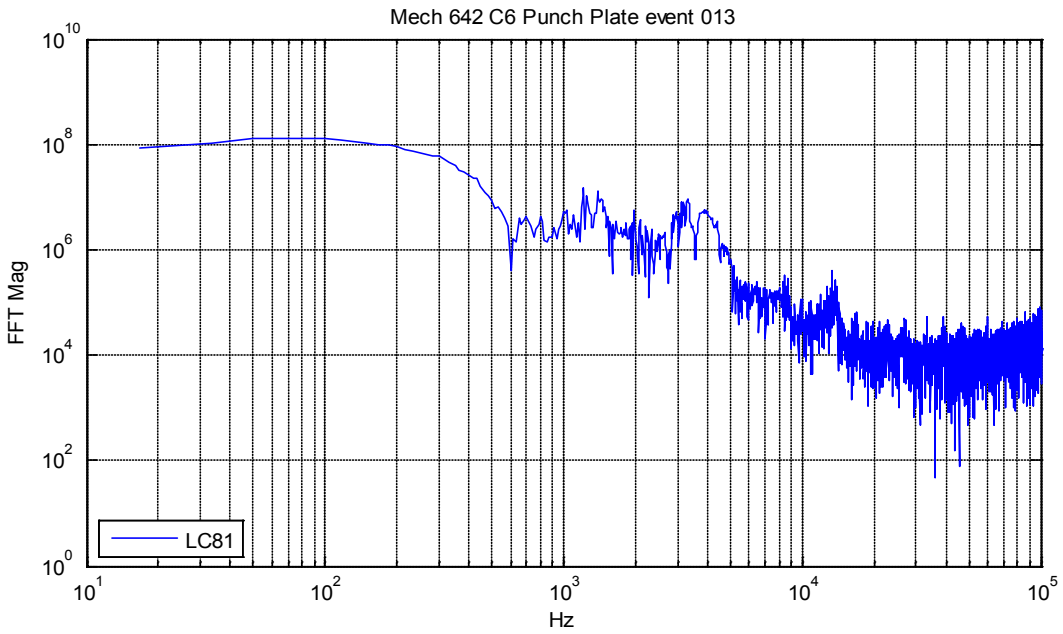

Figure 81. Load cell LC81 frequency content

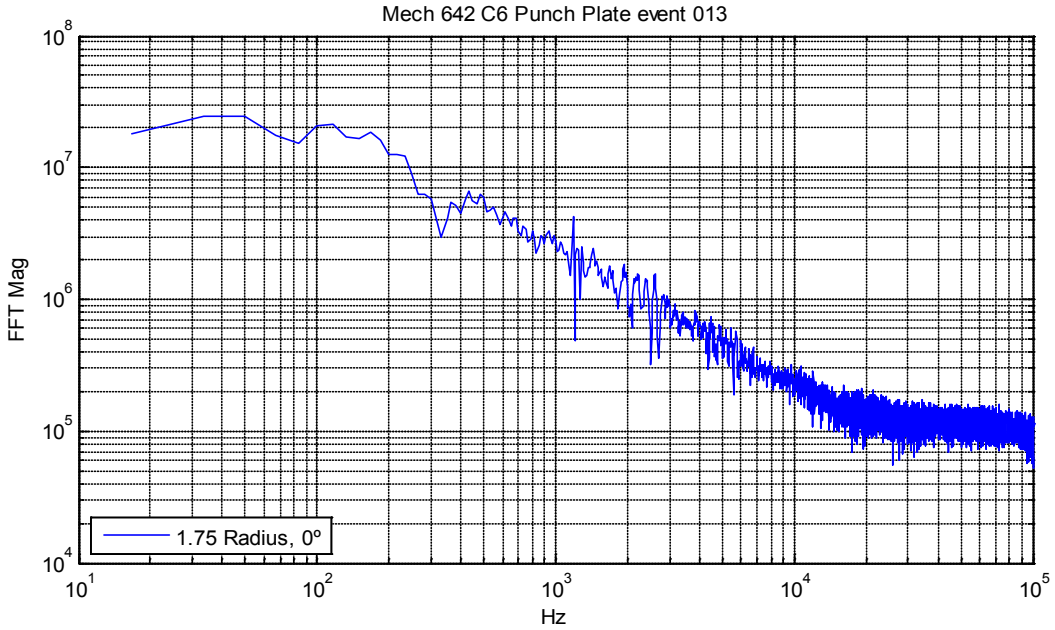

Figure 82. Strain Gage SG1-R frequency content

Figure 83 provides additional insight into the dynamics of the carriage. It presents a frequency response function calculated between a 7270-20K accelerometer mounted on the top of the carriage to the same model accelerometer mounted on the punch adapter. A magnitude of 1, phase of 0, and coherence of 1 indicates rigid-body behavior. As shown in Figure 82, this is largely true up to 1,000 Hz. The first identifiable resonance is at 1,500 Hz, which is lower than expected from coarse calculations performed during the design of the load cell fixture. Future work should investigate the source of these dynamics and possibly modify the design to improve useful bandwidth.

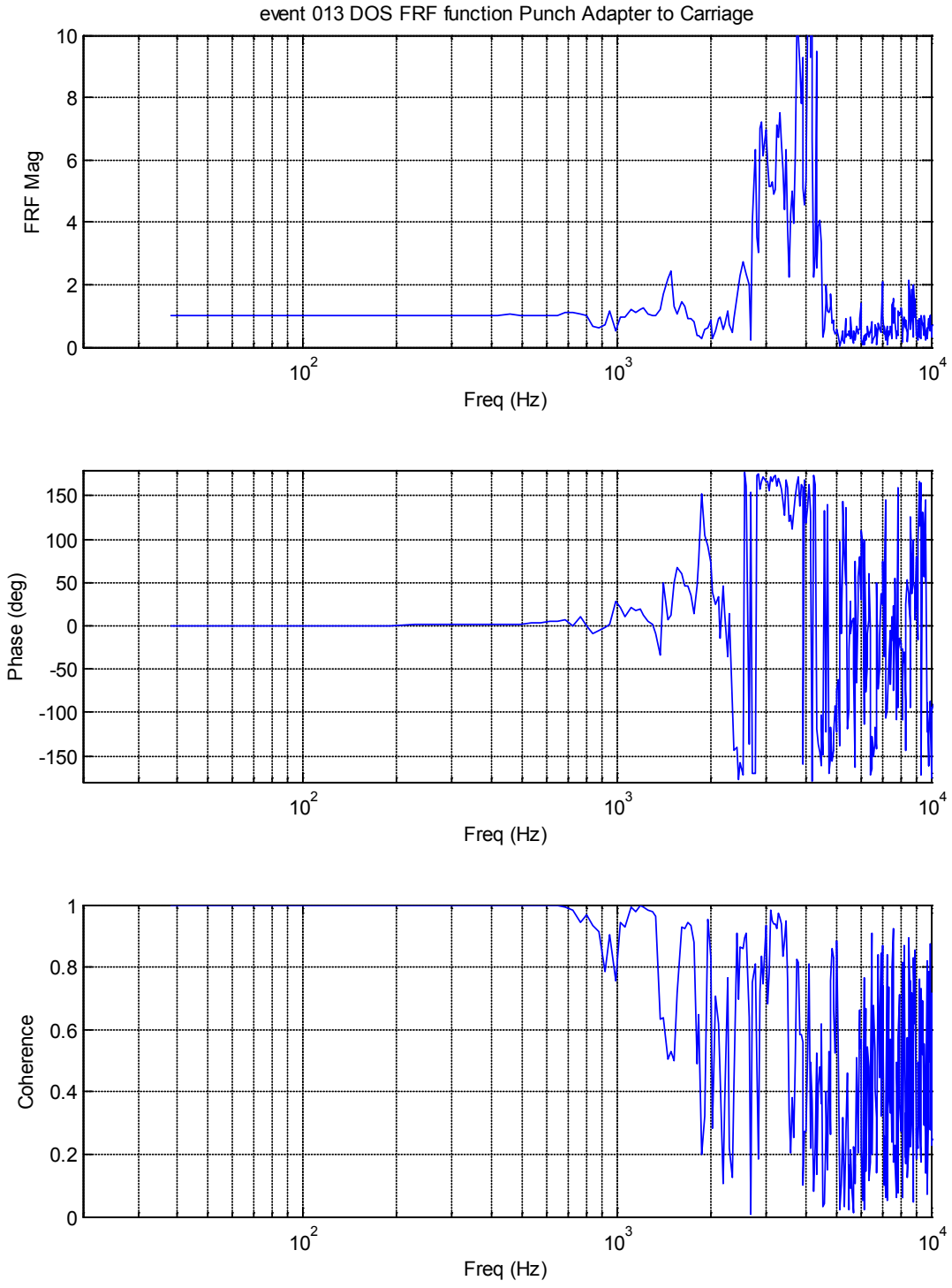

Figure 83. Acceleration frequency response function: punch adapter to carriage

3.3.2 Time Zero Reference

The VXI data system is set up to trigger on an acceleration threshold from the 6K accelerometer mounted on the carriage. The time of this threshold crossing is recorded as zero time (i.e., $t = 0$) in the raw data. The TRIGGER OUT signal, which trigger the cameras and the PC IRIG capture card, goes from low to high 14.8 µs after this recorded zero time. This small delay appears to be an inherent part of the data system circuitry design, but it is very repeatable, so it can still be used for synchronization. Figure 84 overlays the recorded trigger signals for all tests. Several troubleshooting tests were performed in this series without camera coverage, and these show a lower voltage level as expected (refer to Subsection 3.1.2 the regarding camera setup).

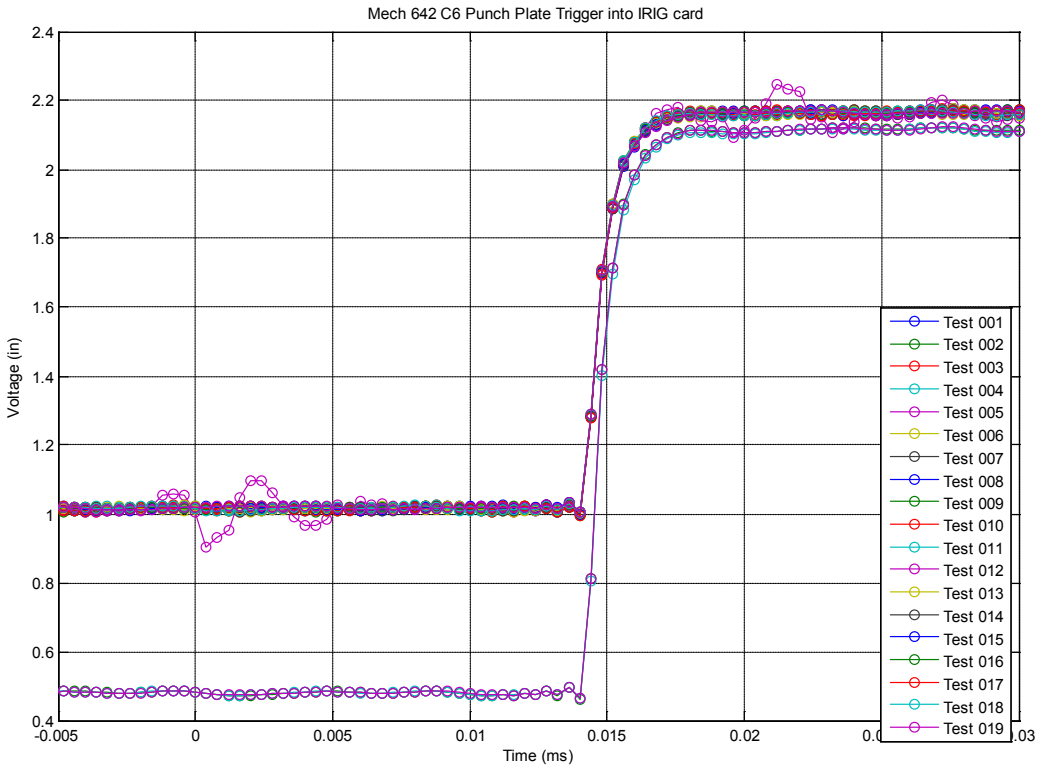

Figure 84. Trigger output signal

The exact timing of the accelerometer threshold crossing can vary from test to test. In particular, the mild steel-conical punch tests did not cross the threshold until the carriage hit the felt stop. In order to facilitate test-to-test comparisons of data, a common zero reference was selected for post-processing of the data. The common time zero was selected to be when the sum of the filtered load cell data first exceeded 800 N. This approximates first contact of the punch with the plate. The carriage displacement was also set to zero at this point in the post-processed data.

3.3.3 Acceleration

The 7270-20K accelerometer mounted on the punch adapter showed much more high-frequency response than the 20K or 6K accelerometers mounted on the carriage. Figure 85 shows the as-acquired and filtered acceleration data for a typical test. The metal-on-metal impact evidently creates enough high-frequency input to excite the internal resonant frequency of this gage (typically > 350 kHz for a 7270-20K accelerometer). This type of response was not totally unexpected, and the data system was set up to avoid clipping the signal even at these high levels. Figure 86 overlays the three filtered accelerometer traces and the raw data integrated to velocity. Agreement is generally very good, except the punch adapter accelerometer does show differences. More investigation is needed to determine if this is reasonable to expect because of the dynamics of the system or if the punch adapter data are compromised because of the high response levels. Figure 87 compares the FFT of the 7270-20K accelerometer on the carriage to the one on the punch adapter. One common rule of thumb for assessing data from these accelerometers is that the magnitude of the accelerometer resonance should not be larger than the low-frequency response. The mild steel-flat punch adapter data fail this rule of thumb. Similar plots are shown for a conical punch, mild steel test in Figure 88 through Figure 90. The resonant response of the punch adapter accelerometer is much lower for these tests as seen in both the time and FFT plots. Also, the filtered acceleration and integrated velocity overlay much more closely. These observations further indicate that the flat punch data are suspect.

This location is a good candidate for a mechanically isolated accelerometer. There is no room in the current assembly for a commercial 7270-AM6. However the Sandia 1520-developed PSR wafer mount commonly used in RB hostile environment tests may be a good option for future testing.

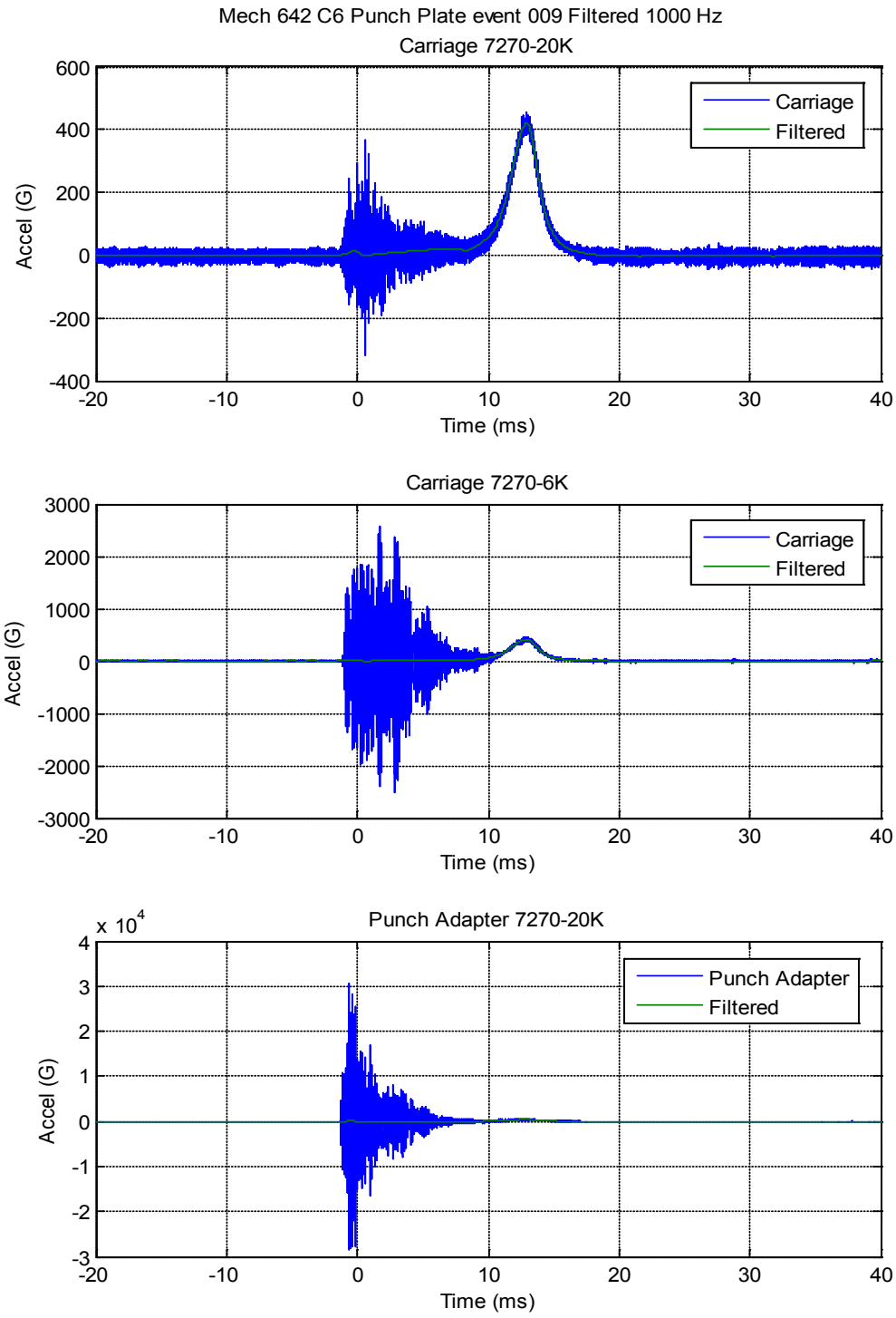

Figure 85. Typical mild steel-flat punch accelerometer data (WMS_FP6)

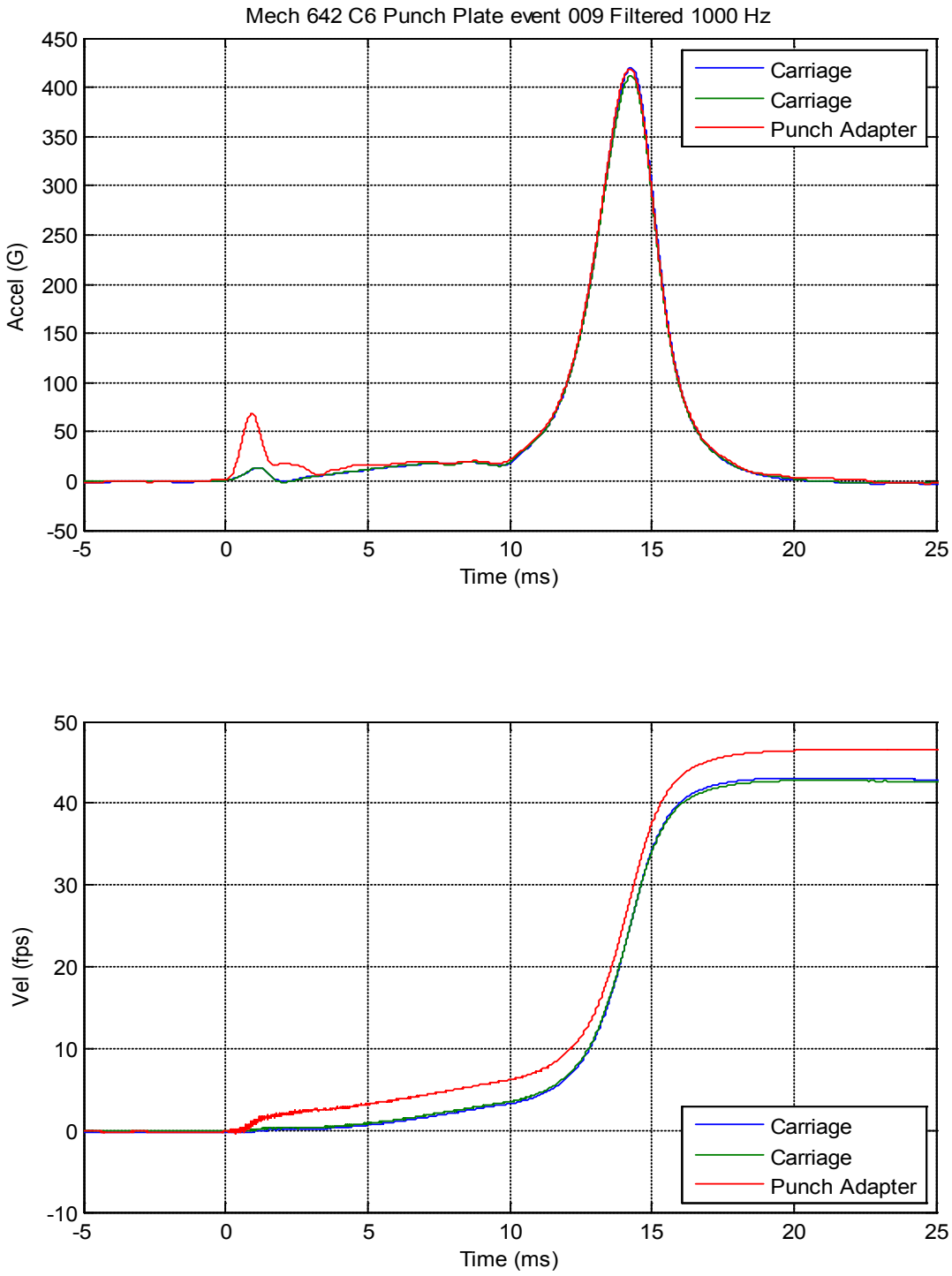

Figure 86. WMS_FP6 accelerometer data filtered and integrated overlay

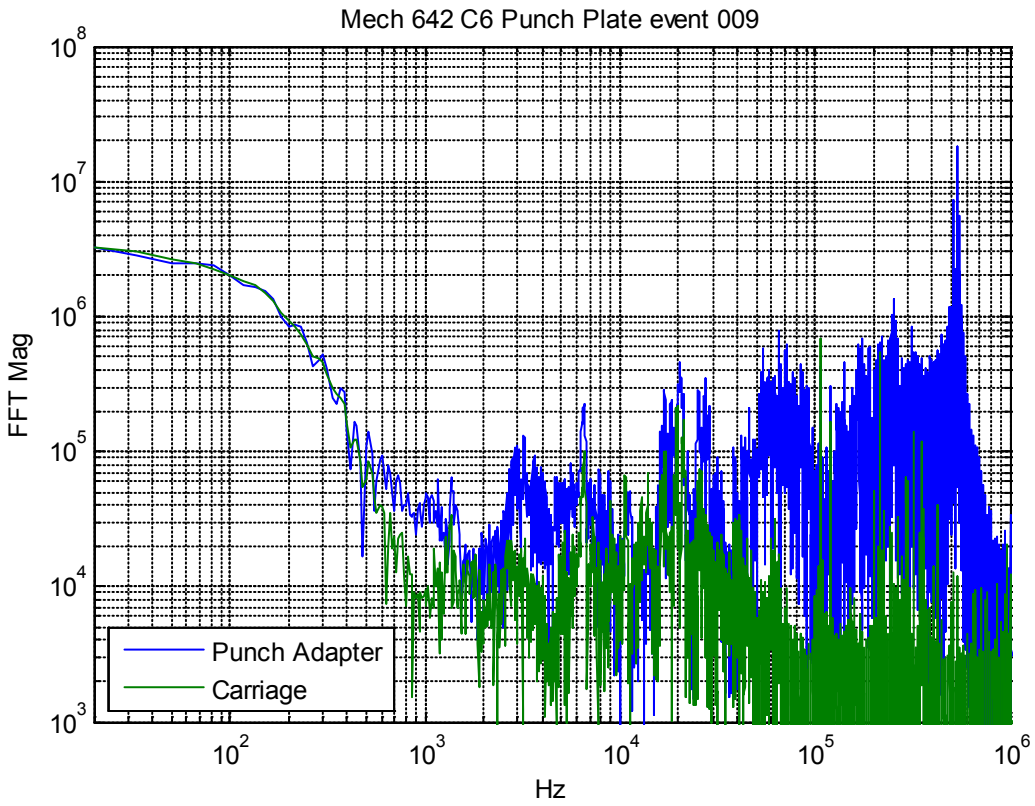

Figure 87. WMS_FP6 7270-20K carriage to punch adapter FFT comparison

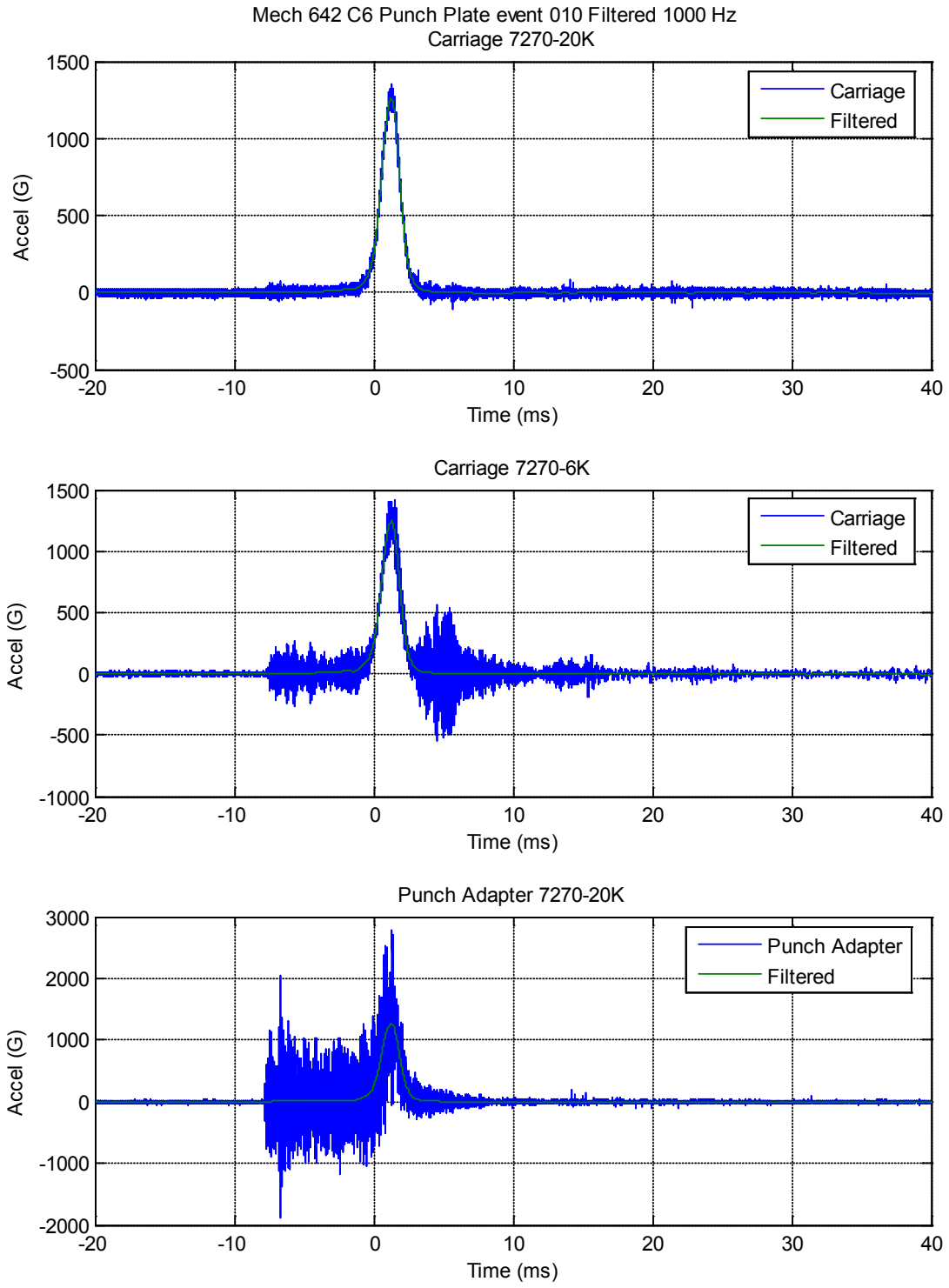

Figure 88. Typical mild steel-conical punch accelerometer data (WMS_CP1)

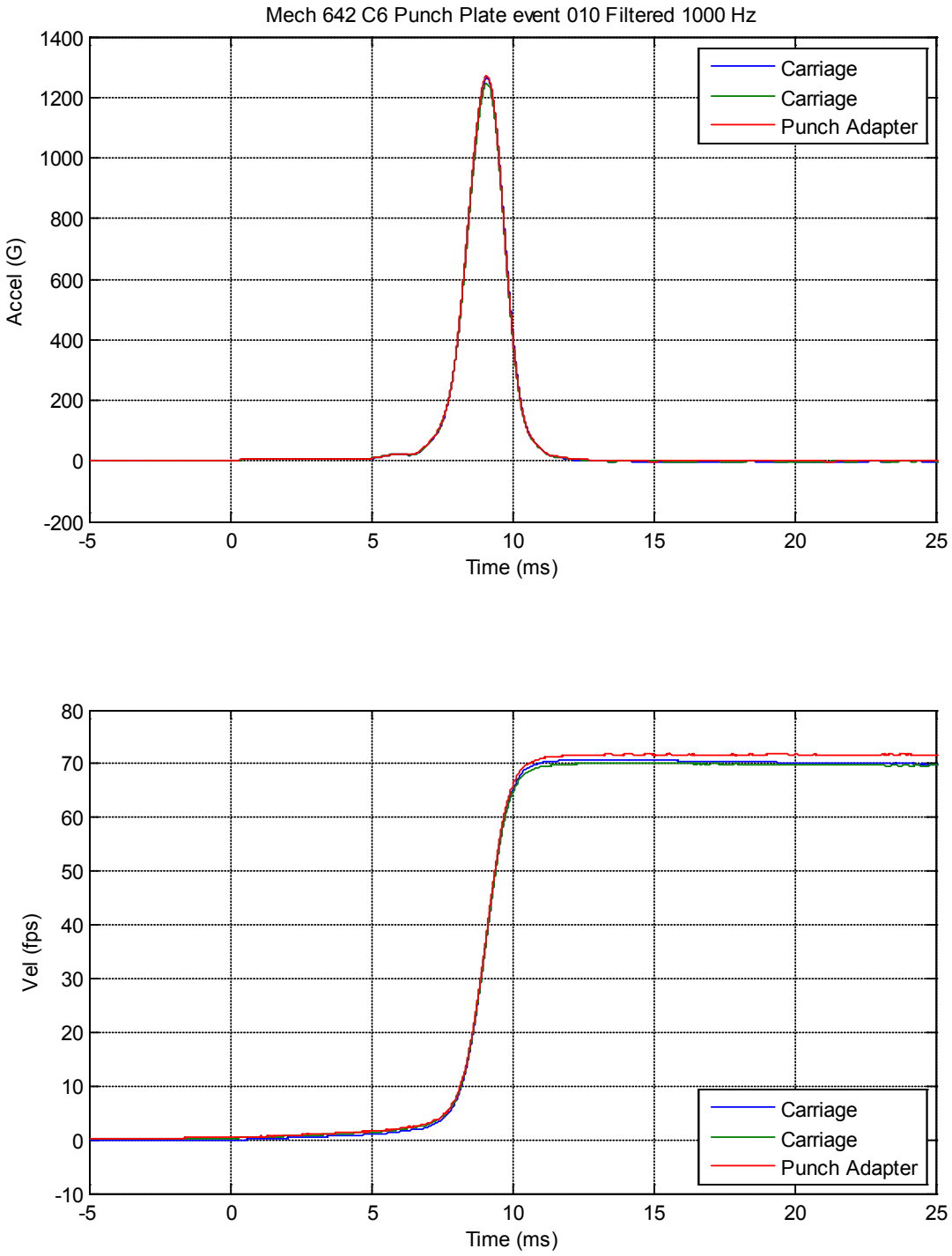

Figure 89. WMS_CP1 accelerometer data filtered and integrated overlay

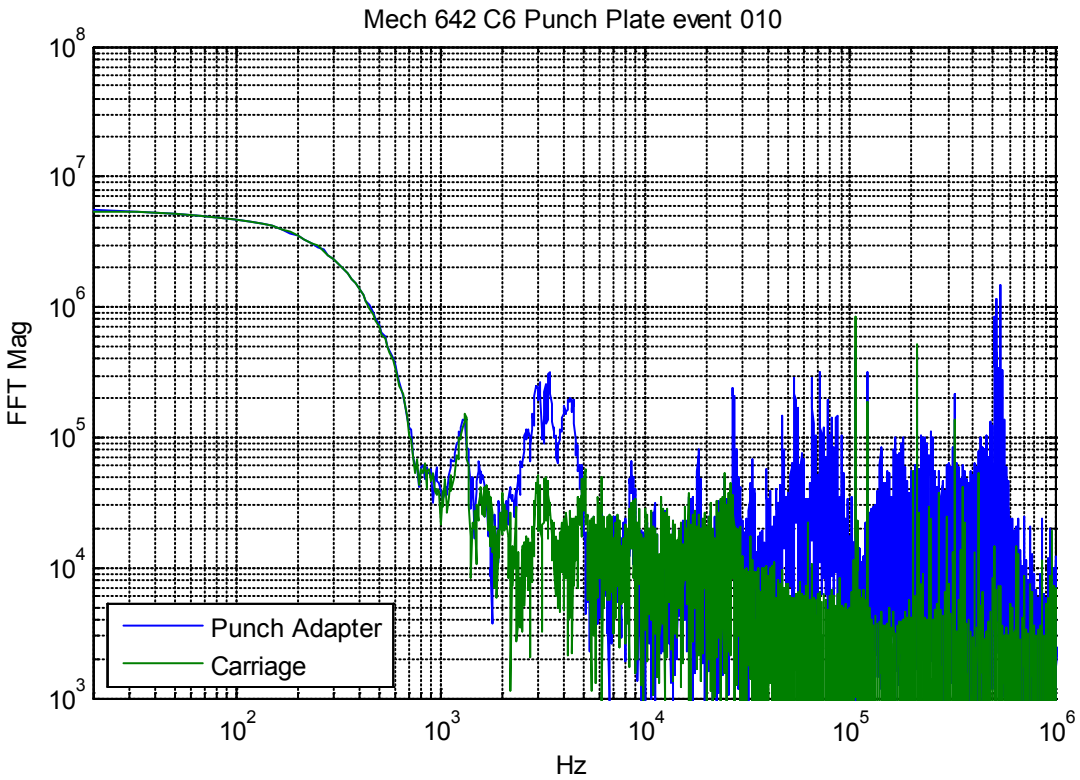

Figure 90. WMS_CP1 7270-20K carriage to punch adapter FFT comparison

3.3.4 Force

Typical individual load cell data are shown in Figure 91 through Figure 93. Also plotted are the total carriage assembly mass (311 lbs) times acceleration. This should represent the total external force applied to the carriage. This force becomes quite large when the felt carriage stop engages. The punch and adapter mass (18.25 lbs) times acceleration is also plotted. This should represent the inertial correction to the measured force data. This correction has not yet been implemented, in part, because of the suspicious data from the punch adapter accelerometer in many tests.

All test geometries show good uniformity between the four load cells during the initial loading. After penetration, there are greater differences, which are likely caused by unbalanced lateral loads on the punch applying moments to the load cell assembly. The mild steel specimens show relatively small variations. However, the abrasion-resistant plates show very large differences where one load cell exceeded its recommended range in compression and the opposite load cell sees 5,000 lbs of tension load. This seems reasonable because of the high strength and stiffness of this plate and the lack of symmetry in the fracture pattern. Also note that in the abrasion-resistant plate tests, the load cells did not go into tension even though the carriage saw ~500 g rigid-body acceleration when it engaged the felt stop. This is a result of the high residual stiffness of the punctured metal plate applying significant residual force on the punch.

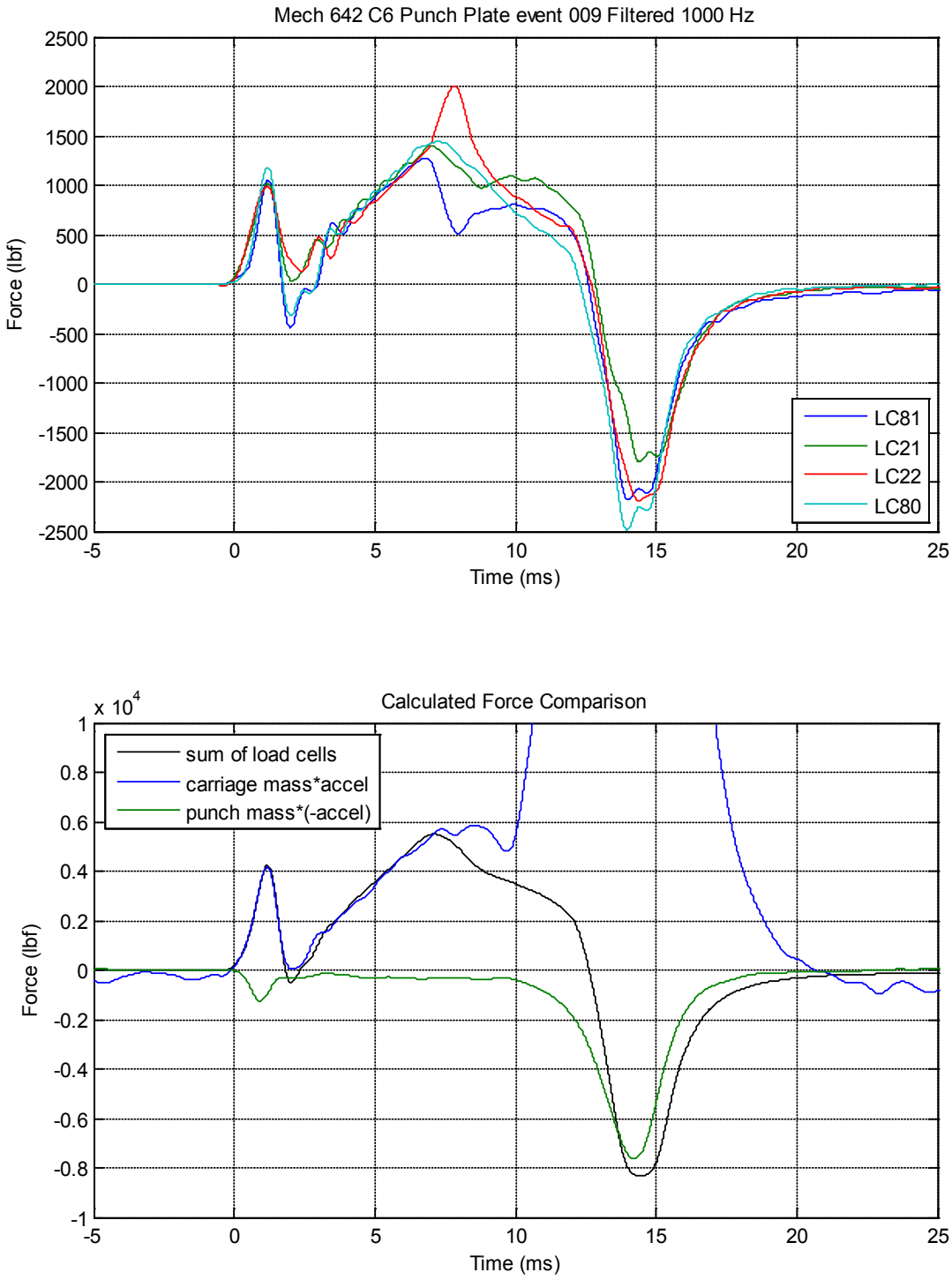

Figure 91. Typical mild steel-flat punch load cell data

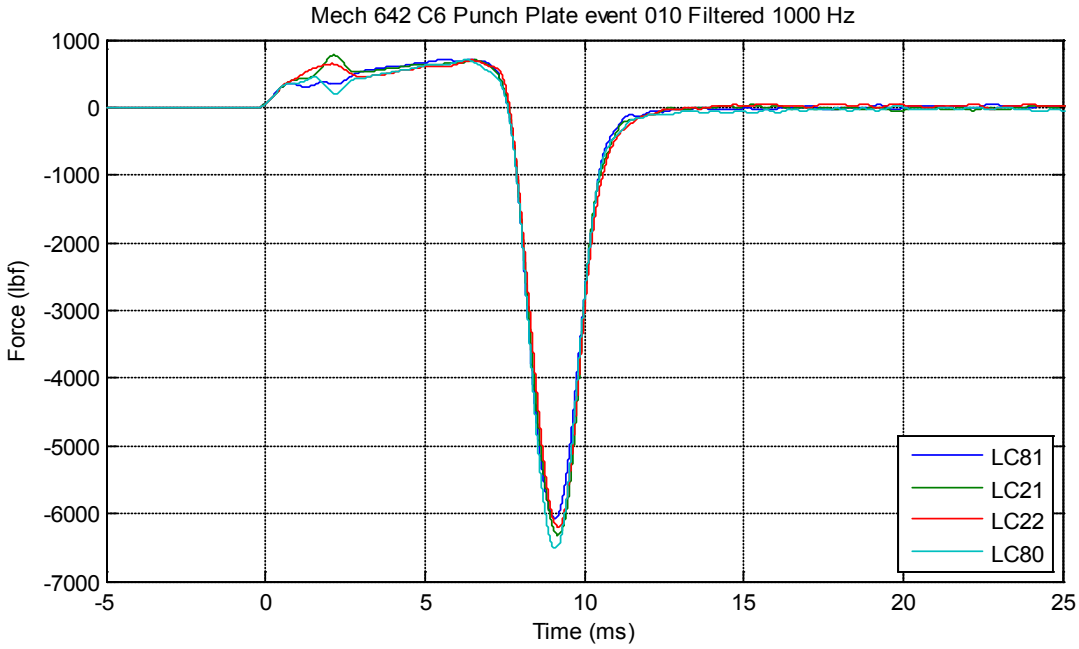

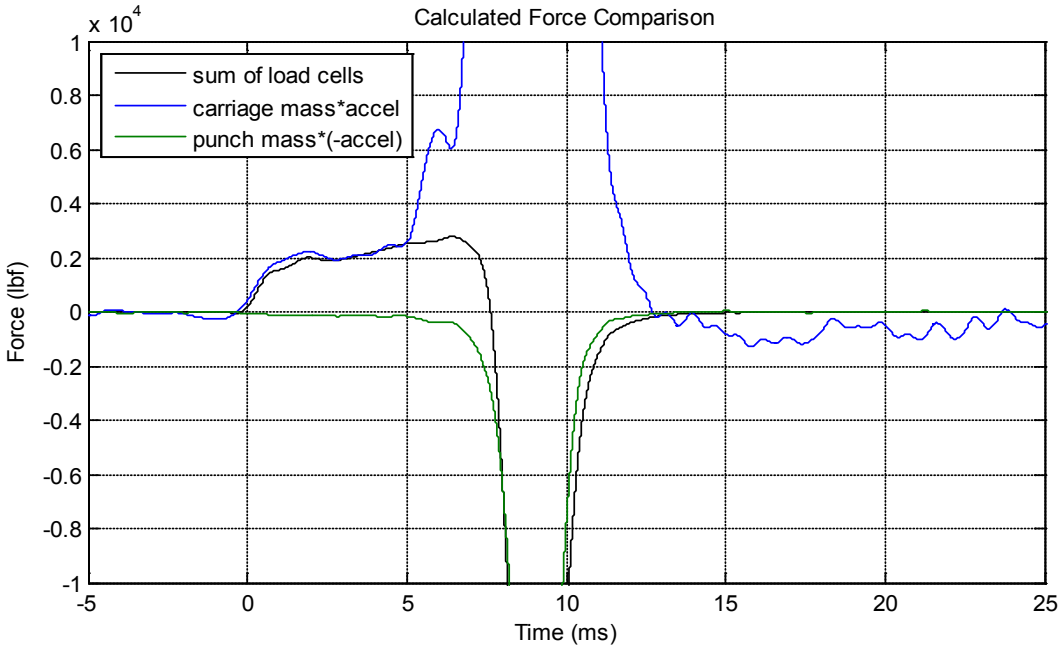

Figure 92. Typical mild steel-conical punch load cell data

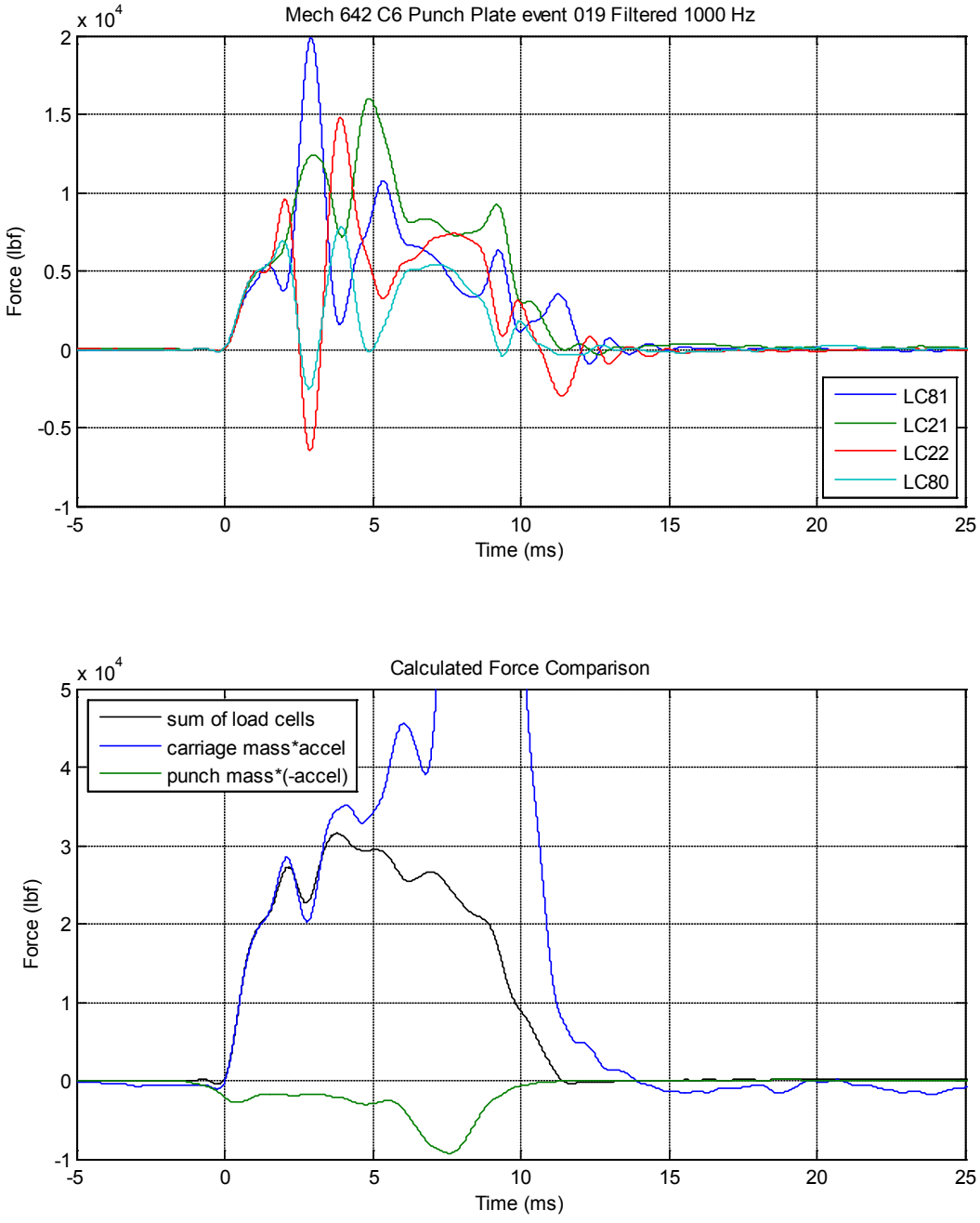

Figure 93. Typical ARP conical punch load cell data

3.3.5 Displacement

The carriage displacement data on several tests have dropouts and nonphysical behavior. Care must be exercised when interpreting these data because data that look obviously bad at a high-filter bandwidth (e.g., 25,000 Hz) can look plausible when filtered at 1,000 Hz as shown in Figure 94. Future processing of the data should trim off these questionable portions. The fixture

displacement gage did not provide useable data because of the frequency and the length of the dropouts. The laser displacement sensor used employs a visible red laser. It is possible that the very high ambient light level in the test location from the DIC lights caused the laser sensor to be unreliable.

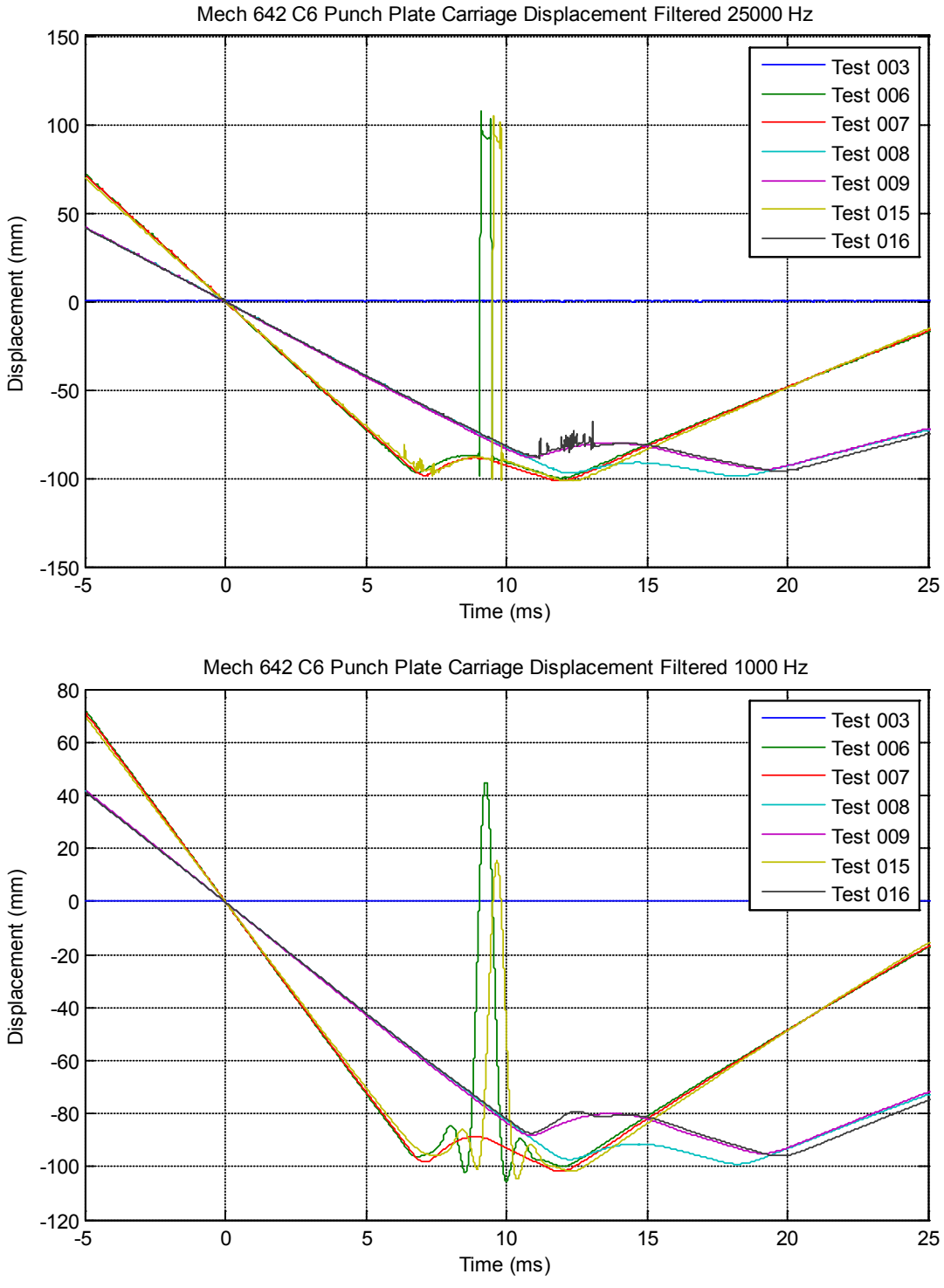

Figure 94. Carriage displacement data curves: 25,000-Hz filter and 1,000-Hz filter

3.3.6 Strain

Strain gage data benefit from being the most direct measurement of the behavior of the plate being punctured. Strain gages do not suffer from internal resonances like accelerometers. Also, the structural dynamics of the carriage, punch, and load cell assembly are unlikely to show up in strain gages mounted on the plate. Because of this, the strain gages were filtered at 20,000 Hz to clean up low-level noise without distorting the dynamic response (see Figure 95). However, a single strain gage datum can be difficult to interpret because it is a single-point measurement, and variations in crack locations relative to a gage can drastically change the stress state making comparisons difficult from test to test or between "equivalent" locations on the same test as shown in Figure 95.

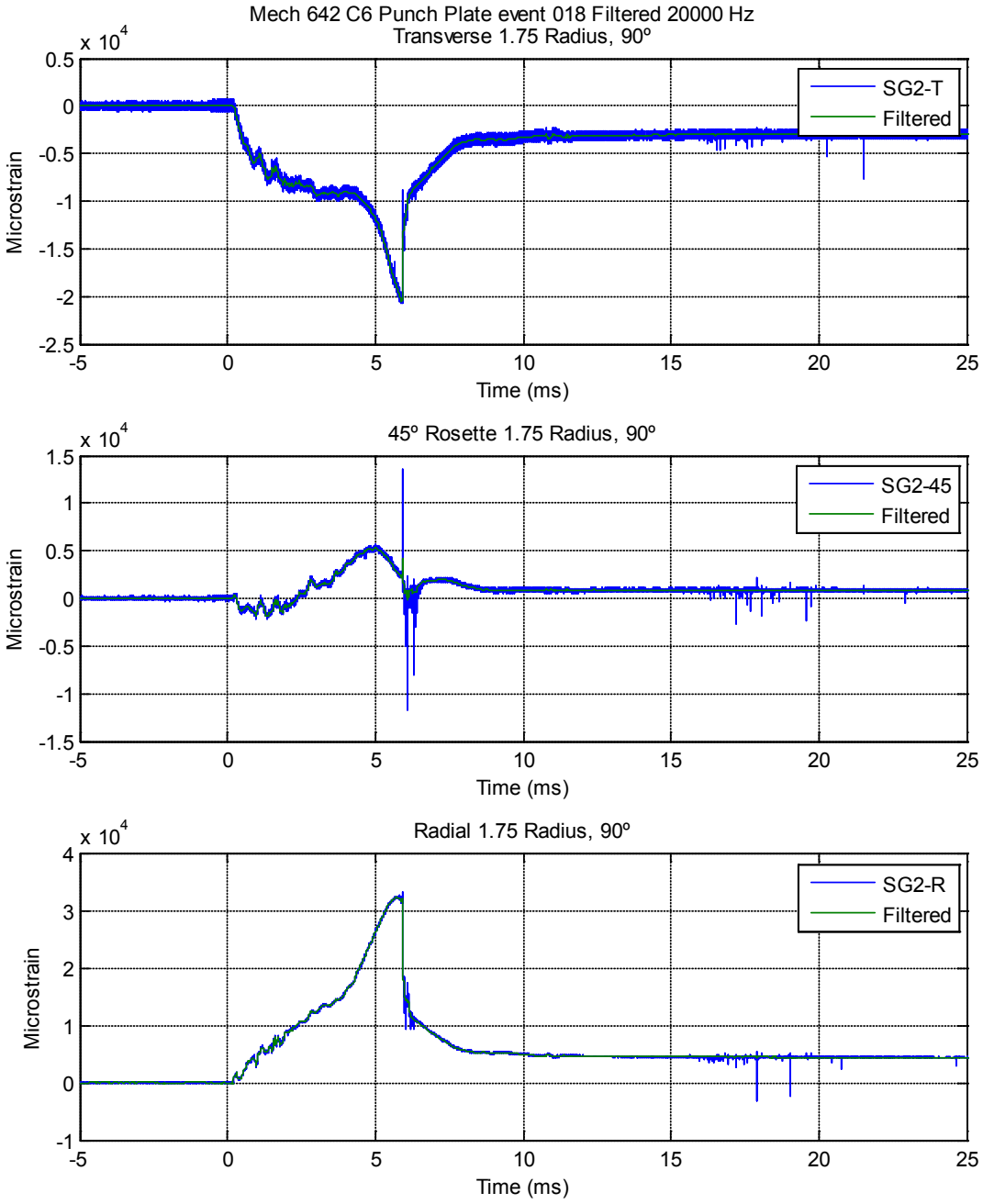

Figure 95. Raw and filtered strain gage data (ARP_CP1)

3.3.7 Data Quality Overview

An assessment of data quality for each channel on each test conducted is presented in Table 5.

Table 5. Dynamic Punch Data Quality Assessment

	Channel	1	2	3	4	5	6	7	8	9	10	11	12	13	14	15	16
VXI test	Drop Height (in)	Sample ID	carriage accel 20K	carriage accel 6K	adapter accel 20K	LC81	LC21	LC22	LC80	fixture disp	carriage disp	trigger	SG1-T	SG1-45	SG1-R	SG2-T	SG2-45	SG2-R
1	48	WMS_FP1	0	0	1	2	2	2	2	2	2	0	2	2	2	2	2	2
2	3	prelim	0	0	0	2	2	2	2	2	2	0	n/a	n/a	n/a	n/a	n/a	n/a
3	120	WMS_FP2	0	0	2	0	0	0	0	2	2	0	n/a	n/a	n/a	n/a	n/a	n/a
4	120	prelim	0	0	0	0	0	0	0	2	2	0	n/a	n/a	n/a	n/a	n/a	n/a
5	12	prelim	0	0	0	0	0	0	0	2	1	0	n/a	n/a	n/a	n/a	n/a	n/a
6	120	WMS_FP3	0	0	1	0	0	0	0	2	1	0	2	2	2	2	2	2
7	120	WMS_FP4	0	0	2	0	0	0	0	2	0	0	n/a	n/a	n/a	n/a	n/a	n/a
8	48	WMS_FP5	0	0	1	0	0	0	0	2	0	0	n/a	n/a	n/a	n/a	n/a	n/a
9	48	WMS_FP6	0	0	1	0	0	0	0	2	0	0	n/a	n/a	n/a	n/a	n/a	n/a
10	120	WMS_CP1	0	0	0	0	0	0	0	2	1	0	n/a	n/a	n/a	n/a	n/a	n/a
11	120	WMS_CP2	0	0	0	0	0	0	0	2	1	0	n/a	n/a	n/a	n/a	n/a	n/a
12	48	WMS_CP3	0	0	0	0	0	0	0	2	1	0	0	0	0	1	0	1
13	120	WMS_CP4	0	0	0	0	0	0	0	2	0	0	0	0	0	0	0	0
14	48	WMS_CP5	0	0	0	0	0	0	0	2	0	0	n/a	n/a	n/a	n/a	n/a	n/a
15	120	WMS_FP7	0	0	1	0	0	0	0	2	1	0	1	1	1	1	1	0
16	48	WMS_FP8	0	0	1	0	0	0	0	2	1	0	1	1	2	1	1	1
17	120	ARP_CP2	0	0	1	1	1	1	1	2	0	0	0	0	0	0	0	1
18	120	ARP_CP1	0	0	2	1	1	1	1	2	0	0	0	0	0	0	0	0
19	120	ARP_CP3	0	0	1	1	1	1	1	2	0	0	n/a	n/a	n/a	n/a	n/a	n/a

Data Quality Key

0 no observed problems
1 dropouts; large noise spikes; possible non-linear response; use caution
2 data not acquired or not usable; clipped data

3.4 Data vs. Time

The acceleration, velocity change, displacement, force, and microstrain data vs. time for the following test types were grouped in various sets and overlain graphically in a series of plots to facilitate comparisons to quasi-static testing or modeling:

- Mild Steel, Flat Punch
- Mild Steel, Conical Punch
- Abrasion-Resistant Plate, Conical Punch

These plots are presented in Appendix A.

3.5 Data vs. Displacement

The load, microstrain, acceleration, velocity, and velocity change data vs. displacement for the following test were grouped in various sets and overlain graphically in a series of plots to facilitate comparisons to quasi-static testing or modeling:

- Mild Steel, Flat Punch
- Mild Steel, Conical Punch
- Abrasion-Resistant Plate, Conical Punch

These plots are presented in Appendix B.

The plots shown in Appendix B can be difficult to interpret because of regions of nonphysical data, either in displacement or the ordinate data. A future task is to trim off these regions of known bad data to make the valid data easier to interpret.

3.6 Full-Field Results and Comparison

3.6.1 Results

The dynamic data analysis of the mild steel plate punched with the conical punch, being representative of all of the dynamic cases, is presented here. Two different drop heights were used for these samples. Tests 12 and 14 used a carriage velocity of 26 fps and Tests 10, 11, and 13 used a 47-fps carriage velocity. Figure 96 plots the principal strain versus time for the two different drop heights.

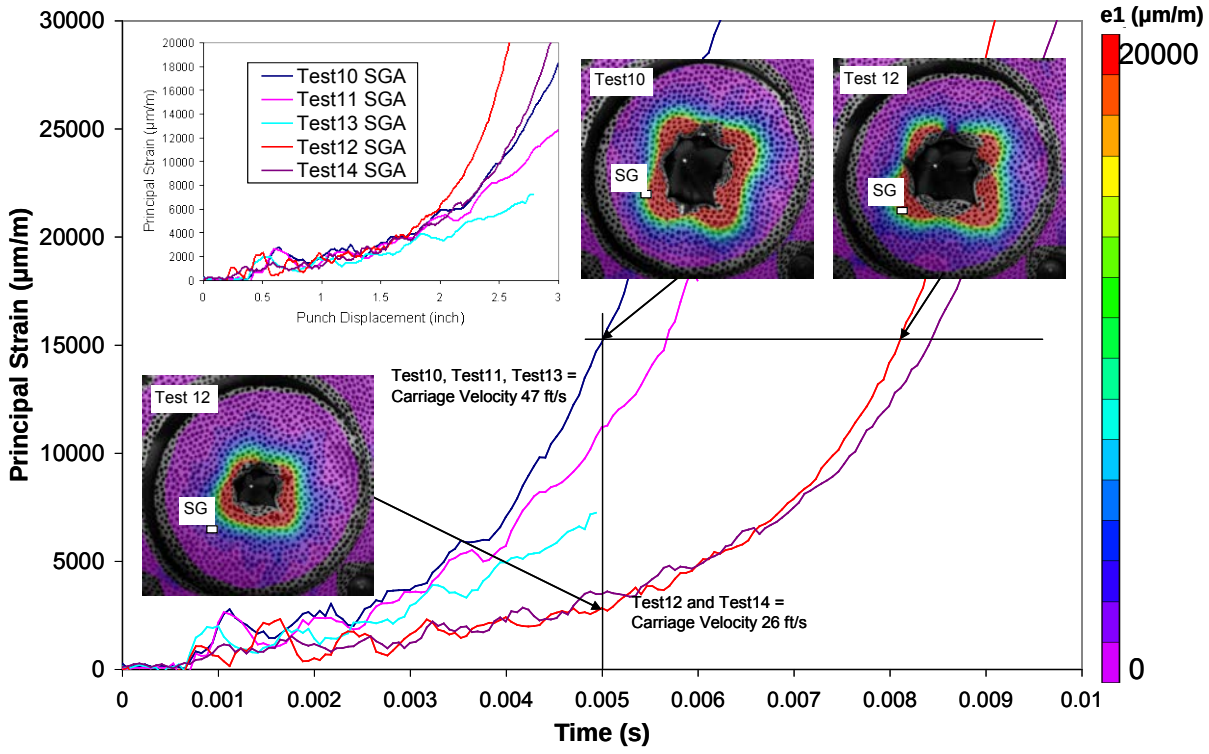

Figure 96. Dynamic loading of the mild-steel plate with the conical punch

Principal strain versus time are plotted in Figure 96. As shown, the punch travels more slowly for the lower punch height although, for similar strains, the punch has penetrated a similar amount. Also shown are two strain plots indicating the gage location and strain at time = 0.005 seconds and another from Test 12 when the strain is ~15,000 µm/m. The inset of Figure 96 shows the data plotted versus punch displacement for Tests 10–14.

3.6.2 Comparison

By plotting the strain results versus the punch displacement, it is possible to get a general comparison between the static and dynamic results. For the static results, the DIC software recorded the punch displacement along with the image information during acquisition. For the dynamic tests, this was not possible, and IRIG was used to time stamp both the images and the punch test displacement. During analysis, it is then possible to determine which frame corresponds to the trigger point, and all of the data can be aligned. This was done for a single test with the results shown in Figure 97.

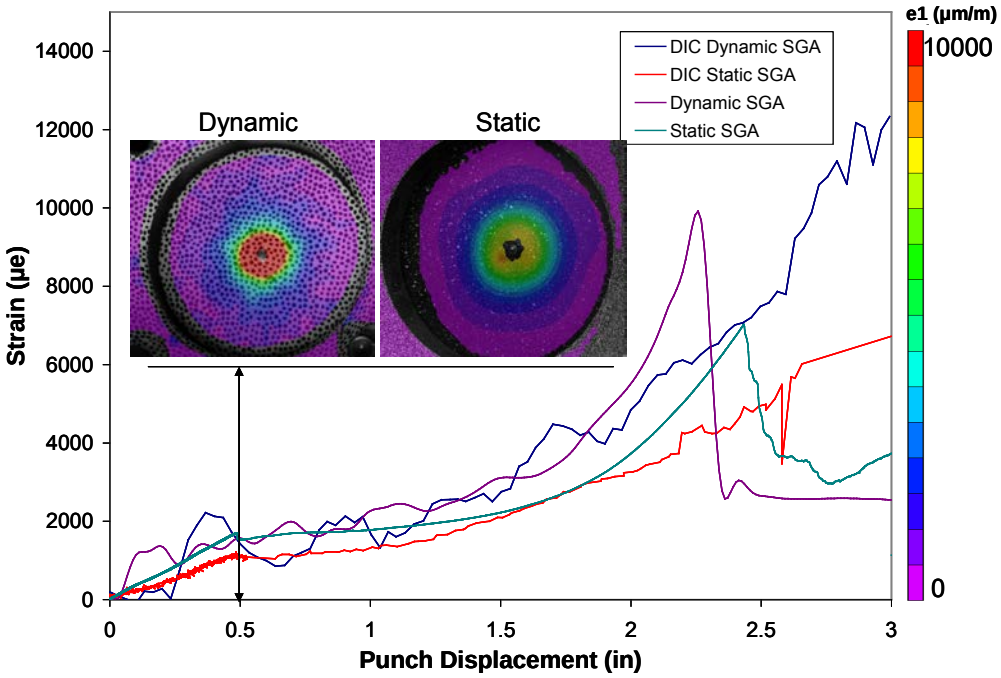

Figure 97. Comparison of dynamic and static results of DIC and strain gage results

4 CONCLUSIONS

A significant amount of data that will be useful for the verification and validation of computational models of ductile failure were collected and were described here. However, much work remains to be performed, including:

- Comparisons of static to dynamic data
- Comparisons to FY07 testing
- Reduction of DIC data and comparisons
- Extraction of crack formation times from high-speed video
- Comparison to finite element simulations
- Revision of the dynamic fixture

Additionally, future testing should include other materials and other punch geometries, and a set of tests should be developed to investigate the nonclassic failure pattern of abrasion-resistant plate, perhaps by attempting to test thinner samples.

APPENDIX A: ACCELERATION, VELOCITY CHANGE, DISPLACEMENT, FORCE, AND MICROSTRAIN VS. TIME DATA PLOTS

This appendix presents the acceleration, velocity change, displacement, force, and microstrain vs. time data plots for the following test scenarios:

- Mild Steel, Flat Punch (§A.1)
- Mild Steel, Conical Punch (§A.2)
- Abrasion-Resistant Plate, Conical Punch (§A.3)

The plots for each of these scenarios are shown in the indicated subsection. Table A-1 summarizes content of each plot presented in this appendix.

Table A-1. Summary of Data (Y Axis) vs. Time (X Axis) Plots

Material	Punch	Test(s)	Y Axis	X Axis	Subsection	Figure
Mild Steel	Flat	3, 6, 7, 8, 9, 15, 16	Acceleration	Time	A.1	A-1
			Velocity Change			A-2
			Displacement			A-3
			Force			A-4
		15	Microstrain[a]			A-5
Mild Steel	Conical	10, 11, 12, 13, 14	Acceleration	Time	A.2	A-6
			Velocity Change			A-7
			Displacement			A-8
			Force			A-9
		13	Microstrain[a]			A-10
Abrasion-Resistant Plate	Conical	17, 18, 19	Acceleration	Time	A.3	A-11
			Velocity Change			A-12
			Displacement			A-13
			Force			A-15
		17	Microstrain[a]			A-15
		18				A-16

Notes

a. Figure shows individual plots for transverse, 45° rosette, and radial strain gage data.

A.1 Mild Steel-Flat Punch Data vs. Time Plots

The following figures show the acceleration, velocity change, displacement, force, and microstrain vs. time data plots for the mild steel-flat punch test scenario:

- Figure A-1: Acceleration vs. Time
- Figure A-2. Velocity Change vs. Time
- Figure A-3. Displacement vs. Time
- Figure A-4. Force vs. Time
- Figure A-5. Microstrain vs. Time

Figure A-5 includes individual plots for transverse, 45° rosette, and radial strain gage data.

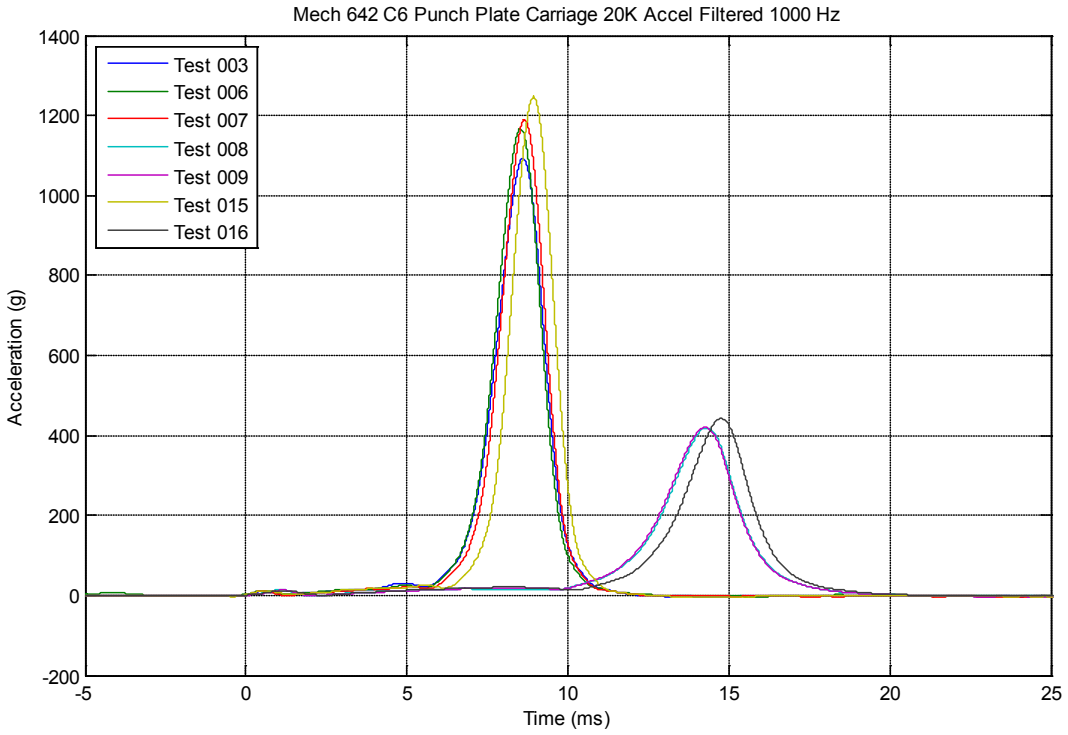

Figure A-1. Mild steel-flat punch acceleration vs. time: Tests 3, 6, 7, 8, 9, 15, 16

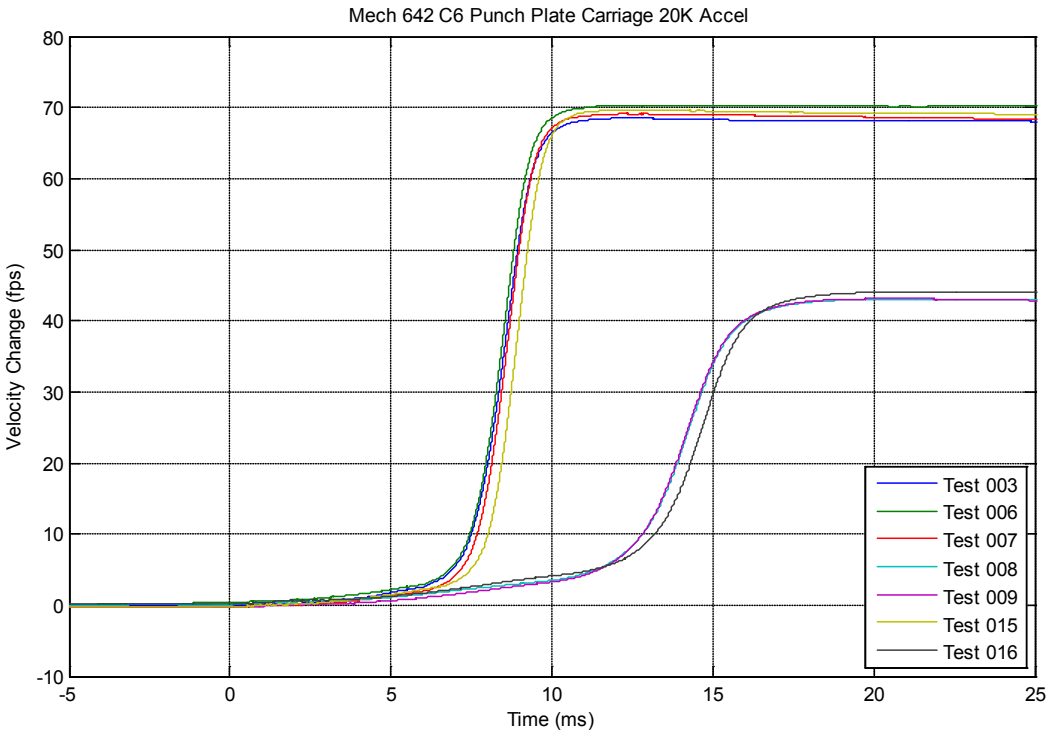

Figure A-2. Mild steel-flat punch velocity change vs. time: Tests 3, 6, 7, 8, 9, 15, 16

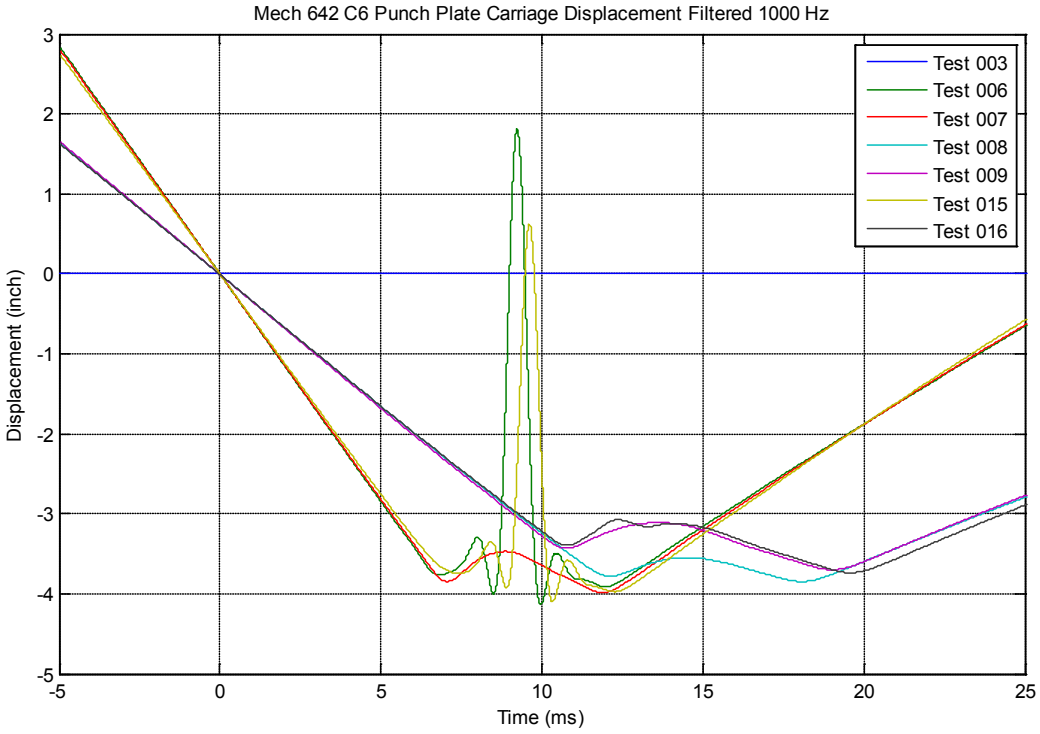

Figure A-3. Mild steel-flat punch displacement vs. time: Tests 3, 6, 7, 8, 9, 15, 16

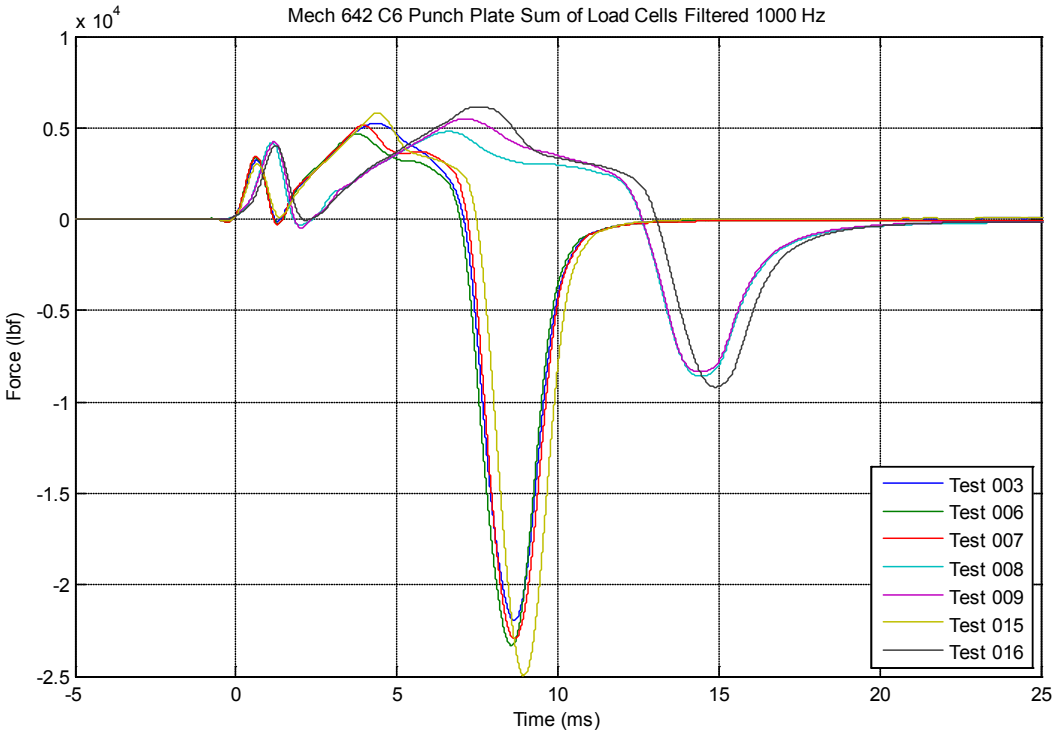

Figure A-4. Mild steel-flat punch force vs. time: Tests 3, 6, 7, 8, 9, 15, 16

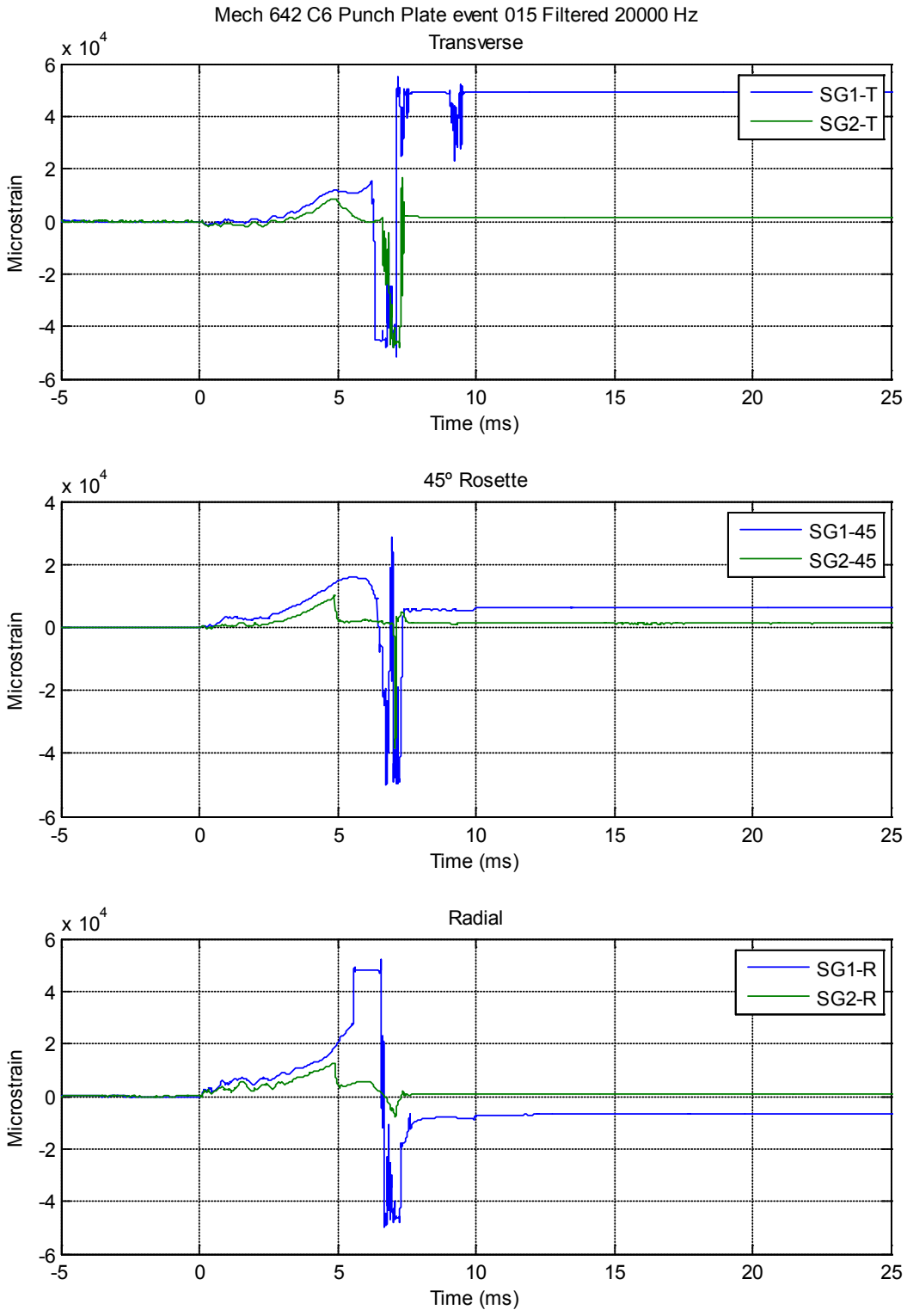

Figure A-5. Mild steel-flat punch microstrain vs. time: Test 15

A.2 Mild Steel-Conical Punch Data vs. Time Plots

The following figures show the acceleration, velocity change, displacement, force, and microstrain vs. time data plots for the mild steel-conical punch test scenario:

- Figure A-6: Acceleration vs. Time
- Figure A-7. Velocity Change vs. Time
- Figure A-8. Displacement vs. Time
- Figure A-9. Force vs. Time
- Figure A-10. Microstrain vs. Time

Figure A-10 includes individual plots for transverse, 45° rosette, and radial strain gage data.

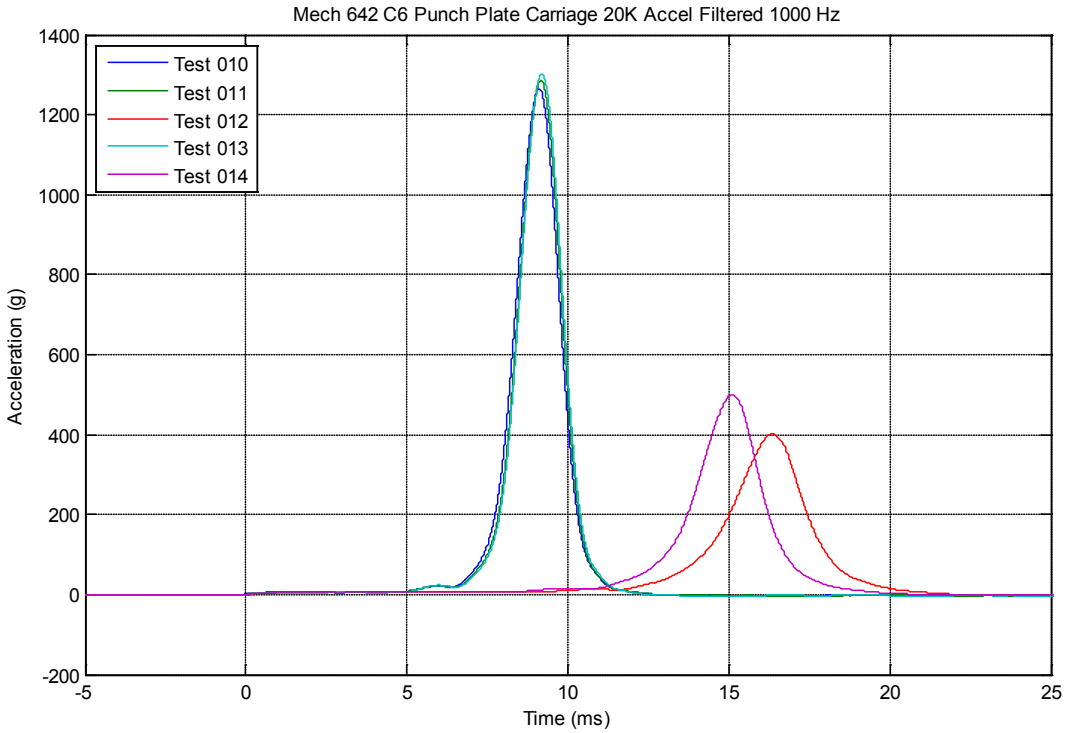

Figure A-6. Mild steel-conical punch acceleration vs. time: Tests 10, 11, 12, 13, 14

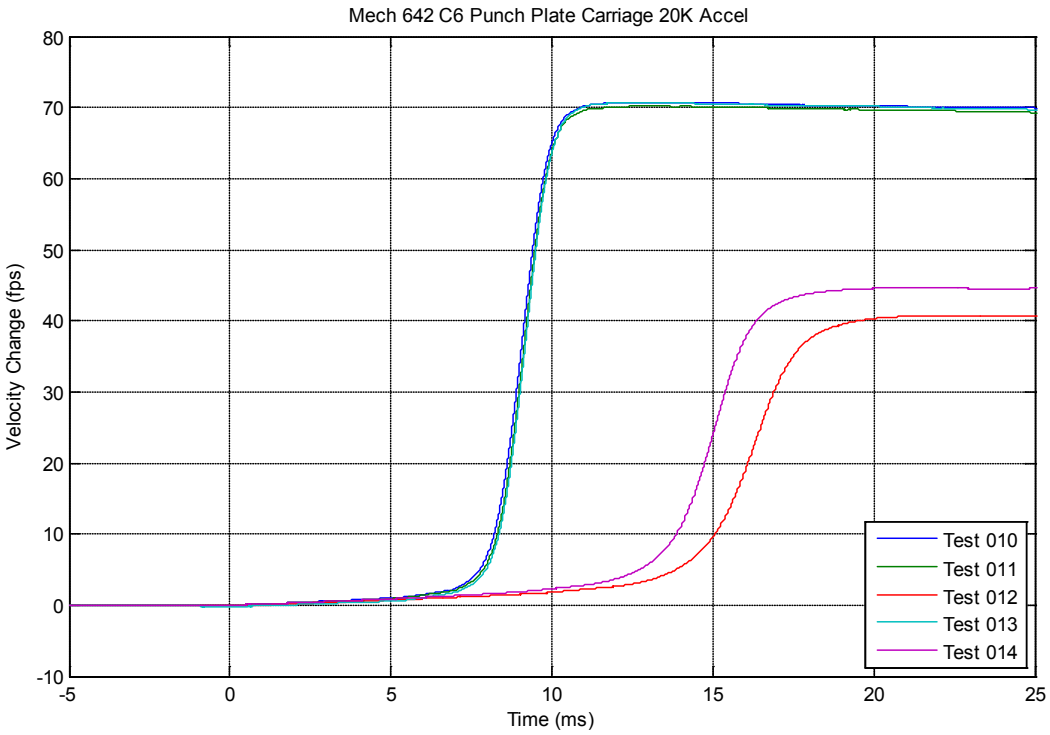

Figure A-7. Mild steel-conical punch velocity change vs. time: Tests 10, 11, 12, 13, 14

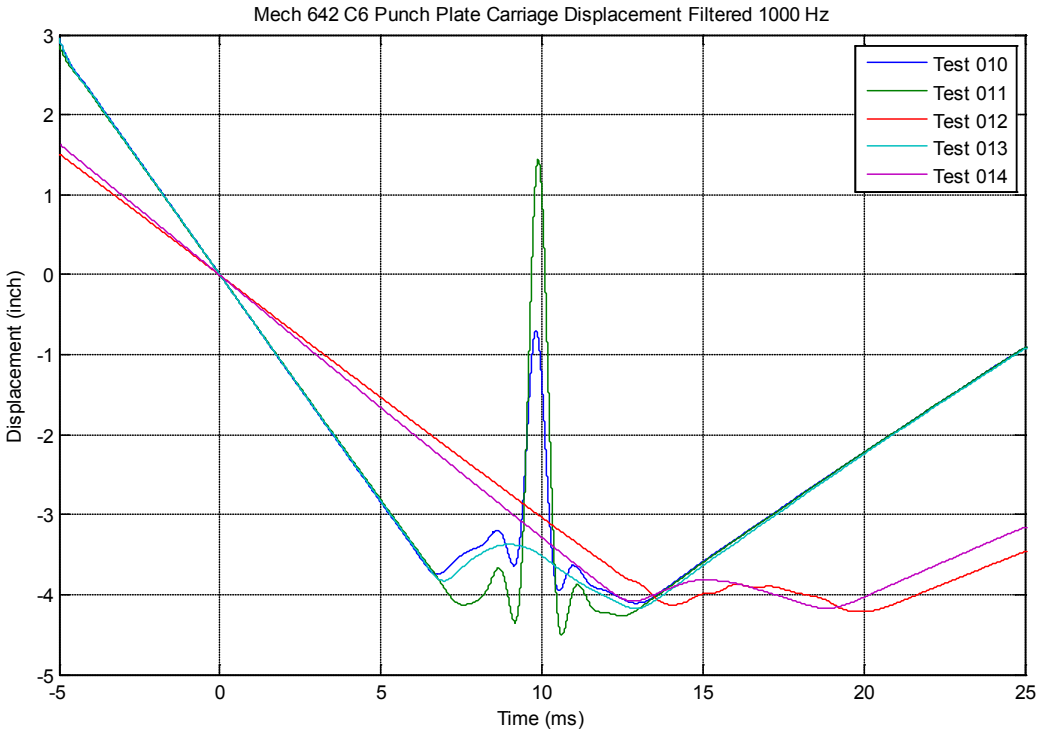

Figure A-8. Mild steel-conical punch displacement vs. time: Tests 10, 11, 12, 13, 14

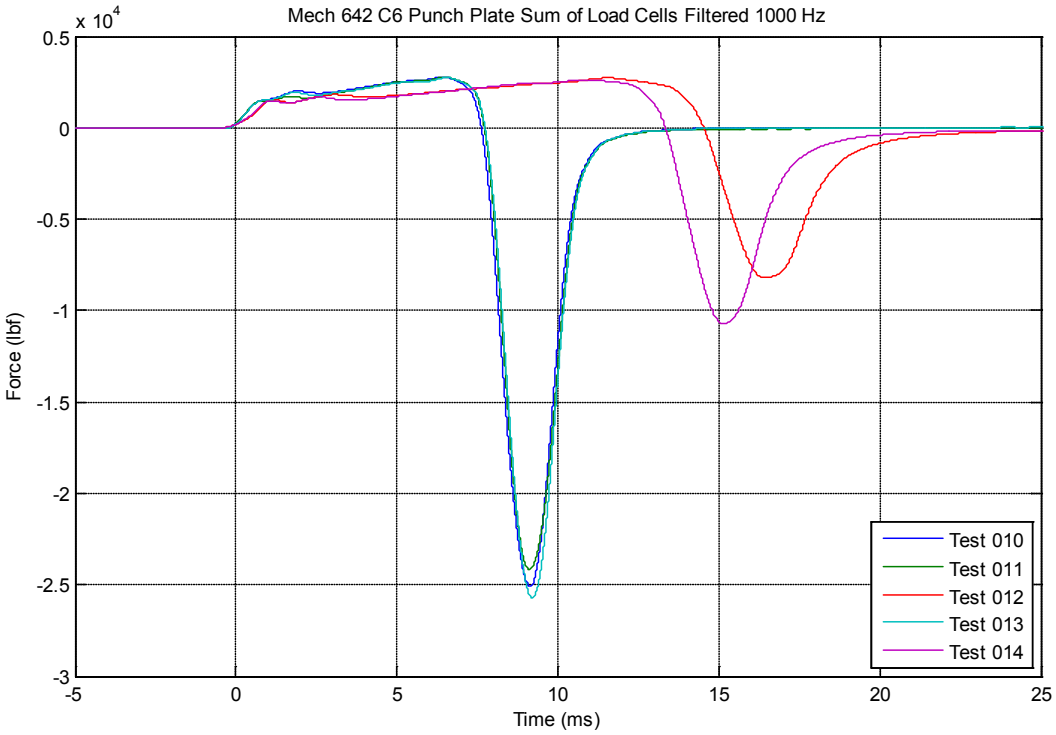

Figure A-9. Mild steel-conical punch force vs. time: Tests 10, 11, 12, 13, 14

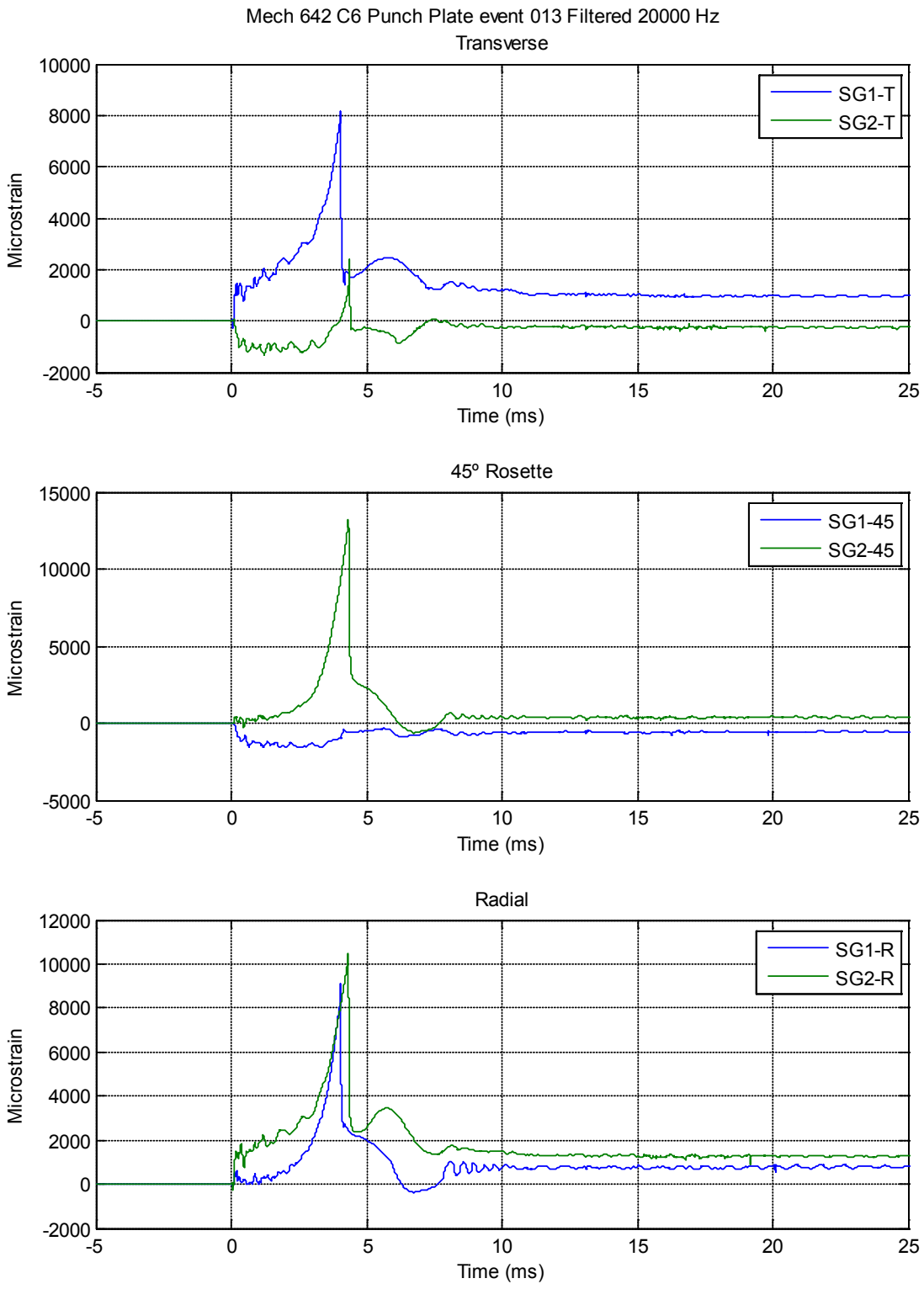

Figure A-10. Mild steel-conical punch microstrain vs. time: Test 13

A.3 Abrasion-Resistant Plate-Conical Punch Data vs. Time Plots

The following figures show the acceleration, velocity change, displacement, force, and microstrain vs. time data plots for the abrasion-resistant plate-conical punch test scenario:

- Figure A-11: Acceleration vs. Time
- Figure A-12. Velocity Change vs. Time
- Figure A-13. Displacement vs. Time
- Figure A-14. Force vs. Time
- Figure A-15. Microstrain vs. Time

Figure A-15 includes individual plots for transverse, 45° rosette, and radial strain gage data.

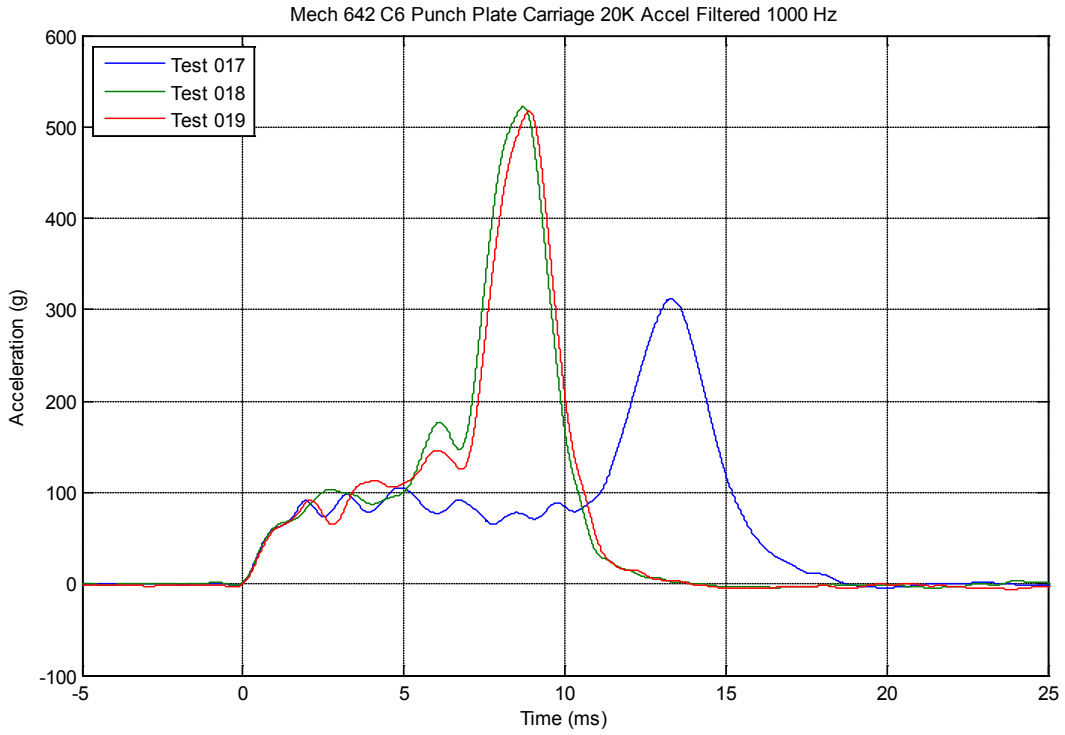

Figure A-11. Abrasion-resistant plate-conical punch acceleration vs. time: Tests 17, 18, 19

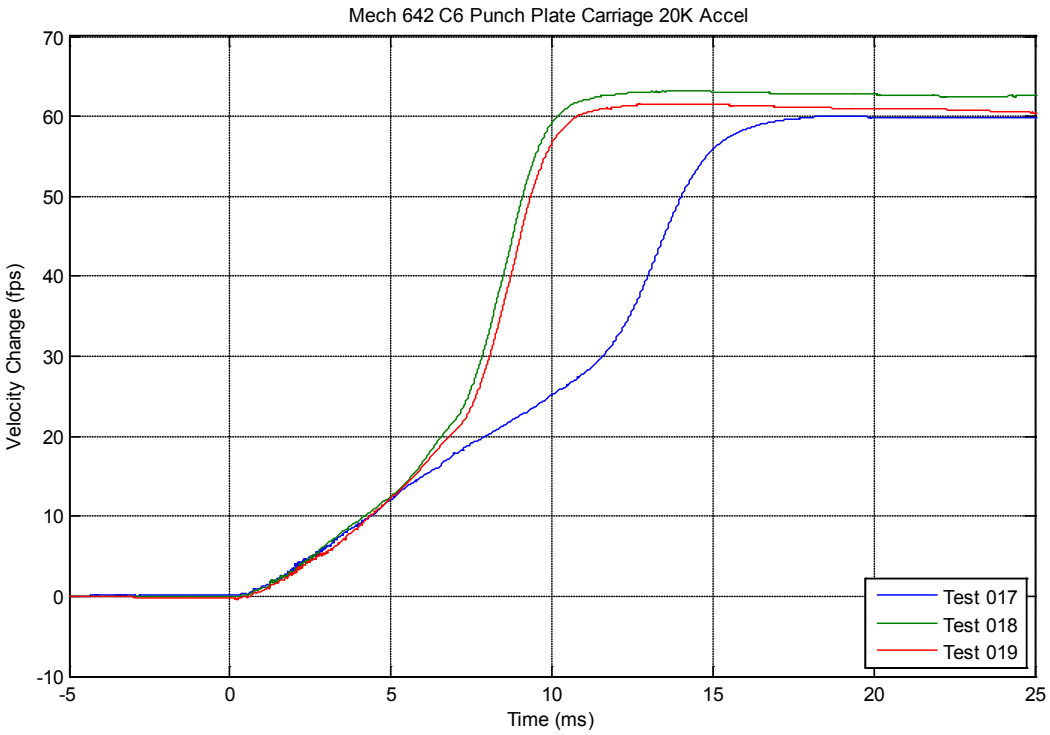

Figure A-12. Abrasion-resistant plate-conical punch velocity vs. time: Tests 17, 18, 19

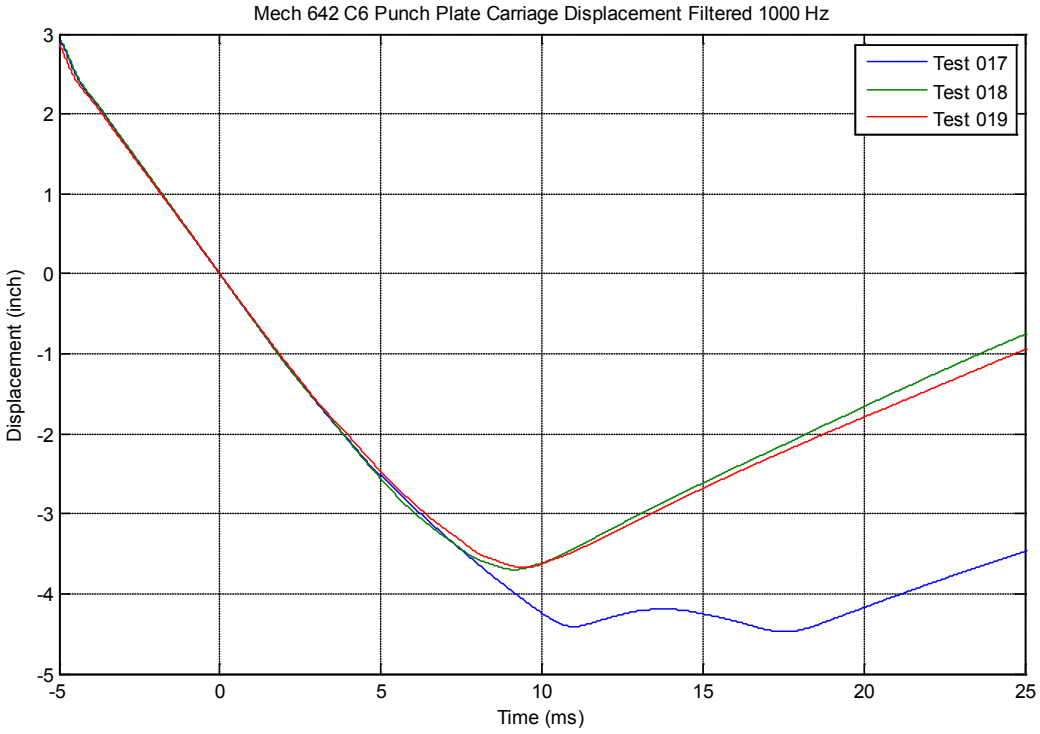

Figure A-13. Abrasion-resistant plate-conical punch displacement vs. time: Tests 17, 18, 19

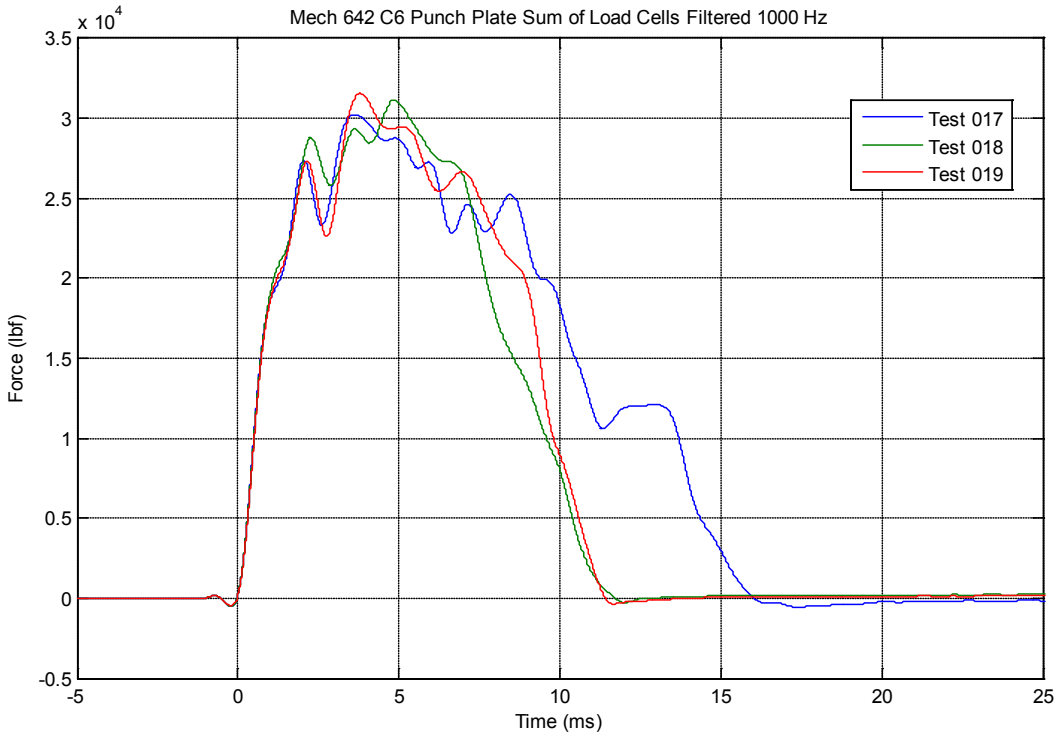

Figure A-14. Abrasion-resistant plate-conical punch force vs. time: Tests 17, 18, 19

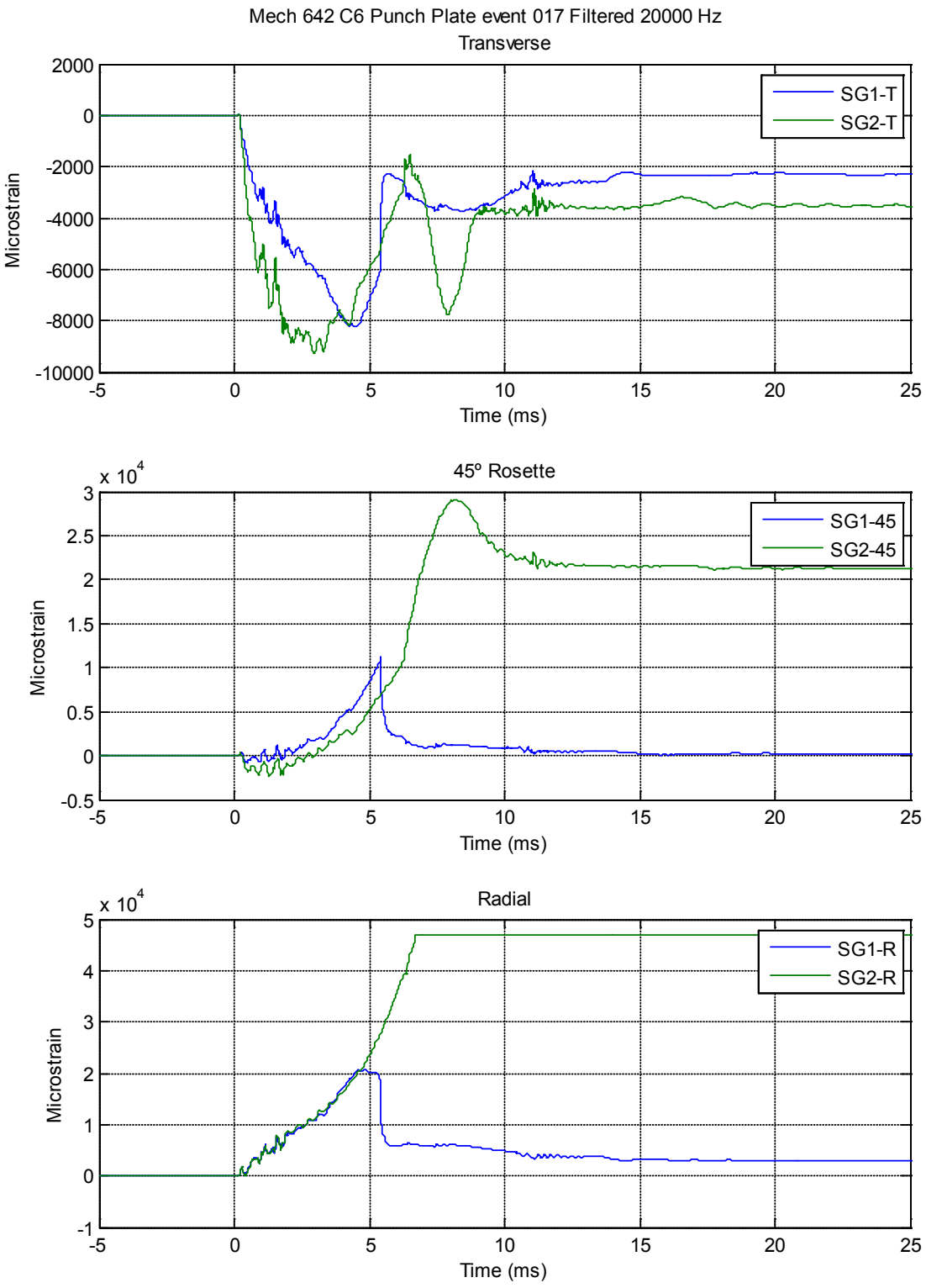

Figure A-15. Abrasion-resistant plate-conical punch microstrain vs. time: Test 17

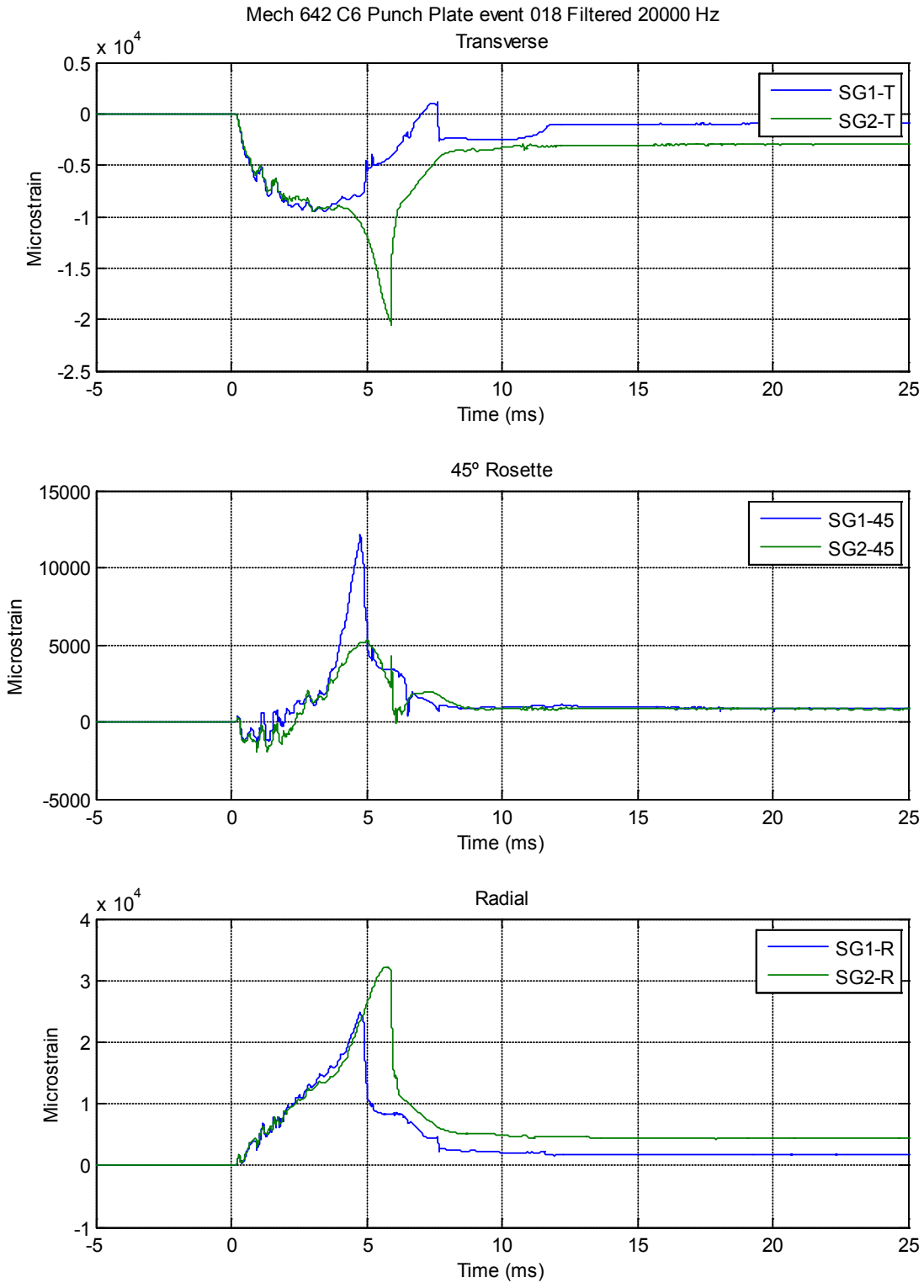

Figure A-16. Abrasion-resistant plate-conical punch microstrain vs. time: Test 18

APPENDIX B: LOAD, MICROSTRAIN, ACCELERATION, VELOCITY, AND VELOCITY CHANGE VS. DISPLACEMENT DATA PLOTS

This appendix presents the load, microstrain, acceleration, velocity, and velocity change vs. displacement data plots for the following test types:

- Mild Steel, Flat Punch (§B.1)
- Mild Steel, Conical Punch (§B.2)
- Abrasion-Resistant Plate, Conical Punch (§B.3)

The plots for each of these test types are shown in the indicated subsection. Table B-1 summarizes content of each plot presented in this appendix.

Table B-1. Summary of Data (Y Axis) vs. Displacement (X Axis) Plots

Material	Punch	Test(s)	Y Axis	X Axis	Subsection	Figure
Mild Steel	Flat	3, 6, 7, 8, 9, 15, 16	Load	Displacement	B.1	B-1
		15	Microstrain[a]			B-2
Mild Steel	Conical	10, 11, 12, 13, 14	Load	Displacement	B.2	B-3
		13	Microstrain[a]			B-4
Abrasion-Resistant Plate	Conical	17, 18, 19	Load	Displacement	B.3	B-5
			Acceleration			B-6
			Velocity Change			B-7
			Velocity			B-8
		17	Microstrain[a]			B-9
		18				B-10

Notes

a. Figure shows individual plots for transverse, 45° rosette, and radial strain gage data.

B.1 Mild Steel-Flat Punch Data vs. Displacement Plots

The following figures show the load, microstrain, acceleration, velocity, and velocity change vs. displacement data plots for the mild steel-flat punch test scenario:

- Figure B-1: Load vs. Displacement
- Figure B-2. Microstrain vs. Displacement

Figure B-2 includes individual plots for transverse, 45° rosette, and radial strain gage data.

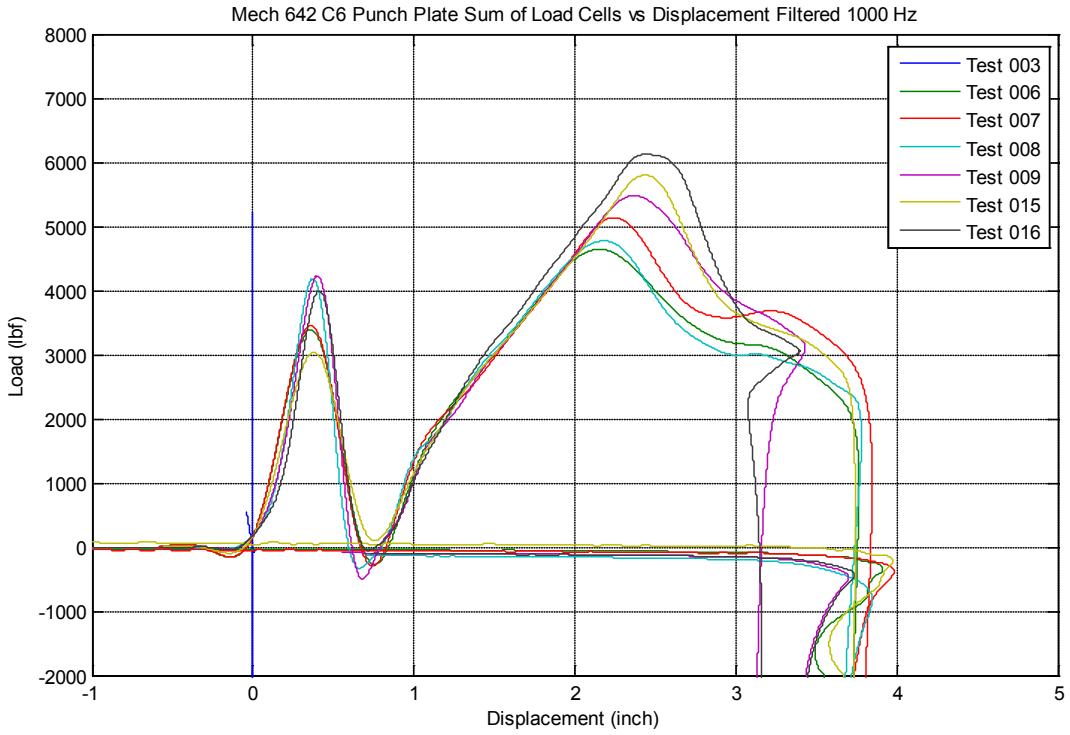

Figure B-1. Mild steel-flat punch load vs. displacement: Tests 3, 6, 7, 8, 9, 15, 16

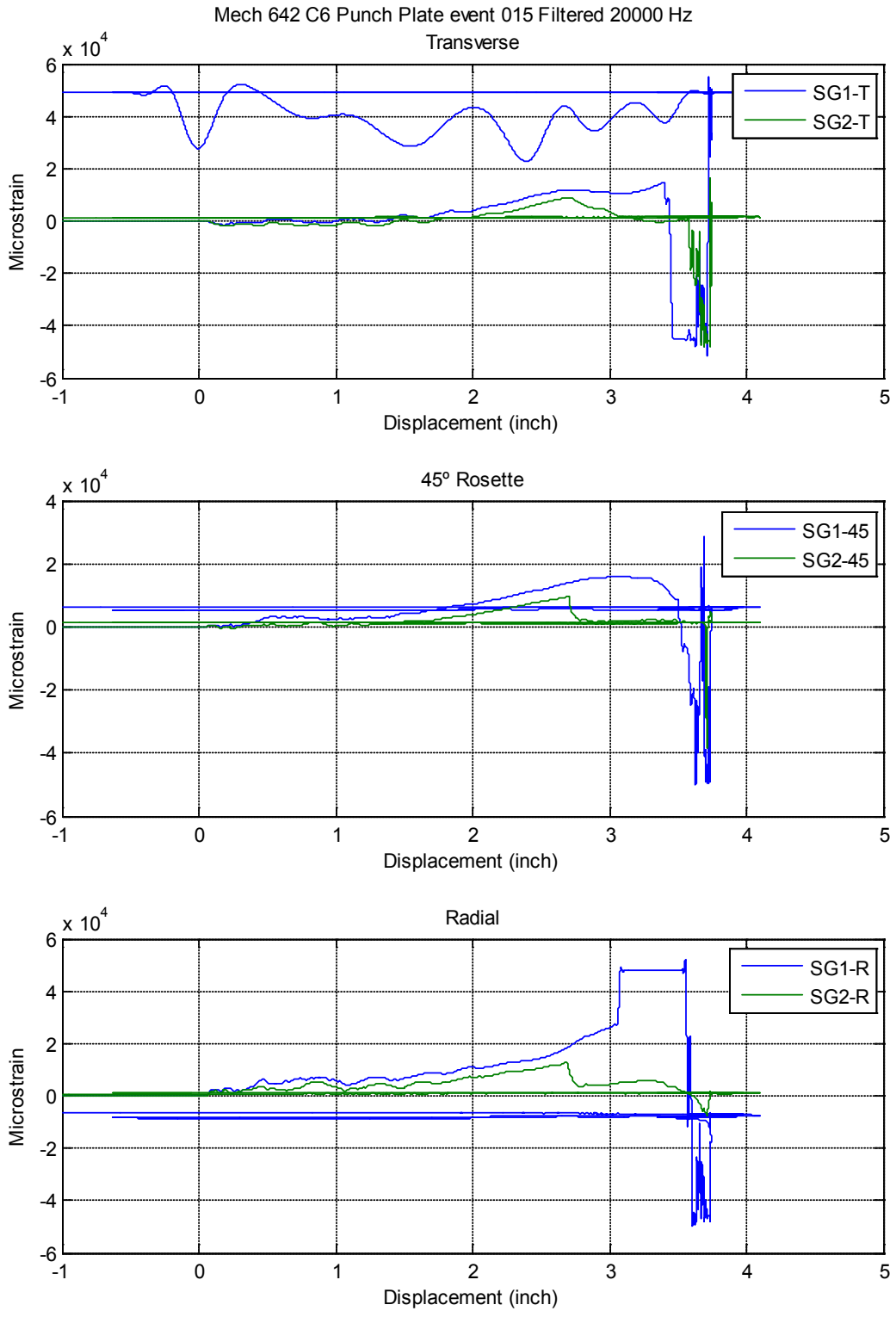

Figure B-2. Mild steel-flat punch microstrain vs. displacement: Test 15

B.2 Mild Steel-Conical Punch Data vs. Displacement Plots

The following figures show the load, microstrain, acceleration, velocity, and velocity change vs. displacement data plots for the mild steel-conical punch test scenario:

- Figure B-3: Load vs. Displacement
- Figure B-4. Microstrain vs. Displacement

Figure B-4 includes individual plots for transverse, 45° rosette, and radial strain gage data.

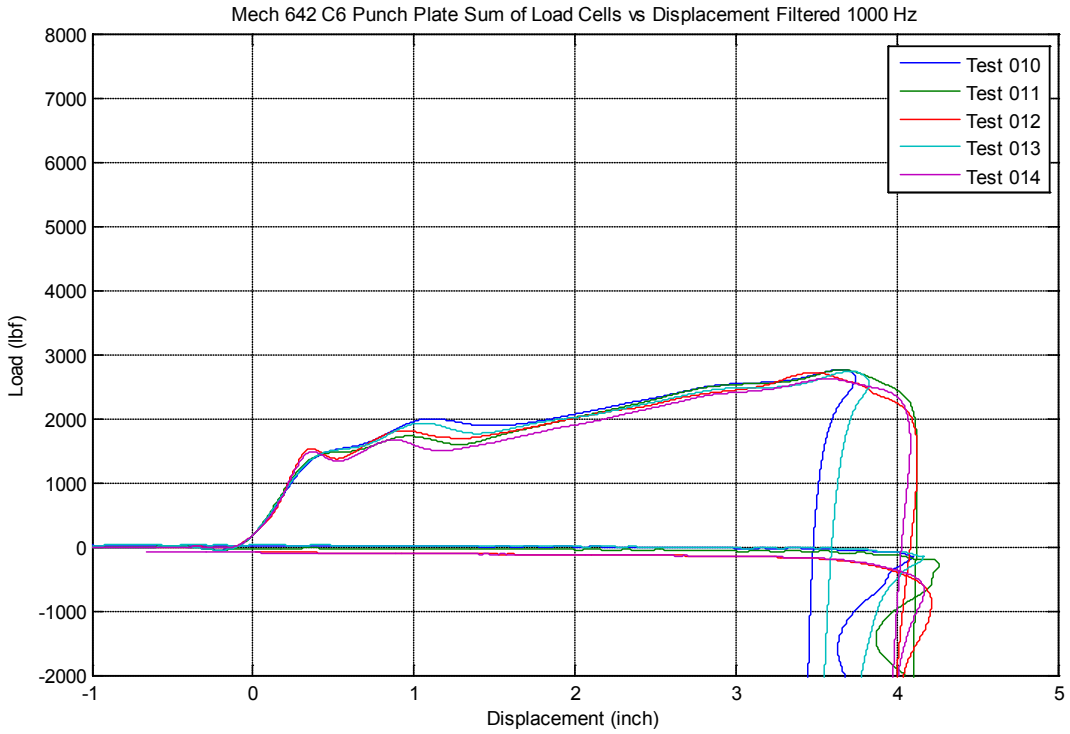

Figure B-3. Mild steel-conical punch load vs. displacement: Tests 10, 11, 12, 13, 14

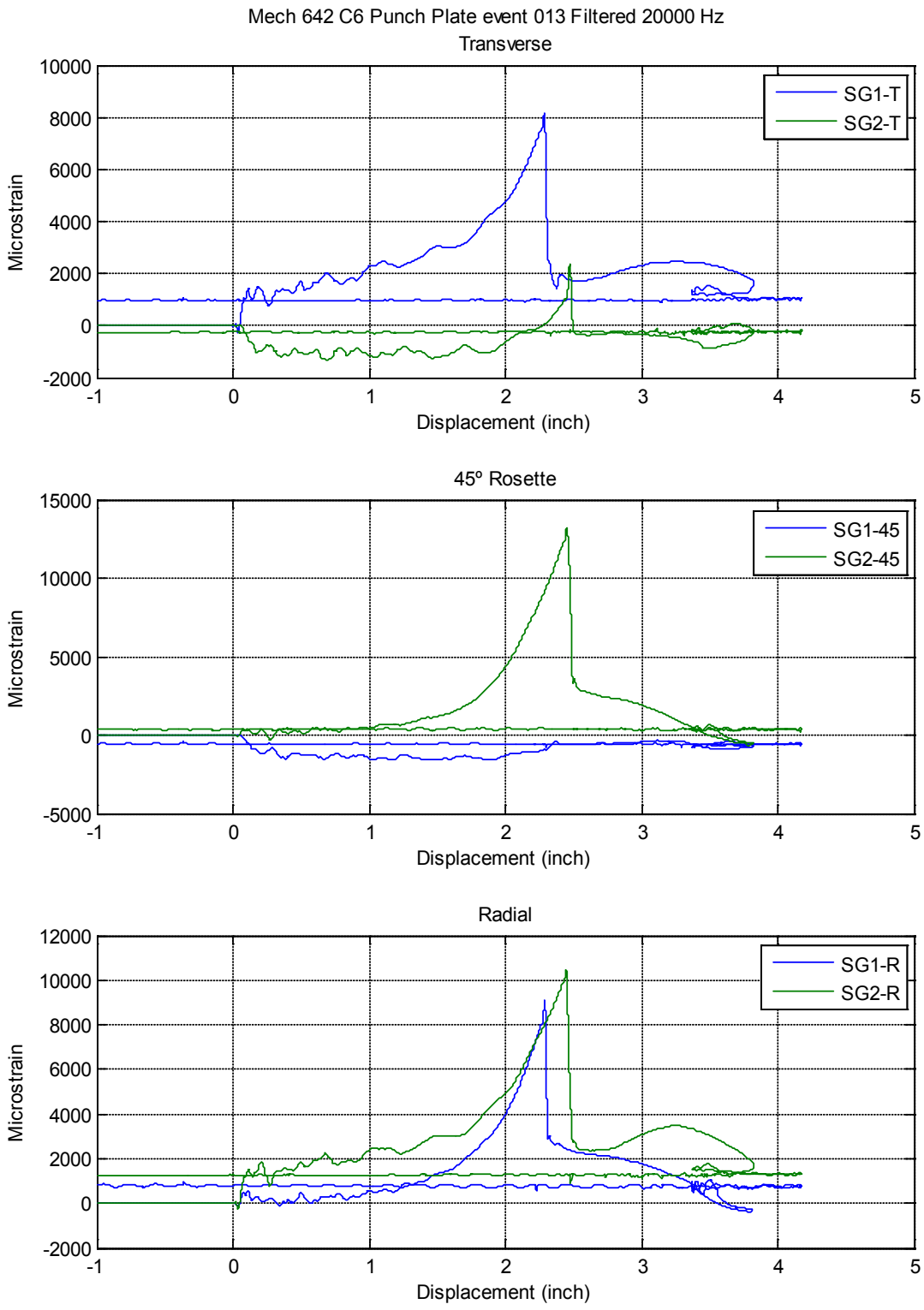

Figure B-4. Mild steel-conical punch microstrain vs. displacement: Test 13

B.3 Abrasion-Resistant Plate-Conical Punch Data vs. Displacement Plots

The following figures show the load, microstrain, acceleration, velocity, and velocity change vs. displacement data plots for the abrasion-resistant plate-conical punch test scenario:

- Figure B-5: Load vs. Displacement
- Figure B-6: Acceleration vs. Displacement
- Figure B-7: Velocity Change vs. Displacement
- Figure B-8: Velocity vs. Displacement
- Figure B-9: Microstrain vs. Displacement (Test 17)
- Figure B-10: Microstrain vs. Displacement (Test 18)

Figures B-9 and B-10 include individual plots for transverse, 45° rosette, and radial strain gage data.

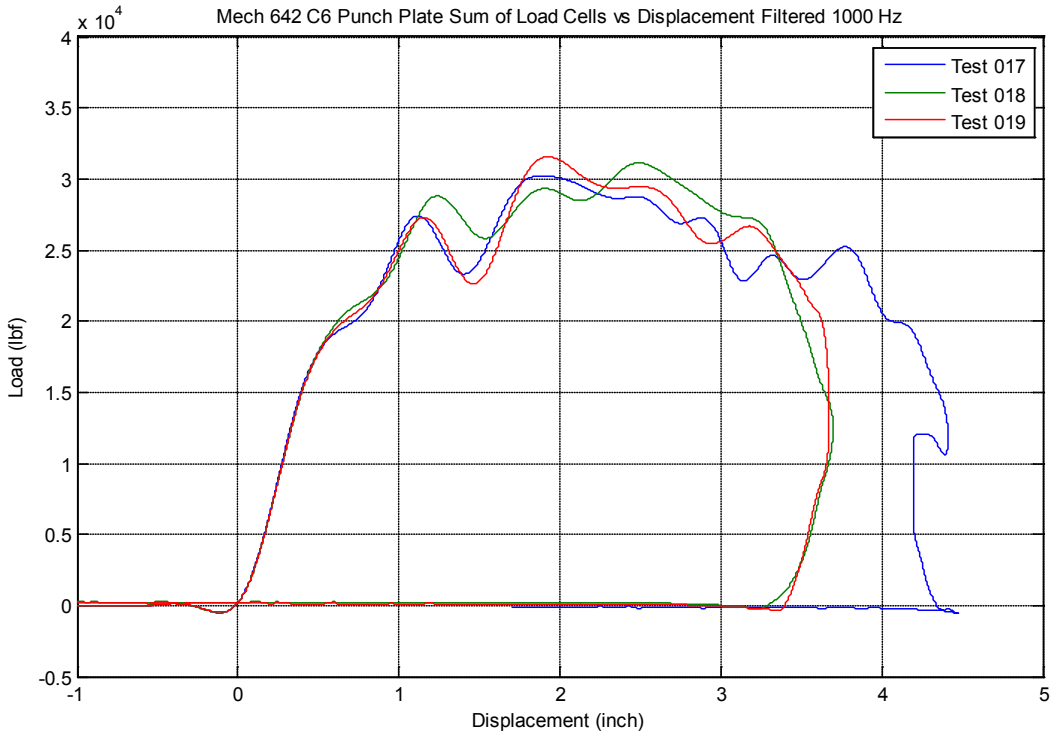

Figure B-5. Abrasion-resistant plate-conical punch load vs. displacement: Tests 17, 18, 19

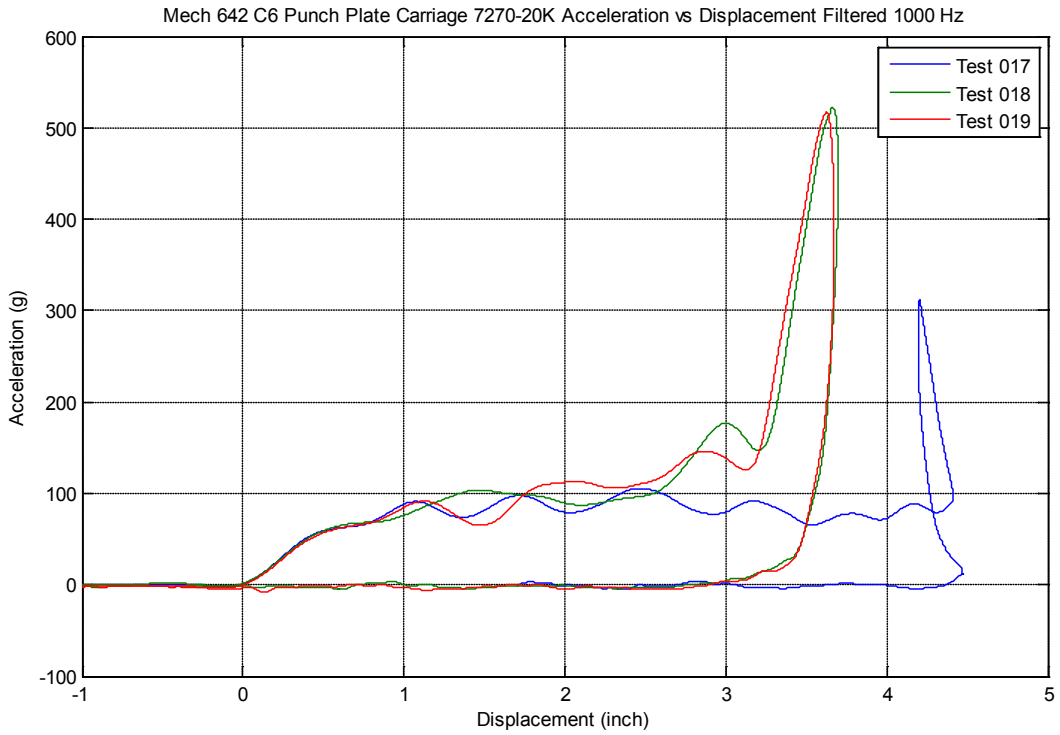

Figure B-6. Abrasion-resistant plate-conical punch acceleration vs. displacement: Tests 17, 18, 19

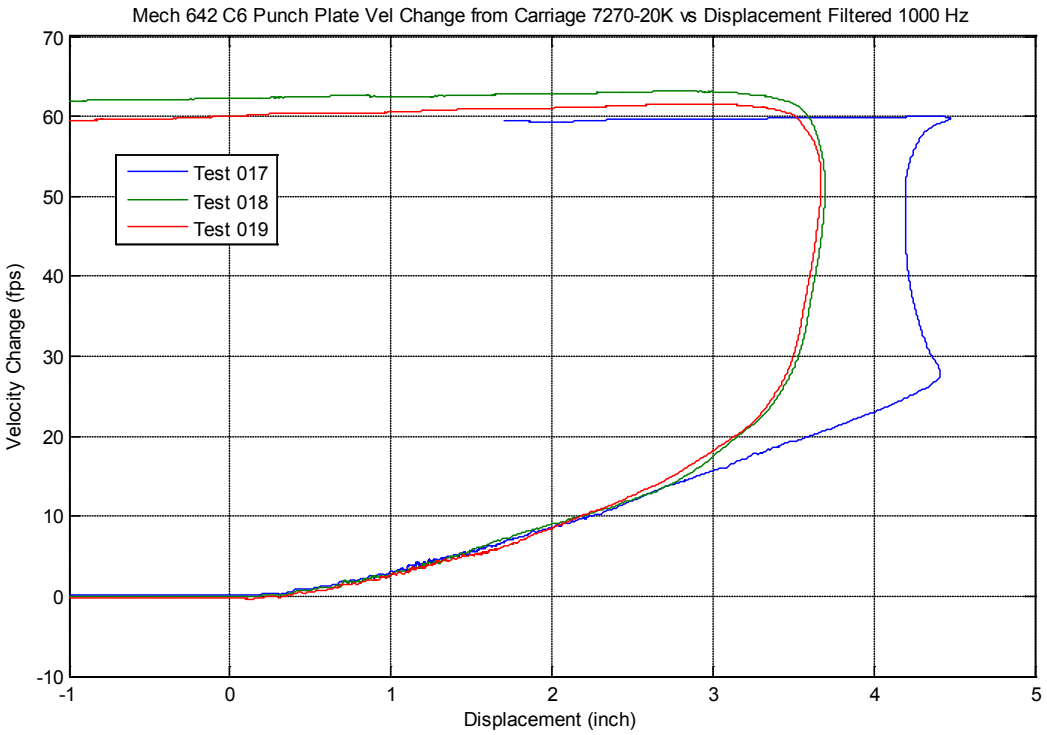

Figure B-7. Abrasion-resistant plate-conical punch velocity change vs. displacement: Tests 17, 18, 19

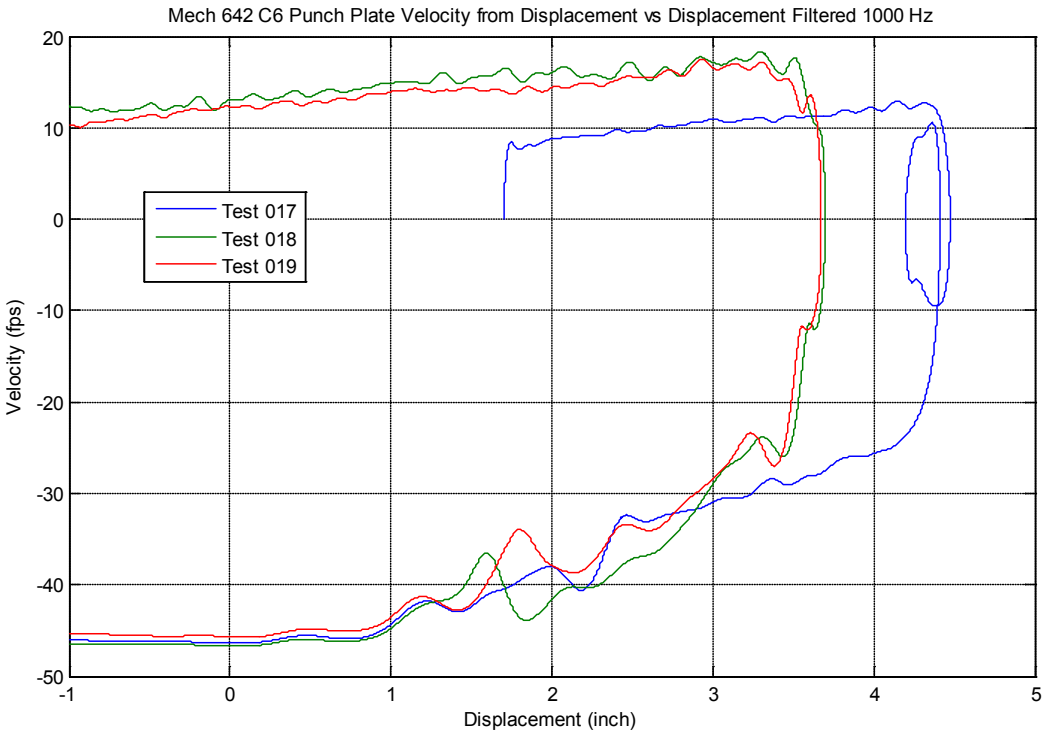

Figure B-8. Abrasion-resistant plate-conical punch velocity vs. displacement: Tests 17, 18, 19

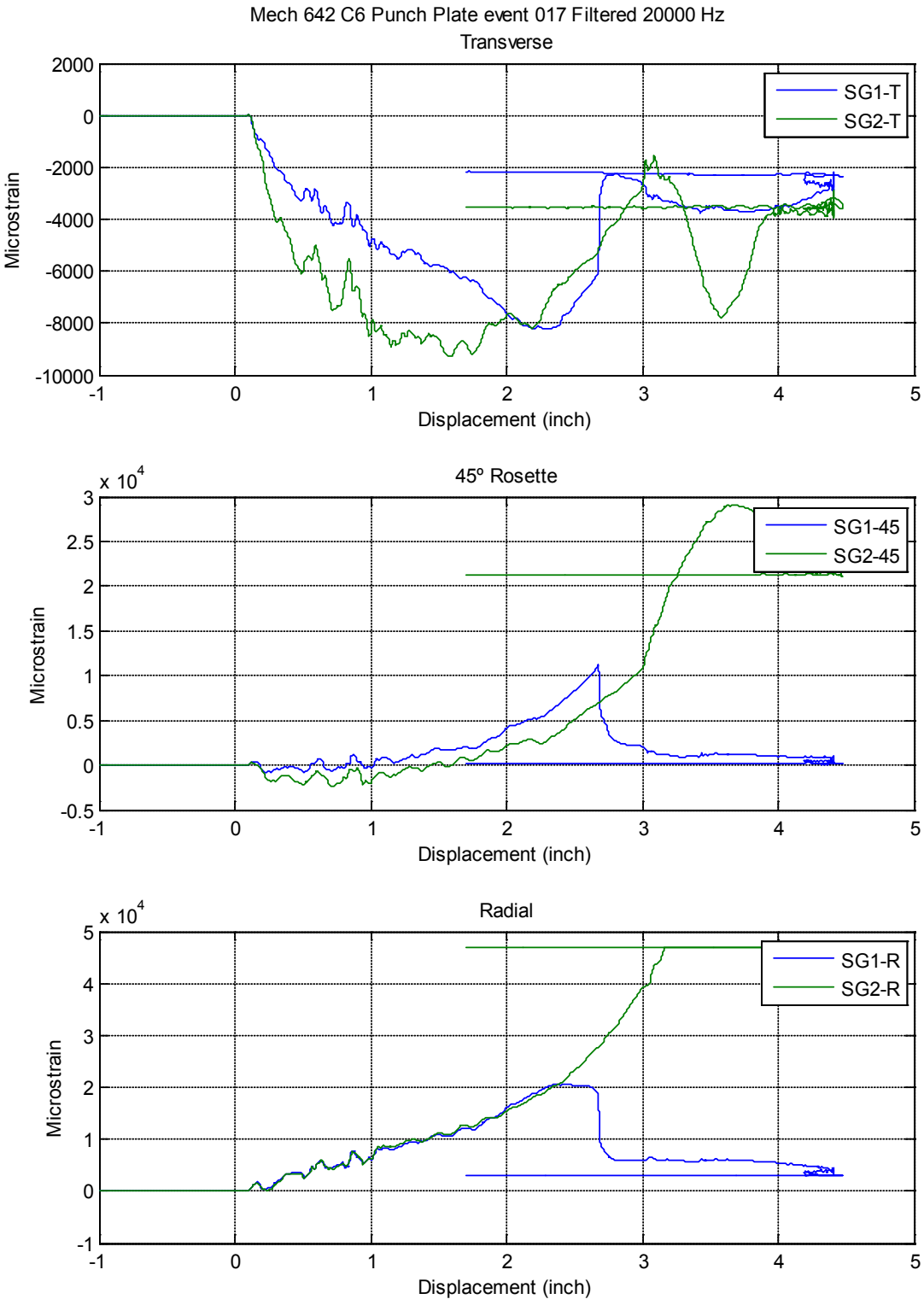

Figure B-9. Abrasion-resistant plate-conical punch microstrain vs. displacement: Test 17

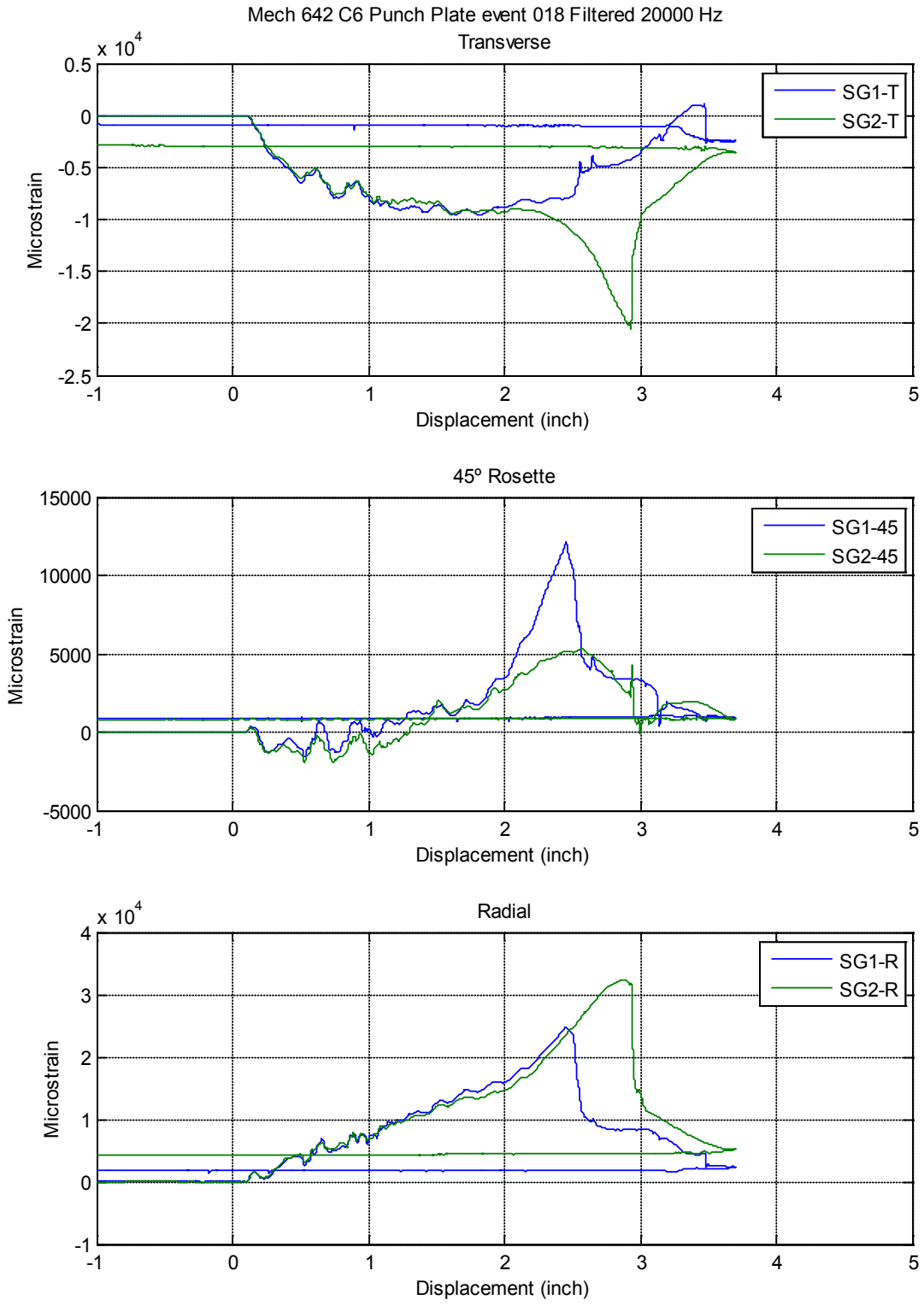

Figure B-10. Abrasion-resistant plate-conical punch microstrain vs. displacement: Test 18

DISTRIBUTION

Internal Distribution:

1	MS 0372	Doug VanGoethem, 01526
1	MS 0372	Nicole Breivik, 01524
1	MS 0372	Kurt Metzinger, 01524
1	MS 0557	Matt Spletzer, 01521
1	MS 0557	David Epp, 01522
1	MS 0840	Justine Johannes, 01520
1	MS 1139	Phil Reu, 01535
1	MS 1139	Jody Smith, 01535
1	MS0899	Technical Library, 9536 (electronic copy)


Sandia National Laboratories